

UNIVERSIDADE DE SANTIAGO DE  
COMPOSTELA

FACULDADE DE FÍSICA

Departamento de Física de Partículas



Neutron-induced fission fragment angular  
distribution at CERN n\_TOF:  
The Th-232 case

Memoria presentada para  
optar al Grado de  
Doctor en Física por:  
**Diego Tarrío Vilas**  
Abril 2012





## UNIVERSIDADE DE SANTIAGO DE COMPOSTELA

**Ignacio Durán Escribano**, Catedrático de Física Atómica, Molecular y Nuclear de la Universidad de Santiago de Compostela, y **Carlos Paradela Dobarro**, investigador contratado de la Universidad de Santiago de Compostela,

### CERTIFICAN:

que la memoria titulada **Neutron-induced fission fragment angular distribution at CERN n\_TOF: The Th-232 case** ha sido realizada por **Diego Tarrío Vilas** en el **Departamento de Física de Partículas** de esta Universidad bajo su dirección y constituye el trabajo de **tesis** que presenta para optar al grado de **Doctor en Física**.

Santiago de Compostela, 30 de abril de 2012.

Fdo: Ignacio Durán Escribano

Fdo: Carlos Paradela Dobarro

Fdo: Diego Tarrío Vilas



*A mis padres  
y a Alma*



# Acknowledgments

As usually happens, a thesis work in experimental nuclear physics is the result of a great effort where many people are involved. I am therefore indebted to all the n\_TOF collaboration and to the Experimental Group of Nuclei and Particles (GENP) at the Universidade de Santiago.

I would like to start by thanking my supervisor Prof. Ignacio Durán for the trust he has put in me when invited me to join the GENP group, and for the interest demonstrated in the development of this work. I am also indebted to my co-supervisor Carlos Paradela who was not only my first guide at the n\_TOF facility at CERN, but an invaluable help in my daily work.

I want to express my best sincere gratitude to Laurent Tassan-Got because without his valuable work, this experiment would have never been possible. I also have to thank him, Laurent Audouin, and Lou-Sai Leong the excellent treatment that I received during my numerous stays at the IPN-Orsay (France), where I was always warmly welcomed.

A special mention is deserved to Eric Berthoumieux, Carlos Guerrero, Andrea Tsinganis, and all the n\_TOF staff at CERN, because they did their best to ensure that the experiment and the data acquisition system worked properly, solving any technical problem that appeared.

I would also like to thank Nicola Colonna for his welcome during my stay at the INFN in Bari (Italy) and for his estimable remarks to my work. Worthy advices and comments arose also from Daniel Cano, Roberto Capote, Franz Käppeler, Rui Ferreira, José Luis Taín, Rosa Vlastou, and many other people that I will not list here because, for sure, I would forget someone.

I am also very grateful to all the people of the GENP group at Santiago. Among them, I really appreciated the valuable help of David Pérez, Pablo Cabanelas, and Prof. Héctor Álvarez, for whom the software has no secrets

and from whose expertise I took advantage many times in my analysis and simulation works.

I especially thank Prof. José Benlliure, Prof. Dolores Cortina, Manuel Caamaño, and Beatriz Fernández for their fruitful comments during our group meetings. And I do not want to forget my colleagues, because they also helped me with a lot of nice moments that we have shared along these last years: Yassid Ayyad, Saúl Beceiro, Paloma Díaz, Martín Gascón, David González, Esther Leal, Juan Llerena, Magdalena Mostazo, Juan Ramón Pereira, Benjamin Pietras, Diego Ramos, Marisol Robles, José Luis Rodríguez, Carme Rodríguez, Raquel Sorribas, and Jossitt Vargas.

Finalmente, me gustaría agradecer a mis padres el apoyo incondicional que me han demostrado desde hace mucho tiempo, cuando todavía yo no sabía lo que era la física pero sí que tenía claro que eso era lo que me gustaba.

Y a Alma, por haberme animado siempre a seguir adelante.

This work was partially supported by the Spanish *Ministerio of Educación*, under Grant No. FPU-AP2007-04542.

Este trabajo ha contado con la financiación de una beca FPU del Ministerio de Educación, con referencia FPU-AP2007-04542.

# Contents

<b>Introduction</b>	<b>1</b>
<b>1. The nuclear fission</b>	<b>11</b>
1.1. The Single Particle Model . . . . .	12
1.1.1. Angular equations . . . . .	13
1.1.2. The radial equation . . . . .	15
1.2. Self-consistent mean field model . . . . .	16
1.3. The Liquid Drop Model . . . . .	18
1.4. Macroscopic-Microscopic Models . . . . .	22
1.4.1. The fission barrier . . . . .	23
1.4.2. Multimodal fission . . . . .	25
1.4.3. Shape dynamics of the fissioning nucleus . . . . .	26
1.5. Neutron-induced fission . . . . .	27
1.5.1. Mass distribution of the fission fragments . . . . .	30
1.5.2. Released energy in fission . . . . .	32
1.6. Fission fragment angular distribution . . . . .	33
1.6.1. Angular distribution in neutron-induced fission . . . . .	35
<b>2. Experimental setup</b>	<b>39</b>
2.1. Description of the n_TOF facility . . . . .	39
2.1.1. The Proton Synchrotron beam . . . . .	39
2.1.2. The spallation target . . . . .	41
2.1.3. The TOF tube . . . . .	42
2.1.4. Neutron beam characteristics . . . . .	44
2.1.5. The n_TOF Data Acquisition System . . . . .	47
2.2. The experimental fission detection setup . . . . .	49
2.2.1. Parallel Plate Avalanche Counters . . . . .	50
2.2.2. The n_TOF detection setup . . . . .	52
2.2.3. Description of the targets . . . . .	54

<b>3. Experimental analysis</b>	<b>57</b>
3.1. Raw data treatment . . . . .	57
3.2. Fission event building . . . . .	58
3.2.1. Anode signal coincidences . . . . .	59
3.2.2. Looking for cathode signals . . . . .	62
3.2.3. The spatial position of hits . . . . .	64
3.2.4. Selection of cathode signals . . . . .	66
3.3. Reconstruction of the fission fragment trajectory . . . . .	68
3.3.1. Linear momentum transfer . . . . .	69
3.4. Neutron energy calculation . . . . .	70
3.4.1. Properties of the $\gamma$ -flash . . . . .	72
3.5. Selection of fission events . . . . .	74
<b>4. Simulation work</b>	<b>77</b>
4.1. Description of the simulation setup . . . . .	78
4.2. Fission event generator . . . . .	79
4.2.1. Mass and charge distribution . . . . .	79
4.2.2. Energy distribution . . . . .	80
4.2.3. Angular distribution . . . . .	81
4.3. Simulation of fission events . . . . .	83
4.3.1. Detected events . . . . .	84
4.4. Simulation results . . . . .	85
4.4.1. Detection efficiency . . . . .	85
4.4.2. The effect of the backing thickness . . . . .	88
4.4.3. The effect of the linear momentum transfer . . . . .	88
4.4.4. Relation between the time difference and the emission angle . . . . .	90
<b>5. Results on <math>^{232}\text{Th}(\text{n},\text{f})</math></b>	<b>93</b>
5.1. Fission fragment angular distribution . . . . .	93
5.1.1. Experimental FFAD in $^{232}\text{Th}(\text{n},\text{f})$ . . . . .	94
5.1.2. The anisotropy parameter . . . . .	98
5.1.3. Discussion on the FFAD results . . . . .	99
5.1.4. Comparison with a perpendicular PPAC setup . . . . .	102
5.2. Fission cross section measurement . . . . .	105
5.2.1. Detection efficiency . . . . .	106
5.2.2. Anisotropy correction in $^{232}\text{Th}(\text{n},\text{f})$ cross section . . . . .	108
5.2.3. Fission cross section ratio $^{232}\text{Th}/^{235}\text{U}$ . . . . .	108
5.2.4. Results on the $^{232}\text{Th}(\text{n},\text{f})$ cross section . . . . .	109
5.3. Identification of fission modes . . . . .	114

<b>Summary and conclusions</b>	<b>121</b>
<b>Resumen en castellano</b>	<b>125</b>
<b>A. Legendre polynomials</b>	<b>141</b>
A.1. Introduction to the Legendre polynomials . . . . .	141
A.2. Properties of the Legendre polynomials . . . . .	142
<b>B. Linear momentum transfer</b>	<b>145</b>
<b>C. Numerical results</b>	<b>147</b>



# Introduction

This thesis examines the neutron-induced fission of  $^{232}\text{Th}$  using a Parallel Plate Avalanche Counter (PPAC) setup with targets in between. The experimental work has been carried out at CERN in the frame of the international collaboration n\_TOF. The experimental objective was to obtain the fission fragment angular distribution and the fission cross section as a function of the neutron energy [1, 2].

The two-fold purpose of this thesis work is: 1) to demonstrate the suitability of the geometrical configuration used to measure the angular distribution of the fragments emitted during fission, with the aim of being able to correct the efficiency in fission cross section measurements with the best accuracy because they are related to the  $(n,\gamma)$  and  $(n,f)$  cross sections; and 2) to measure the angular distribution and the fission cross section of the neutron-induced fission of  $^{232}\text{Th}$  in the energy range from the fission threshold up to 1 GeV. Successful and accurate results have been demonstrated in previous measurements of the fission cross sections of actinides  $^{234}\text{U}$  and  $^{237}\text{Np}$  [3], and subactinides  $^{nat}\text{Pb}$  and  $^{209}\text{Bi}$  [4], going up to a high neutron energy that has not been reached in any other experimental facility.

Research on neutron-induced reactions is of great relevance in basic and applied nuclear physics. Knowledge of resonances in radiative capture,  $(n,\gamma)$ , and in neutron-induced fission,  $(n,f)$ , is a very powerful tool for studying nuclear structure.

Neutron-induced reactions are also crucial to the field of nuclear astrophysics, for understanding the abundance of heavy elements that were produced in different stages of stellar evolution in the universe, because they are directly related to the  $(n,\gamma)$  cross sections.

Nuclear data on neutron-induced fission are also of primary importance for developing new solutions to current questions related to power generation in nuclear power plants. Among other possible sources, nuclear energy plays an important role in the ever-increasing demand for electricity. New concepts

in nuclear energy production are being investigated in order to improve the efficiency of energy production, the safety of nuclear power plants and the treatment of nuclear waste.

## Nuclear data needs for energy production

The main disadvantages of power production by nuclear fission are the low burning efficiency of current nuclear fuel and the long-term radiotoxic nuclear waste by-products composed of long-lived actinides and fission fragments. In the currently operating nuclear fission reactors, the spent fuel elements account for the largest part of the nuclear waste in terms of radiation activity. In addition to uranium, the waste consists of fission products and isotopes of plutonium and minor actinides like neptunium, americium and curium. After a cooling period, needed to diminish the activity of the spent fuel, mainly of the short-lived fission products, sometimes is possible to extract the uranium and plutonium which can be re-used as fuel. In any case, the remaining material is considered as waste. The high activity and the long lifetime of several isotopes present in the nuclear waste require long term storage under safe conditions on a very long time scale, reaching several hundreds of thousands of years.

Natural uranium is composed primarily of  $^{238}\text{U}$  and a mere 0.72% of  $^{235}\text{U}$ , which is the fissile material. The amount of  $^{235}\text{U}$  in enriched uranium, the most widely used nuclear fuel, is between 2% and 4%. Only a small fraction of natural uranium is actually useful in producing energy, and global uranium reserves are limited; so this must be considered a non-renewable energy source.

Additionally, the waste generated in power production includes fission products, such as  $^{137}\text{Cs}$ ,  $^{90}\text{Sr}$ , and plutonium and minor actinides such as americium and curium, which are produced by neutron capture in the fuel and subsequent beta decay. These heavy nuclear fuel products decay mainly by  $\alpha$  emission and have very long lifetimes. Such residues must be isolated from biological systems for their entire active life, which can involve millions of years [5]. Even if storage of those materials in geological deposits were considered a valid solution, the ever-increasing amount of waste would soon make such an alternative insufficient, becoming nuclear waste management one of the main problems of nuclear energy production.

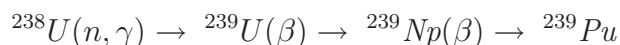
For this reason, nuclear waste transmutation has been proposed as a way to reduce substantially the quantity of the long-lived isotopes in the

nuclear waste, mainly the transuranic ones. Transmutation of actinides is proposed to take place by fission in nuclear systems like critical reactors or sub-critical Accelerator Driven Systems (ADS). In most of the scenarios, the use of fast neutron energy spectra and specific fuel compositions are proposed. In addition, the transmutation of long-lived fission products has also been proposed using neutron absorption, mainly by radiative capture with thermal and epithermal neutrons.

At present, there are several generations of nuclear reactors in operation. Generation III (and 3+) nuclear reactors incorporate important improvements with respect to the original designs of Generation II commercial reactors, which were built through the end of the 1990s. The main improvements are related to greater efficiency and the installation of passive safety features that require no active control or operation to avoid accidents in the event of a failure. Nevertheless, they maintain the original nuclear energy production concept of the earliest reactors.

Future Generation IV facilities mark a dramatic change in the concept of nuclear energy production. They are still in the design and development stage, and not expected to be available for commercial use before 2030. Although some of the Generation IV concepts have been deliberated for decades, international collaboration officially began in 2000 with the creation of the Generation IV International Forum (GIF), which seeks to establish the feasibility and performance capabilities of innovative nuclear energy systems [7]. In 2002, six reactor technologies were selected as candidates for future implementation in nuclear energy. Three of these are Fast Neutron Reactors (FNR), one is not an FNR but can be made to function like one, and the other two use low energy neutrons.

Most of today's nuclear plants operate with slow neutrons because the fission cross section of  $^{235}\text{U}$  is very high at those energies. However, Fast Reactors or Fast Breeder Reactors (FBR) mainly use plutonium as the fissile material because of its higher fission cross section with fast neutrons that maintain the fission chain.  $^{239}\text{Pu}$  can be obtained from  $^{238}\text{U}$  (the most abundant uranium isotope) by neutron-capture and two subsequent  $\beta$  decays, in what is called the uranium-plutonium fuel cycle:



There is an additional interest in fast reactors because of their ability to incinerate minor actinides, thus reducing the quantity of long-lived radioactive nuclear waste. Updated information on the status of nuclear technologies and the efforts of different countries can be found on the World Nuclear Association website (see Ref. [8]).

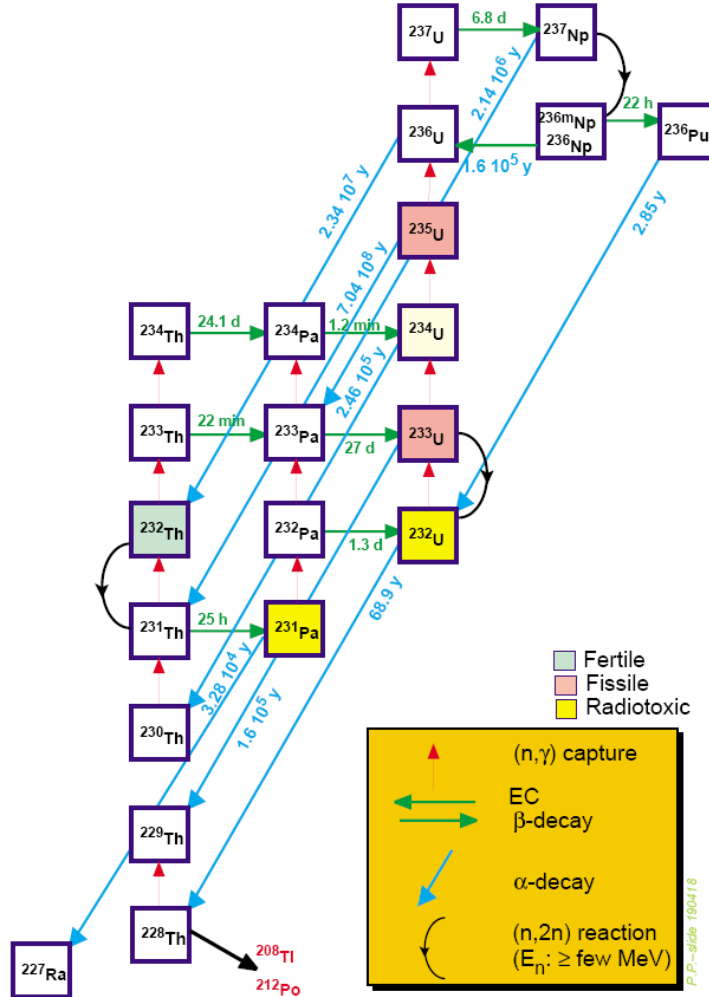


Figure 1: Schematic view of the thorium cycle [6].

A different approach is to reduce dramatically the amount of nuclear waste, specially the actinides, by using a fuel cycle based on  $^{232}\text{Th}$ , which is the only naturally existing thorium isotope and about three times more abundant than uranium. The  $^{232}\text{Th}$  is not fissile but, after a reaction initiated by the capture of a neutron, the fissile  $^{233}\text{U}$  is formed:



During neutron irradiation, the  $^{233}\text{U}$  produced in the reaction begins to fission and can produce neutrons that sustain the reaction. This is called the thorium cycle [9, 10] and is shown in Fig. 1. This cycle has been proposed for implementation in thermal reactors, fast reactors and ADS systems.

An Accelerator Driven System (ADS) is a subcritical system driven by accelerators that uses spallation reactions of high-energy protons on a heavy target (made of lead, bismuth or tantalum) to produce the amount of neutrons needed to maintain the nuclear reaction chain [11]. If a problem arises, automatic shutdown of the accelerator is enough to stop the reaction and minimize the risk of an accident.

Another advantage of the ADS is that plutonium and minor actinides can be transmuted by admixing them into the nuclear reactor fuel. Fission of those nuclei is induced by the neutrons, resulting in a huge reduction of the radiotoxicity as their fission fragments has much shorter half-lives (typically, hundreds of years) than those of the original nuclei (possibly millions of years). This dramatically reduces the dimensions of the problem of long-term storage of nuclear waste.

In order to validate different fuel cycles and reactor concepts, their performance must be studied by means of simulations that include accurate data on the nuclear reactions involved. Data currently available in different nuclear libraries are derived from evaluations based on both experimental data and theoretical predictions from nuclear models. The cross sections given in different evaluations are frequently incompatible among themselves. Accurate data on cross sections for neutron-induced reactions on different isotopes will make it possible to use new technologies that will improve the present situation in nuclear energy production. New measurements on  $(n,\gamma)$  and  $(n,f)$  reactions are required for the main isotopes involved in the thorium cycle and for the long-lived isotopes and fission products involved in the transmutation process. These measurements should include energies ranging from thermal neutron energy to hundreds of MeV.

Nuclear data on the Th cycle isotopes received little attention in the past, compared to the isotopes of the uranium-plutonium cycle. Most of the experimental data for  $^{232}\text{Th}$  were measured in the 1970-1980s and present greater discrepancies than the uncertainties permitted for their consideration in the development of nuclear power plants.

A compilation of experimental measurements can be found in the Experimental Nuclear Reaction Data (EXFOR) database [12]. EXFOR is an open-access data library that stores experimental reaction data, including how the measurements were done, bibliographic references and information on updates of the numerical data. Maintenance of this database is coordinated by the Nuclear Data Section (NDS) of the International Atomic Energy Agency (IAEA).

In addition to EXFOR there are several major libraries containing nuclear

data evaluations based on experimental data and nuclear model calculations, such as:

- The Evaluated Nuclear Data File (ENDF), latest version: ENDF/B-VII.1 (released in 2011) [13].
- The Japanese Evaluated Nuclear Data Library (JENDL), latest version: JENDL-4.0 [14]. Its High-Energy sub-library (JENDL/HE-2007) provides values for proton- and neutron-induced reactions up to 3 GeV [15].
- The Joint Evaluated Fission and Fusion File (JEFF), latest version: JEFF-3.1.2 [16].
- The Russian Evaluated Neutron Reaction Data Library (BROND), latest version: BROND-2.2 [17].
- The Chinese Evaluated Nuclear Data Library (CENDL), latest version: CENDL-3.1 [18].

The Nuclear Energy Agency (NEA) of the Organisation for Economic Co-operation and Development (OECD) has elaborated a High Priority List for the most urgent nuclear data needed to improve present evaluations related to the development of the nuclear energy industry. This list is subject to continuous change due to new requests from different fields, and is available at the website cited in Ref. [19].

The IAEA Nuclear Data Center (NDC) has also made several recommendations for improving the quality of nuclear data for materials relevant to the thorium fuel cycle, specifically  $^{232}\text{Th}$ ,  $^{231,233}\text{Pa}$  and  $^{232,233,234,236}\text{U}$  [20, 21].

## The status of $^{232}\text{Th}(n,f)$

The different aforementioned evaluations of the  $^{232}\text{Th}(n,f)$  cross section are presented in Fig. 2, where large discrepancies are evident. To begin, the ENDF/B-VII.1 evaluation includes neutron energies up to 60 MeV, while the others stop at 20 MeV, and only the BROND-2.2 library provides evaluated values for the subthreshold fission resonances. There are also very large differences among all the evaluations up to 1 MeV and only the ENDF/B-VII.1 (based on the work done in [22], where a theoretical model including a triple-humped fission barrier was used to describe fission on light actinides) shows the fine structure in the region between 500 keV and 1 MeV. The region

of vibrational resonances between 1 MeV and 3 MeV exhibits different peak heights in Fig. 2(b) with differences up to 20%. Above those energies, all the evaluations present a similar shape, with differences of around 10%. This discrepancy is too great: accuracy within a 1% percent is needed [10] for this cross section in a fast reactor, which makes new, precise measurements and evaluations a necessity.

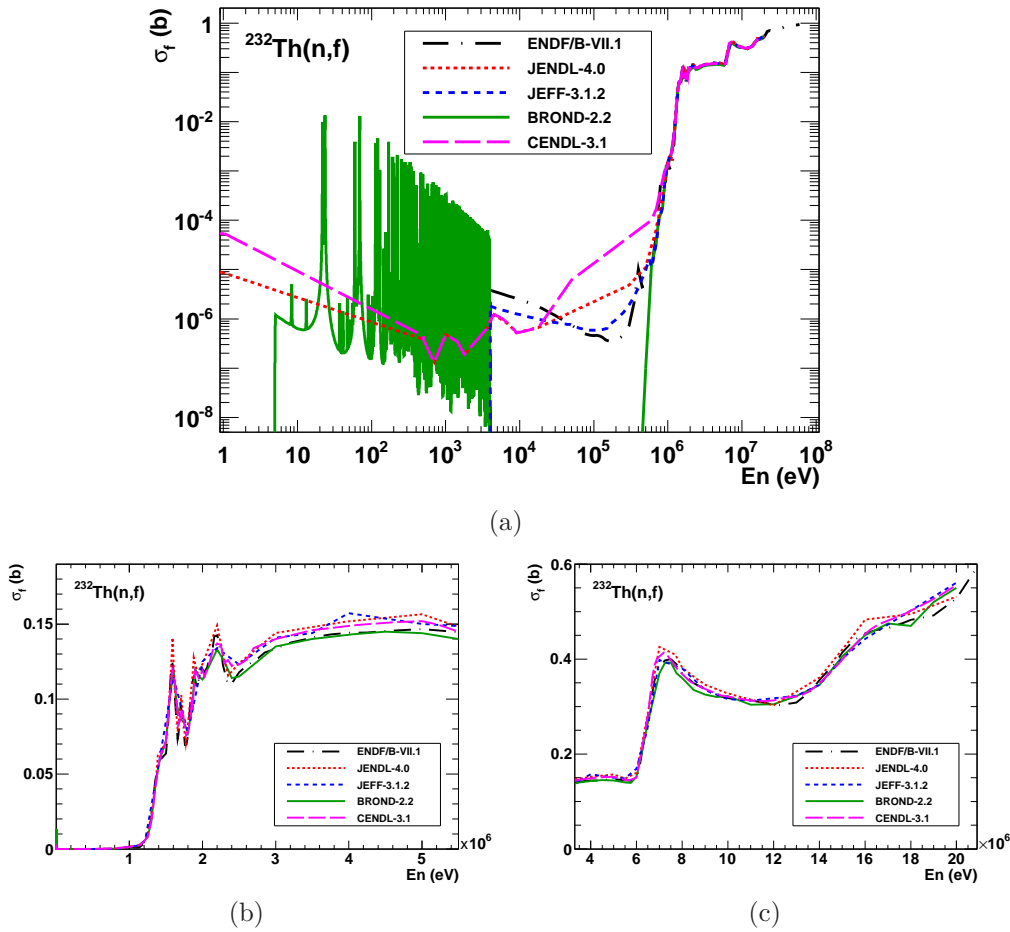


Figure 2: Different evaluations for the neutron-induced fission cross section of  $^{232}\text{Th}$  [13, 14, 16–18]. Large discrepancies existing below 1 MeV are seen in (a). The region of vibrational resonances shown in (b) exhibits differences of as much as 20%, being of around 10% for the above energies up to 20 MeV (c). ENDF/B-VII.1 is the only evaluation that provides data up to 60 MeV.

Apart from its relevance in developing advanced nuclear fuel cycles, the  $^{232}\text{Th}(n,f)$  reaction is also very interesting from a purely theoretical point of view. Several light actinides, such as  $^{230}\text{Th}$ ,  $^{232}\text{Th}$ , and  $^{234}\text{U}$ , are known to

present a behaviour called “the thorium anomaly” [23], that is the impossibility of describing the structure of their narrow resonances in the threshold region using a double-humped barrier, making necessary to include a third minimum.

The fission fragment angular distribution is an important observable for understanding the fission mechanism; particularly for studying the quantum properties of the levels of fissioning nuclei for a given  $J$  and  $K$  (total spin and its projection on the fission axis) when considering energies close to the thresholds of the different multiple-chance fission channels. This information is useful to determine a unique set of the fission barrier parameters, as it was pointed out in [22].

Apart from the theoretical implications, the strong anisotropies observed at these thresholds of neutron emission before fission affect also to the fission cross section measurements due to the angular limitation of the detectors.

The evolution of the angular distribution with the neutron energy is usually characterized by the anisotropy parameter, which is defined as the ratio of the number of fission fragments emitted at  $0^\circ$  and at  $90^\circ$  with respect to the neutron beam direction. The experimental data currently available in the EXFOR database for  $^{232}\text{Th}(n,f)$  anisotropy are shown in Fig. 3, where most measurements are concentrated around the fission threshold region (1-2 MeV). Above this region, data are scarce and exhibit large uncertainties, so that little is known about the fission fragment angular distribution for the  $^{232}\text{Th}(n,f)$  reaction.

## Experimental program at CERN-n\_TOF

The Neutron Time of Flight (n\_TOF) facility was built at CERN [24, 25] in order to improve the accuracy of nuclear data required for advanced nuclear technologies and nuclear astrophysics. The n\_TOF has a long flight path and an intense spallation neutron source [26] that covers a continuous energy range from thermal to 1 GeV, with great accuracy. The high-intensity neutron flux makes it possible to measure cross sections of neutron-induced reactions in highly radioactive materials.

A specific experimental program for measuring neutron-induced fission cross sections of isotopes relevant to the thorium fuel cycle is in progress at CERN [6, 27]. As part of this program, the work for the thesis presented here focused on the study of the  $^{232}\text{Th}(n,f)$  reaction in an experiment to measure the angular distribution of the fission fragments and the cross section

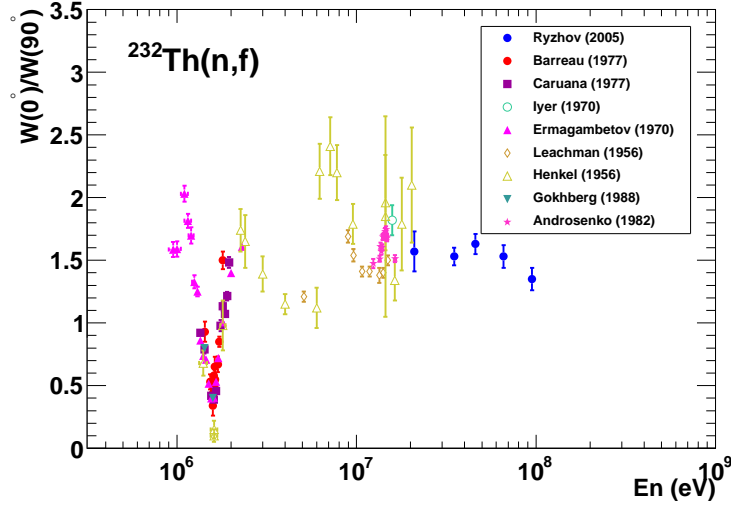


Figure 3: Available EXFOR experimental data on the anisotropy parameter for  $^{232}\text{Th}(n,f)$ . Scant data and large uncertainties are encountered outside the region of the fission threshold.

of the reaction. The aim of the present work was to extract and analyse the data from that experiment. The high-resolution neutron energy at the n\_TOF facility makes it possible to experimentally measure the vibrational resonances at the fission threshold [28]. The study of those resonances in the fission cross section and the variations in the angular distribution will increase understanding of the thorium anomaly.

The PPAC-based detection setup was specifically designed for the n\_TOF experiments. Double-gap PPACs with two stripped cathodes make it possible to determine the impact point, and therefore the trajectory, of the fission fragments. A geometrical configuration of targets and detectors tilted at  $45^\circ$  with respect to the neutron beam was used in this experiment, in order to detect fission fragments emitted at any angle between  $0^\circ$  and  $90^\circ$ .

## This work

This introductory chapter has provided a description of the motivation behind the interest in obtaining accurate measurements of the  $^{232}\text{Th}(n,f)$  reaction. I will conclude with a short description of the remaining sections of this thesis:

- Chapter 1 is devoted to the physics of the nuclear fission process, es-

pecially as it relates to the origin of the observed angular distribution of the emitted fragments. An overview of most widely-used nuclear models is included, followed by an explanation of the non-isotropic behaviour of emitted fragments.

- Chapter 2 describes the n\_TOF facility at CERN and the experimental setup used for this experiment, including the detectors and the targets.
- Chapter 3 explains the first stages of data analysis, including the procedure for identifying fission events from the raw data and extracting information relevant to them, such as the neutron energy calculation or the X-Y position of the hits in the detectors.
- Chapter 4 describes the simulation work done with Geant4 to calculate the detection efficiency and compares this experimental setup with the one used in n\_TOF Phase 1.
- Chapter 5 contains the final stages of the data analysis and the results obtained for the angular distribution of the fission fragments in  $^{232}\text{Th}(n,f)$  reactions, as a function of the neutron energy from fission threshold up to 1 GeV. The anisotropy parameter, defined as the ratio of the number of emitted fragments at  $0^\circ$  with respect to  $90^\circ$ , is calculated and compared with previous experimental data from other authors. The fission cross section for  $^{232}\text{Th}$  is also provided and compared with previous experimental data available in the EXFOR database and other evaluations.
- Finally, the main conclusions of this work are summarized.

# Chapter 1

## The nuclear fission

Nuclear fission reaction is commonly defined as the process by which a nucleus is split into two fragments of comparable mass. Historically, barium isotopes were detected in uranium that had been irradiated with neutrons in a 1938 experiment by O. Hahn and F. Strassmann [29]. That same year, L. Meitner and O. R. Frisch were the first to explain this phenomenon [30] by terms of a splitting of a vibrational liquid drop into two smaller ones, in a process that they called, for the first time, *fission*, in analogy to the cellular division. Soon after, in 1939, N. Bohr and J. A. Wheeler [31] provided the first complete theoretical description of the process improving the so called Liquid Drop Model (LDM). A brief history of the first experimental evidences that led to the discovery of fission can be found in Ref. [32].

There is a great variety of nuclear structure models at very different theoretical levels. None of the successive attempts to develop a model based on ab-initio theories has been, up to date, successful. Therefore, to perform nuclear-reaction calculations one must turn to theories based on effective potentials that leave a set of parameters to be tuned, relying strongly on phenomenological inputs. More and more accurate experimental data are required, therefore.

An extensive description of the fission process is beyond the scope of this thesis work, though detailed descriptions of the theoretical frameworks and experimental works are widely available [33, 34]. An overview of the features of fission relevant to the work of this thesis is presented here.

## 1.1. The Single Particle Model

Nuclei represent a many-body problem that cannot be solved analytically. Even more, the interaction between nucleons inside the nucleus has not a known analytical formula and, therefore, some approximations and assumptions are necessary. Nucleons inside a nucleus are kept tied together by residual strong forces that at close enough distances are more intense than the Coulomb repulsion. Nevertheless, as both the Coulomb field and the spin momenta are governed by the electromagnetic conservation rules, we are interested in solving the time-independent Schrödinger equation:

$$\hat{H}\psi = E\psi \quad (1.1)$$

where  $E$  is the total energy of the system, and the Hamiltonian operator  $\hat{H}$  takes into account the sum of the kinetic and potential energies of all the nucleons. Different approaches to this problem are described in most textbooks on nuclear physics [35–37]. A first approximation is to assume that the potential  $V$  experienced by each nucleon  $i$  is due to the interaction with all other nucleons individually. So that, for a nucleus containing  $A$  nucleons, Eq. (1.1) can be written as:

$$\hat{H}\psi = \left[ \sum_{i=1}^A \hat{T}(i) + \sum_{i=1, j>i}^A \hat{V}(i, j) \right] \psi = E\psi \quad (1.2)$$

The Single Particle Model (SPM) assumes, basically, that the force experienced by every nucleon inside the nucleus is due to the average field created by the others, as it is done in the atomic Hartree approximation. In a coarse approximation, one can take as if each nucleon were seeing the same potential  $V_{SP}$  and behaving as an independent particle in the nucleus. The total Hamiltonian  $H_{IPM}$  would be the sum of the Hamiltonians for all  $A$  nucleons:

$$\hat{H}_{IPM} = \sum_{i=1}^A \left[ \hat{T}(i) + \frac{1}{2} \hat{V}_{SP}(i) \right] \quad (1.3)$$

By adding and subtracting the total potential from Eq. (1.3) to Eq. (1.2), we get:

$$\hat{H}\psi = \left\{ \hat{H}_{IPM} + \left[ \sum_{i=1, j>i}^A \hat{V}(i, j) - \sum_{i=1}^A \frac{1}{2} \hat{V}_{SP}(i) \right] \right\} \psi = E\psi \quad (1.4)$$

If the difference between both potentials is small, the model will be more realistic and the eigenfunction  $\psi$  will approximately describe the eigenfunction of the real nucleus so that it can be assumed that the unknown nucleon-nucleon interactions can be treated as perturbations and approached in a Hartree-Fock fashion.

Following this single particle approximation, the Schrödinger equation for a nucleon within an average spherically-symmetric potential, is:

$$-\frac{\hbar^2}{2\mu} \nabla^2 \Psi + V(r, s)\Psi = E\Psi \quad (1.5)$$

where the potential  $V(r, s)$  depends on the radial coordinate and on the spin. We restrict ourselves to time-independent (or stationary) solutions that can be factorized in terms depending on the radial coordinate  $r$  and on the spin  $s$ :

$$\Psi = \psi(r)\chi(s) \quad (1.6)$$

In this way, we have  $A$  independent Hartree equations in the following form:

$$\frac{\hbar^2}{2\mu} \nabla^2 \psi(r)\chi(s) + [E - V(r, s)]\psi(r)\chi(s) = 0 \quad (1.7)$$

To solve Eq. (1.7) we need to know the potential  $V(r, s)$ . For the sake of simplicity one can start by assuming that it can be described as an average, spherically-symmetric central potential  $V(r)$ , being the spin-dependent energy small enough in magnitude to be treated separately as a perturbation. Let us consider factorized solutions of the form:

$$\psi(\vec{r}) = \psi(r, \theta, \phi) = R(r)Y(\theta, \phi) \quad (1.8)$$

and so we can write separated equations for the radial and the angular dependences:

$$\frac{1}{R} \frac{\partial}{\partial r} \left( r^2 \frac{\partial R(r)}{\partial r} \right) + \frac{2\mu r^2}{\hbar^2} [E - V(r)] = \lambda \quad (1.9)$$

$$\left[ \frac{1}{\sin \theta} \frac{\partial}{\partial \theta} \left( \sin \theta \frac{\partial Y(\theta, \phi)}{\partial \theta} \right) + \frac{1}{\sin^2 \theta} \frac{\partial^2 Y(\theta, \phi)}{\partial \phi^2} \right] = -\lambda Y(\theta, \phi) \quad (1.10)$$

### 1.1.1. Angular equations

Note that in this approximation the angular part of the wave function  $Y(\theta, \phi)$  is completely independent of  $V$  and so, valid for any  $V(r)$ , provided that the interaction potential does not depend on the angular coordinates

$\theta$  and  $\phi$ . The angular wave functions  $Y(\theta, \phi)$  will be the same for all the potentials  $V(r)$  and can be known exactly, although when the energies of the levels are not accurately known, because of the unknown radial behaviour of the interaction. These functions define both the angular momentum and the parity of the wave functions.

The normalized functions  $Y(\theta, \phi)$  are known as the spherical harmonics, and have the form:

$$Y_{l,m}(\theta, \phi) = (-1)^m \left[ \frac{(2l+1)(l-m)!}{4\pi(l+m)!} \right]^{1/2} e^{im\phi} P_l^m(\cos\theta) \quad (1.11)$$

where  $l$  and  $m$  are integers, with  $l \geq 0$  and  $|m| < l$ .

It is customary to say that  $l$  is the angular momentum quantum number, being  $m$  its z-component, what is correct as far as the earlier approximations were true.

### Angular momentum

The operator for the z-component of orbital angular momentum is given by:

$$\hat{L}_z = -\frac{i}{\hbar} \frac{\partial}{\partial \phi} \quad (1.12)$$

and the operator for the square of the total orbital angular momentum is:

$$\hat{L}^2 = -\hbar^2 \left[ \frac{1}{\sin\theta} \frac{\partial}{\partial \theta} \left( \sin\theta \frac{\partial}{\partial \theta} \right) + \frac{1}{\sin^2\theta} \frac{\partial^2}{\partial \phi^2} \right] \quad (1.13)$$

A straightforward comparison with Eq. (1.10) gives us:

$$\hat{L}^2 Y(\theta, \phi) = \lambda \hbar^2 Y(\theta, \phi) = l(l+1) \hbar^2 Y(\theta, \phi) \quad (1.14)$$

Here we have used that  $\lambda = l(l+1)$ , where  $l$  is the orbital angular momentum quantum number. We have shown that the spherical harmonics are eigenfunctions of the squared total orbital angular momentum operator as well as for the z-component of the orbital total momentum:

$$\hat{L}_z Y(\theta, \phi) = -\frac{i}{\hbar} \frac{\partial}{\partial \phi} Y(\theta, \phi) = \frac{1}{\hbar} m Y(\theta, \phi) \quad (1.15)$$

It must be noticed that these calculations have been done under the assumption of a spherically-symmetric central potential and so, it is only

in this case when the angular part of the Schrödinger equation (Eq. (1.4)) does not depend on the potential  $V(r)$ . Many heavy nuclei are showing ellipsoidal shapes rather than spherical, leading to rotational symmetry about the unequal principal axis (we will call it the  $z$  axis). The potential  $V$  is, in such a case, a function of the nuclear matter distribution so that it is also function of  $\theta$  and therefore the total orbital angular momentum is not longer a good quantum number. However, as long as the potential do not depend on the angle  $\phi$  due to the rotational symmetry about the  $z$  axis, the  $z$  component of the angular momentum is conserved and  $m$  is still a good quantum number. This quantum number is usually called  $\Omega$ , because  $m$  is reserved for the component of the angular momentum along an axis defined by the magnetic field, whereas the symmetry axis of the nucleus could not be fixed in space.

### 1.1.2. The radial equation

Different approaches can be used to describe the radial part of the interaction potential that is included in Eq. (1.9). For spherical nuclei, a quite realistic central potential is the Woods-Saxon potential. It is based on the fact that the nuclear matter has a certain distribution inside the nucleus, with a density of mass and charge that is nearly constant inside heavy nuclei and falls smoothly to zero over a dimension of the order of the femtometer ( $1 \text{ fm} = 10^{-15} \text{ m}$ ). The dependence of the mass density with the radius can be described by:

$$\rho(r) = \frac{\rho_0}{1 + e^{\frac{(r-R)}{a}}} \quad (1.16)$$

where  $R = r_0 \cdot A^{1/3}$  (being  $r_0 \approx 1.2 \text{ fm}$ ) and  $a \approx 0.55 \text{ fm}$ .

So that the Woods-Saxon potential takes the form:

$$V(r) = -\frac{V_0}{1 + e^{\frac{(r-R)}{a}}} \quad (1.17)$$

Despite the simplicity of this formula, Eq. (1.9) cannot be solved analytically with this potential but, nevertheless, it can help to find a good approximation.

For heavy nuclei it can be assumed that the potential is constant at the central value up to a well defined nuclear radius, where it vanishes. In this approach, a simple spherical potential well can be used having so an analytical solution. However, for the light nuclei, this is quite a poor approximation since there is no region where the potential can be assumed constant. In this

case, the three-dimensional isotropic harmonic oscillator can be taken as a good approximation. The problem is that this potential is not so realistic, as it increases infinitely, but it can be solved analytically and the solutions remains confined inside the well. In any case it is a good approximation for the lower vibrational levels.

The potential of the isotropic harmonic oscillator can be written in the form:

$$V_{IHO} = -V_0 + \frac{1}{2}\mu\omega^2 r^2 \quad (1.18)$$

where  $V_0$  represents the depth of the potential well and  $\mu$  is the reduced mass of a nucleon.

If we solve the Schrödinger Eq. (1.9) with this potential, we obtain the following discrete values of the energy levels:

$$E_N = -V_0 + \hbar\omega \left( N + \frac{3}{2} \right) \quad (1.19)$$

where  $N$  is a positive integer, named “major shell number” into the frame of the Shell Model.  $N = 2k + l$ , where  $k$  is the order of the Legendre polynomial associated to the radial wave function  $R(r)$ , and  $l$  is the quantum number corresponding to the orbital angular momentum.

## 1.2. Self-consistent mean field model

In the mean field theory, the Hartree-Fock approach starts from a Hamiltonian containing both  $n$  kinetic energy terms, and potential terms. In this first hypothesis, the potential term of the Hamiltonian must include all possible two-body interactions in the set of  $n$  nucleons subjected to the Pauli principle that were neglected in Eq. (1.5). The second step assumes that the wavefunction of the system can be written as a Slater determinant of one-particle spin-orbitals. This mathematical translation of the independent-particle model being treated as fermions is the second hypothesis. The components of this Slater determinant, or the individual wavefunctions of the nucleons, must be ascertained. To this end, the third hypothesis assumes that the total wavefunction (the Slater determinant) leads to an energy minimum. The resulting Schrödinger equation on the (unknown) Slater determinant must therefore be computed, imposing that its mathematical variation must vanish, which leads to a set of coupled equations (the Hartree-Fock equations) where the unknowns are the individual wavefunctions. Solving

this system of equations provides a set of (false) individual nucleon wavefunctions, and thus the total energy of the nucleus is derived. In fact, this gives us a total energy functional that is dependent on the individual wavefunctions. Everything is then done to optimize the choice of these wavefunctions so that the functional has a minimum. It should be noted that the energy is a functional of a “density function”, which is defined as the sum of the individual squared wavefunctions. This is similar to the electron shell model, where the total Coulomb energy is proportional to the density of charge.

The process of solving the Hartree-Fock equations can only be iterative, since the potential energy terms depend on the density functions, which are precisely the wavefunctions to be determined. The algorithm starts with a set of grossly reasonable wavefunctions (usually the eigenfunctions of a harmonic oscillator, as defined in the previous section). From these, the density functions can be calculated and then, the Hartree-Fock potential. Once this done, the Schrödinger equation is solved anew, and the process is repeated. Convergence is reached when the difference in the energy values of two successive iterations is less than a certain value. The mean field potential is then completely determined and the corresponding Hamiltonian is known as the Hartree-Fock Hamiltonian.

The problem that remains unresolved in the Single Particle Model is how to introduce nucleon-nucleon interactions. In contrast with atomic physics, where the Coulomb interaction is analytically known, the nucleon-nucleon interaction inside the nucleus is not. This problem can be overcome by defining an *effective nucleon-nucleon interaction* and inserting it into the Hartree-Fock calculations, providing a minimal set of parameters that incorporates the essential physics. Since the interaction is phenomenological, these parameters need to be determined from experimental data.

The Skyrme’s interaction force was introduced in the seminal work of Vauthrein and Brink [38] and has been widely used since then. It gives a density-dependent potential function that depend on the distance between nucleons, that is, on the nucleon density. By adjusting a set of up to ten parameters, nuclear properties can often be derived in a rather simple and reliable way, even for the heaviest nuclei or nuclei far from the stability line [39]. In the so-called Skyrme-Hartree-Fock (SHF) model, there is a nucleon pairing effect in addition to the nucleon-nucleon interaction mentioned above.

Historically, this hypothesis was introduced after nuclei with even numbers of nucleons were systematically observed to be more strongly bound than those with an odd number. The first theoretical description of nuclear pairing was proposed at the end of the 1950s by Aage Bohr and Ben Mot-

telson (which led them to receive a Nobel Prize in Physics in 1975). The very simple idea is that nucleons bind with another to form pairs. When the nucleus has an even number of nucleons, each nucleon finds a partner. To excite such a system, there must be at least enough energy to break a pair. However, with an odd number of nucleons, exciting the unpaired “bachelor” nucleon requires less energy.

Theoretically, this mentioned pairing phenomenon can be combined with the mean field theory previously described, so that nucleons are subject to both the mean field potential and to pairing interaction, even though independently, since they proceed from the same nucleon-nucleon interaction. The Hartree-Fock-Bogolyubov (HFB) approach was developed to include the mean field, the pairing and their mutual links in a unified formalism. In the absence of pairing, the HFB equations reduce to the SHF equations.

In nuclear astrophysics, the increasing need to determine cross sections of nuclei far from stability represents a challenge for nuclear reaction models [40]. Predictions of cross sections have generally relied on more or less phenomenological approaches, and depended on parameters adjusted to available experimental data or deduced from systematic relations. While such predictions are quite reliable for nuclei not too far from the experimentally known regions, it has long been recognised that self-consistent mean-field methods with effective nucleon-nucleon interactions can be very successfully applied for this purpose [41]. A description of nuclear properties over the entire nuclear chart requires theoretical methods that are both microscopically functional and computationally tractable. With this purpose, semi-microscopic nuclear models based on the Hartree-Fock-Bogoliubov (HFB) method have been developed [42, 43] and fully microscopic (or semi-microscopic) cross section calculations were performed, using the nuclear reaction parameters given by the TALYS<sup>1</sup> or EMPIRE<sup>2</sup> nuclear reaction codes [46, 47].

### 1.3. The Liquid Drop Model

In the Single Particle Model described in the previous section the angular momentum appears as having well defined quantum numbers and gives a fair description of the nuclear energy levels for those nuclei in the vicinity of the “magic numbers”. The Nilsson approach [48] extends the single particle

---

<sup>1</sup>TALYS is a software package for the simulation of nuclear reactions induced by light particles in the 1 keV - 200 MeV range [44].

<sup>2</sup>EMPIRE is a modular system of nuclear reaction codes, and designed for calculations over a broad range of energies and incident particles [45].

model to deformed nuclei by using deformed harmonic oscillator potentials to give energy levels that depends on the deformation. However, when dealing with large deformations, the results produced by the approximation of a central field are less accurate. Unlike the single particle model, the Liquid Drop Model (LDM) that is presented in this section provides a macroscopical description of the nucleus, comparing it to a uniformly charged liquid drop in which the deformation produced by an excitation can be lead to a division in two smaller nuclei, as a result of an increase in the surface energy smaller than the decrease in the Coulomb energy. This first description of the fission process based on the calculation of the potential energy of the nucleus as a function of its shape was formerly developed by L. Meitner and O. R. Frisch in 1938 [30] and improved by N. Bohr and J. A. Wheeler [31] in 1939.

In this model, the energy of the nucleus is given by the sum of a volume energy  $E_V$  proportional to the mass number, the surface energy  $E_S$  proportional to the surface area of the drop and the Coulomb energy  $E_C$ :

$$E = E_V + E_S + E_C \quad (1.20)$$

As the nuclear density is almost constant all along the nuclear chart, the nuclear radius is proportional to  $A^{1/3}$ , and the standard semiempirical formula for nuclear ground-state energies can be written in the form:

$$E = -C_1 A + C_2 A^{2/3} + C_3 (Z^2/A^{1/3}) \quad (1.21)$$

A pairing energy  $E_P$  can be added to take into account the nucleons structure of odd-even nuclei. This small correction is usually taken in the form  $E_P = 11 \cdot A^{-1/2} (MeV)$  to be added or subtracted for doubly odd or doubly even nuclei, respectively. Moreover, as Myers and Swiatecki [49] suggested, a isospin-dependent correction should be added:

$$C_1 = a_1 [1 - \gamma (N - Z/A)^2] \quad (1.22)$$

$$C_2 = a_2 [1 - \kappa (N - Z/A)^2] \quad (1.23)$$

where the many involved parameters are determined from experimental data.

Since the nucleus is assumed to be incompressible, only the surface and Coulomb terms are relevant to the deformation energy, that will be given by:

$$E_{def} = E_S(\epsilon) + E_C(\epsilon) - E_S(0) - E_C(0) \quad (1.24)$$

where  $\epsilon$  represents some combination of the coefficients  $a_{\lambda\mu}$  describing the deformation by a multipole expansion of the nuclear radius in terms of spherical

harmonics:

$$R(\theta, \phi) = R_0 \left[ 1 + \sum_{\lambda, \mu} a_{\lambda\mu} Y_{\lambda\mu}(\theta, \phi) \right] \quad (1.25)$$

If we assume small distortions limited to pure quadrupole deformation (only  $a_{20} \neq 0$ ), the surface and the Coulomb energies are given by:

$$\begin{aligned} E_S(\epsilon) &= E_S(0) \cdot (1 + 2/5 a_{20}^2) \\ E_C(\epsilon) &= E_C(0) \cdot (1 - 2/5 a_{20}^2) \end{aligned} \quad (1.26)$$

The charged liquid drop will be stable against small distortions if the decrease in the Coulomb energy is smaller than the increase in the surface energy:  $\Delta E_C > \Delta E_S$ . This is always true if  $E_C(0)/E_S(0) < 2$  leading to the introduction of the so-called *fissility parameter*  $x$  [31]:

$$x = \frac{E_C(0)}{2E_S(0)} \quad (1.27)$$

Numerical calculations for these terms give the typical value:

$$x \approx \frac{1}{50} \cdot \frac{Z^2}{A} \quad (1.28)$$

so that nuclei with  $Z^2/A > 50$  give values of  $x$  greater than unity, being unstable against spontaneous fission. The same result can be obtained by using exact expressions for the Coulomb energy of an ellipsoidal nuclei [35].

Huge efforts over more than 40 years have been devoted to the computation of the deformation energy of the nucleus in terms of the liquid drop model, most of them concentrated on drops with  $x = 0.7 - 0.8$ , which are the typical values of the actinide nuclei. In Fig. 1.1 (taken from [23]) a schematic diagram of potential energy contours is shown in the plane defined by two of the commonly used deformation parameters, related to the quadrupole and hexadecapole coefficients in a Legendre polynomial expansion (see Appendix A) of the liquid drop surface. The energetically most favorable path towards fission is indicated by the broken line and the potential energy barrier presented along this path is shown in the lower panel.

For  $x < 1$ , the deformation energy has a local minimum for the spherical shape so that the LDM will predict spherical ground states for all stable nuclei, what it is not true for the actinides specially, which present values of  $x \sim 0.7 - 0.8$ . For these values of  $x$ , and positive values of the quadrupole

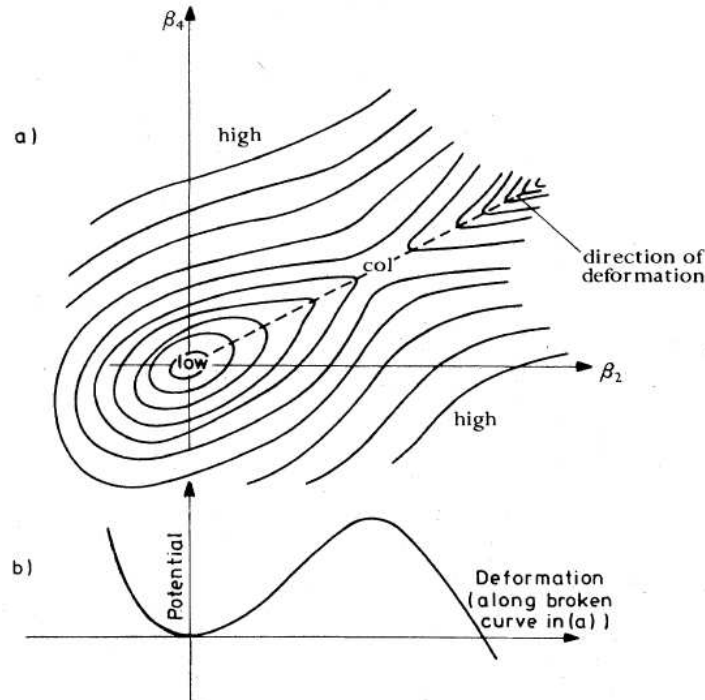


Figure 1.1: Potential energy contours as a function of the quadrupole and hexadecapole deformation parameters (upper panel). The potential energy barrier along the most favorable path towards fission is indicated in the lower panel (Fig. from [23]).

deformation term  $a_{20}$ , the deformation energy presents a saddle point with positive energy with respect to the ground state. Different shapes of the nucleus at the saddle point for different values of  $x$  are shown in Fig. 1.2 [5]. As  $x$  decreases from 1 to 0.7, the nucleus becomes more cylindrical and, below 0.7, at the saddle point configuration develops a well-defined neck whose rupture (at  $x = 0$ ) will cause the scission of the two fragments.

For the case of light actinides, the fission barrier is low enough to allow fission to be induced by simply exciting the nucleus to energies above the fission barrier. For instance, a thermal neutron provides energy enough to  $^{235}\text{U}$  fissions, through the formation of the compound nucleus  $^{236}\text{U}$ . Spontaneous fission is also possible in actinides by quantum tunneling of the barrier. This effect becomes more probable as the nuclear charge increases, since the height of the fission barrier decreases.

Despite some improvements made to the model, such as the inclusion of a diffuse nuclear surface and the finite compressibility of nuclear matter, it

is still inadequate to explain some of the basic properties of actinides as, for instance, the non-spherical ground state and the asymmetric mass division of fission fragments.

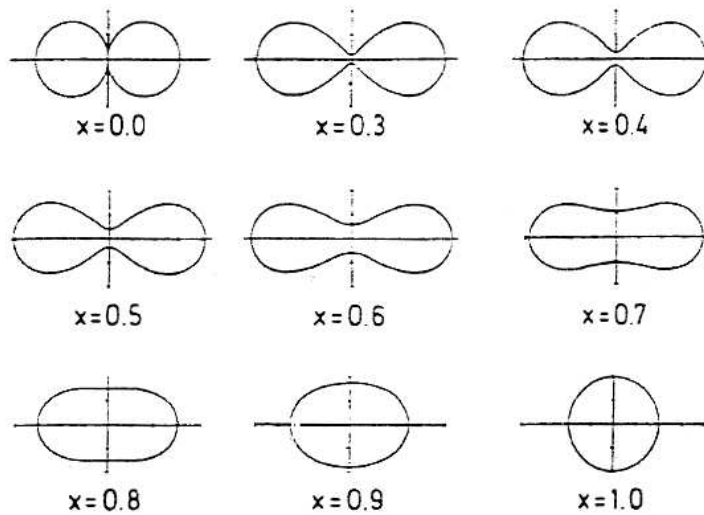


Figure 1.2: Nuclear shape as a function of deformation [5].

## 1.4. Macroscopic-Microscopic Models

As it has been discussed in the previous sections, the Single Particle Model treats the interaction between nucleons as an average, spherically-symmetric central potential, where the nucleons are assumed to move freely, what it is termed as a microscopic approach. Conversely, the Liquid Drop Model is taken as a macroscopic model.

Following Ref. [23], the first apparent weakness in this whole picture of the fission barrier lay in the quantitative estimates of barrier heights from the liquid drop theory. The liquid drop force constants deduced from analysis of nuclear masses can be adjusted to lead to barrier heights of the order of 5-6 MeV (above the ground state) for the actinides, but it is not possible to explain how the barriers can remain constant in the range from  $^{230}\text{Th}$  (with  $x=0.76$ ) to  $^{253}\text{Cf}$  ( $x=0.82$ ) as observed, while the liquid drop predictions change from 7.5 to 2.8 MeV in this range. It had long been known, however, that important deviations occurred for nuclei near shell closures, so that attempts were therefore made to incorporate the nucleon shell effects into the semiempirical formula given by Eq. (1.21).

In the mid-1960s, V. M. Strutinsky [50, 51] proposed a method where shell effects are theoretically taken into account as small deviations from a uniform single particle energy level distribution. This deviation is then treated as a correction to the liquid drop model energy which contains the dominant surface and Coulomb effects. The total energy in this macroscopic-microscopic model is the sum of the energy given by the liquid drop model and the shell and pairing corrections  $\delta U$  and  $\delta P$ , that take into account the quantum-mechanical structure of the nucleus:

$$E = E_{LDM} + \delta U + \delta P \quad (1.29)$$

Although these effects are larger in the vicinity of “magic” nuclei, microscopic corrections to the LDM occur to some extent in all nuclei.

#### 1.4.1. The fission barrier

The Strutinsky approach leads to the conclusion that the potential energy as a function of the nuclear deformation has two minima, as it is shown in Fig. 1.3, giving the so-called double-humped barrier. The “deformation” variable should be understood as a measure of progress along the energetically most favorable path to fission. The first minimum is containing the ground state and the first several excited levels, whereas the second one explains the existence of spontaneously fissioning shape isomers.

Following this model, when an actinide absorbs a nucleon and it is excited above its fission barrier, the most common result is immediate fission, but it cannot be discarded the possibility of radiative capture, that is, capture of the nucleon followed by  $\gamma$ -ray emission, leading the nucleus to a state in the first well. Another possibility is that the excited nucleus remains trapped in the second well in an excited isomeric state, which can either decay to the first minimum or fission spontaneously. The half-lives of the steady states in this well are much shorter than if the nucleus were in the ground state, since the fission barrier is much narrower.

Another feature of the double-humped fission barrier is the existence of a resonance structure in fission cross section. The levels in the first and in the second potential well will be designated class I and class II levels, respectively (see Fig. 1.3). For an excitation energy below the height of the barrier  $A$ , the two groups of levels (class I and class II) will be well separated. However, when the excitation energy is large enough, both groups of levels will be mixed. In an intermediate case, there will be a weak coupling between two types of levels through the barrier. Class I levels with energies near the more

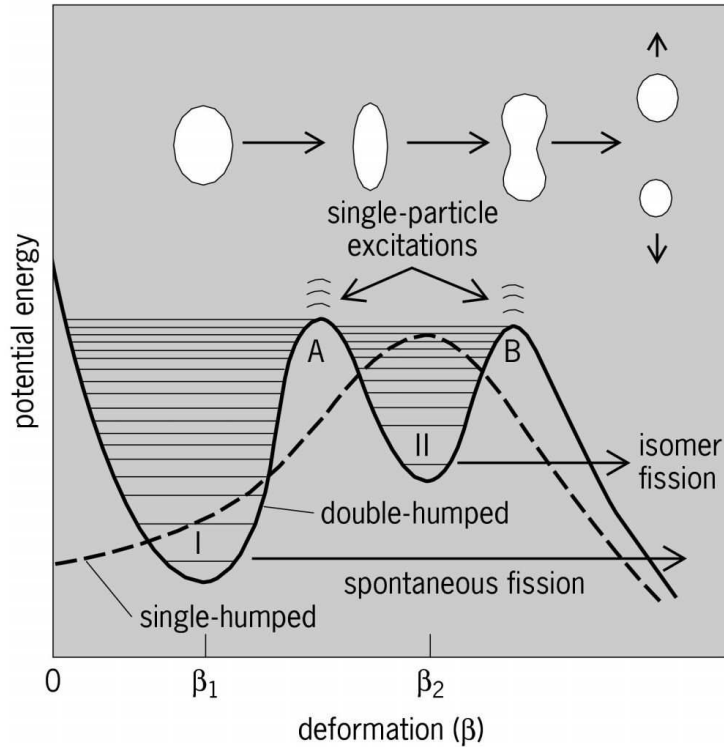


Figure 1.3: Potential energy as a function of deformation.

widely spaced class II levels will mix to form the actual compound levels. This effect is observed at fission threshold of actinides, for example, in  $^{237}\text{Np}$ . The fission cross section shows an structure with an average separation of about 50 eV between peaks, due to the spacing levels in the second well (class II states). If we go deeper in energy resolution, this so-called intermediate structure can be resolved into more closely spaced resonances, with a characteristic separation of the levels of the first well (class I states) of a few eV. This difference is because the second well is not as deep as the first one and, therefore, it has a smaller density of levels.

The double-humped barrier cannot describe the structure of several narrow resonances in the threshold region exhibited by some light actinides, as for example in neutron-induced fission of  $^{230}\text{Th}$  and  $^{232}\text{Th}$ . These resonances are too narrow to correspond to a deformation in the second well and their existence implies that the second well is much more above the first well than predicted by the theoretical estimations. P. Möller and J. R. Nix [52] suggested that this “thorium anomaly” could be best explained if the outer barrier peak were split into two peaks separated by a shallow third minimum,

being supported by the works of J. Blons et al. [53–55]. This triple-humped barrier allows the existence of class III vibrational states that could explain the structure found near to the first-chance fission cross-section of light isotopes of Th, Pa and U. An extended review on the theoretical aspects of their fission barriers, including a discussion on the suitability of the third well hypothesis, can be found in Ref. [23].

However, the triple-humped barrier hypothesis presents a somewhat confusing picture (see discussion in [56] and references therein). While the existence of a double-humped fission barrier is a common feature of both macroscopic-microscopic and self-consistent calculations, the existence of the third minimum (and its depth) depends on the calculation. For instance, in Ref. [57], it is claimed that resonances at the subthreshold fission of  $^{232}\text{Th}$  can be described by single-particle excitations in a phenomenological double-humped barrier. On the other hand, a model taking into account transmission through a triple-humped fission barrier with absorption was developed in [22]. The complex resonance structure in the first-chance neutron-induced fission cross sections of  $^{232}\text{Th}$  and  $^{231}\text{Pa}$  is well reproduced by the latter model, using 0.7 and 0.9 MeV shallow third wells, respectively.

In any case, accurate nuclear data on fission cross section and on the angular distribution of the fragments are crucial to understand the collective motion of nuclear matter leading to nuclear fission [28].

### 1.4.2. Multimodal fission

Recently, P. Möller et al. [58] performed more sophisticated calculations based on the method they introduced in Ref. [59]. In this way, fissioning nuclei can be described by a path on a multi-dimensional potential surface that determines the evolution from the ground state to the separated fission fragments. The total potential surface has, therefore, valleys in the space of elongation and mass number, and nuclei do not see a fission barrier (simple or double-humped) but a system of them, so that several different paths to fission can be available to the nucleus, what are called fission modes. An example of recent calculations for such potential surfaces is shown in Fig. 1.4, from Ref. [58].

Fission fragment data for some nuclei have been interpreted as showing the presence of at least two separate modes of fission, corresponding to different paths defined in the potential surface by “ridges” separating the “valleys” that are higher than the “mountain passes” (saddles). Such coexistence of two fission modes can involve, for example, two separated peaks in kinetic

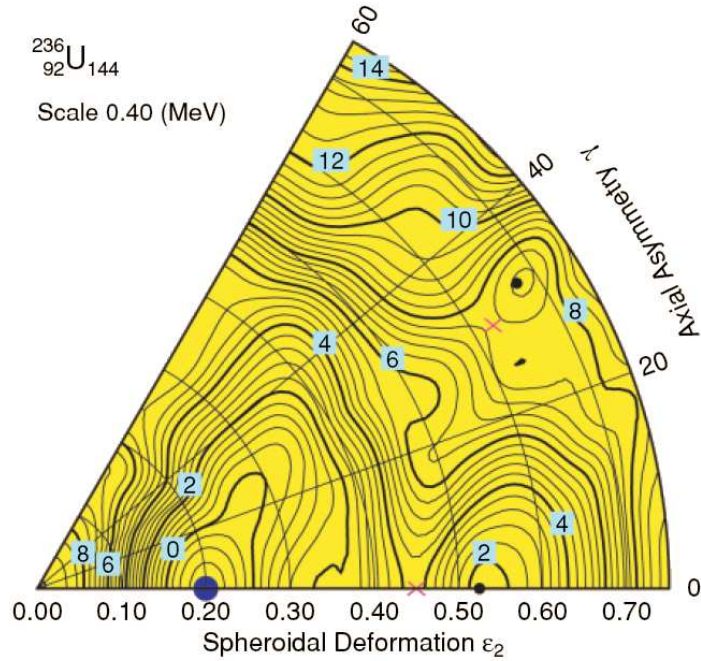


Figure 1.4: Contour plot of calculated potential energies for  $^{236}\text{U}$  as a function of spheroidal deformation and axial asymmetry [58]. The filled dots indicate local minima and the  $\times$  symbols represent saddle points. The large filled dot marks the ground state. Although this minimum is not the lowest minimum it has the highest fission barrier and it is therefore considered the ground-state minimum.

energy distributions, and separate thresholds for the onset of asymmetric and symmetric fission.

As reported in [58], the existence of two well-separated fission modes is a quite general feature for light actinides, as it can be seen in Fig. 1.5 for  $^{232}\text{Th}$ .

### 1.4.3. Shape dynamics of the fissioning nucleus

Following the basic LDM, the fissioning nuclei will evolve from their initial sphericity, with elongation as the main parameter (see Fig. 1.2.) Two nucleon clusters begin to develop giving rise to the nascent fragments separated by the so-called “neck”.

The basic assumption is that the fission fragment distributions can be determined at or near the scission point by using the relative potential energies of the complementary nascent fragments. These energies are functions

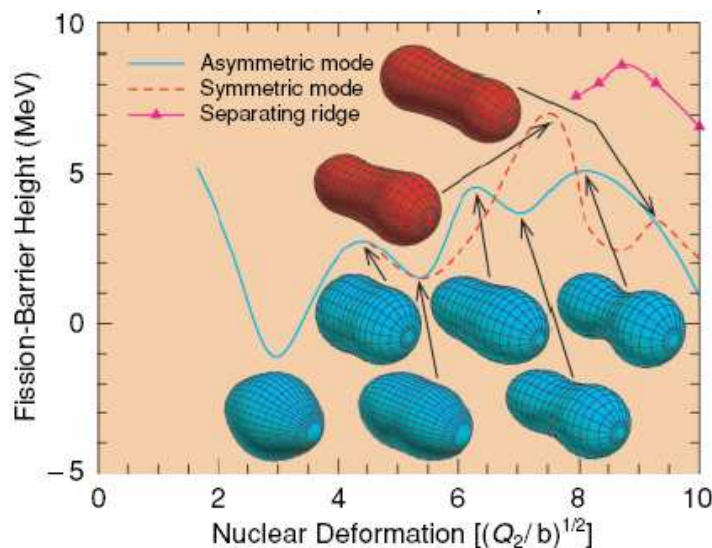


Figure 1.5: Triple-humped fission barriers for  $^{232}\text{Th}$  corresponding to different fission modes (symmetric and asymmetric) that are separated by a high ridge. Shapes associated with the barrier curves are displayed for representative points. Fig. from Ref. [58].

of their proton and neutron numbers and of their respective deformation parameters. The fragment pair is assumed to be nearly touching spheroids, and an additional term takes into account the surface energy associated with the neck connecting them (Fig. 1.6).

The neck rupture plays a key role to link the pre-scission shape to the exit channel. The neck rupture is produced when the nucleus is stretched beyond the pre-scission shape, but the rupture can be produced elsewhere in the neck being the number of pre-scission neutrons evaporated also random. This leads to different characteristics of the final fragments, in what is called the statistical scission model [60, 61]. The combination of the random neck rupture and the multiple-channel fission model allows to explain the asymmetric mass division in actinides in what is called the multi-modal random neck rupture, or Brosa model [61]. Further improvements to this model including temperature-dependent fission barriers have been developed [62].

## 1.5. Neutron-induced fission

A nucleus capable of undergoing fission after capturing a neutron is called “fissionable”. Currently, the term refers to those nuclei that can only fission

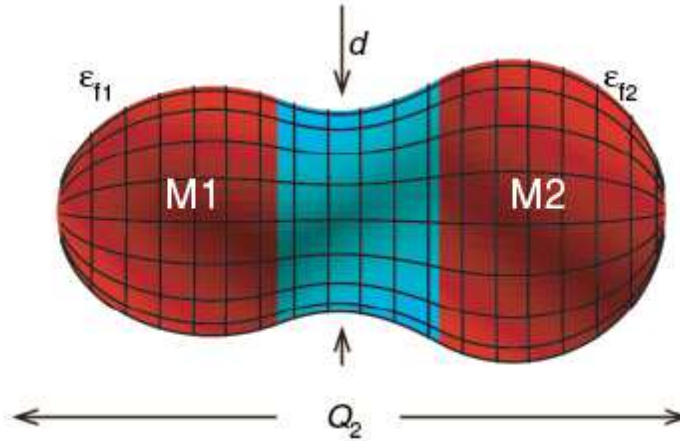


Figure 1.6: Shape parametrization of the fissioning nucleus showing a deformation given by its charge quadrupole momentum  $Q_2$ . Two nascent fragments of masses  $M_1$  and  $M_2$  and deformations  $\epsilon_{f1}$  and  $\epsilon_{f2}$ , respectively, are arising by developing a neck of diameter  $d$  in between. Fig. from Ref. [59].

after capture of a high-energy neutron, such as  $^{238}\text{U}$  or  $^{232}\text{Th}$ . However, a subset of the fissionable nuclei, known as “fissile” nuclei, can be induced to fission by low-energy neutrons, such as  $^{235}\text{U}$  or  $^{237}\text{Np}$ .

Two typical examples of the neutron-induced fission cross section are shown in Fig. 1.7 for  $^{235}\text{U}$  and  $^{238}\text{U}$ , as given by the ENDF/B-VII.1 evaluation [13]. For the fissile nucleus  $^{235}\text{U}$ , the fission cross section is large even for thermal energies, because the neutron binding energy is larger than the maximum of the fission barrier so that, after absorption of a neutron, the compound nucleus  $^{236}\text{U}$  is unstable against fission. As the neutron energy increases, the fission cross section decreases with  $1/v$ , being  $v$  the velocity of neutron. At somewhat higher energies, a large number of narrow resonances are shown due to class II states and, at a certain point, the resonances cannot be resolved anymore, because of the high density of levels.

In the  $^{238}\text{U}$  we find the opposite case, with a barrier higher than the neutron binding energy, so that only neutrons above a threshold energy can lead the nucleus to fission. This value is called “fission threshold” and cannot be seen in the case of  $^{235}\text{U}$  because of the tail of the  $1/v$  behaviour.

At higher energies, beyond the fission threshold, the behaviour of both fission cross sections is rather similar. The multiple-chance fission (i.e. fission preceded by neutron evaporation) becomes possible as the excitation energy of the compound nucleus exceeds the sum of the fission barrier plus the

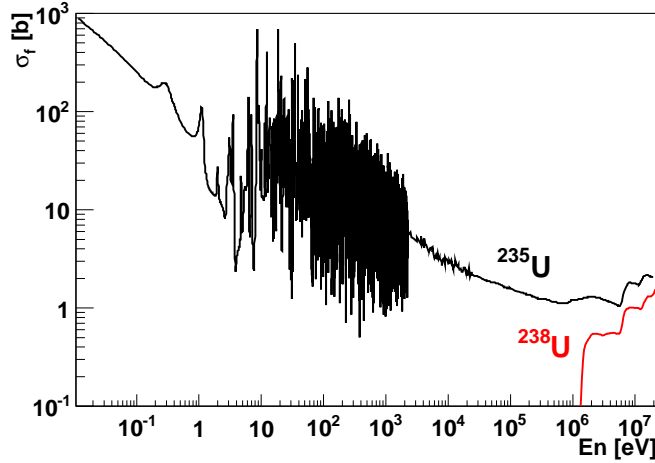


Figure 1.7: Neutron-induced fission cross section for  $^{235}\text{U}$  and  $^{238}\text{U}$  given by the ENDF/B-VII.1 evaluation [13].

neutron binding energy. So, the reaction (n,nf) is called “second-chance fission”; as the neutron energy increases, the thresholds of the “third-chance fission” (n,2nf) and “fourth-chance fission” (n,3nf) reactions are opened.

In general, the fission cross section above the threshold presents a step-like structure, due to the superposition of the different (n,xnf) reactions, as it is shown in Fig. 1.8 for  $^{232}\text{Th}$  [63]. As it will be shown later, there is a strong correlation between the opening of the thresholds of different fission chances and the angular distribution of the emitted fragments. As far as the fission fragment angular distribution is sensitive to the chance structure, the inclusion of angular anisotropy into the evaluation process imposes additional constraints into the parameters of the used model. According to I. V. Ryzhov et al. [64], at neutron energies beyond 15 MeV, fission is preceded by other pre-equilibrium processes including multiple-particle emission. This can involve a significant decrease in the total anisotropy of the emitted fission fragments. On the other hand, the multimodal behaviour (see Section 1.4.2) of the compound nucleus (the fissioning one) makes difficult any theoretical prediction, stressing the interest on reliable experimental data [65].

Let us, finally, mention that, above  $\sim 300$  MeV, the incident neutron has energy enough to undertake hadronic reactions with the nucleons of the target nucleus. The first of such a process is the creation of  $\Delta$  barions, giving rise to new de-excitation channels including  $\pi$  emission and subsequent charge interchange.

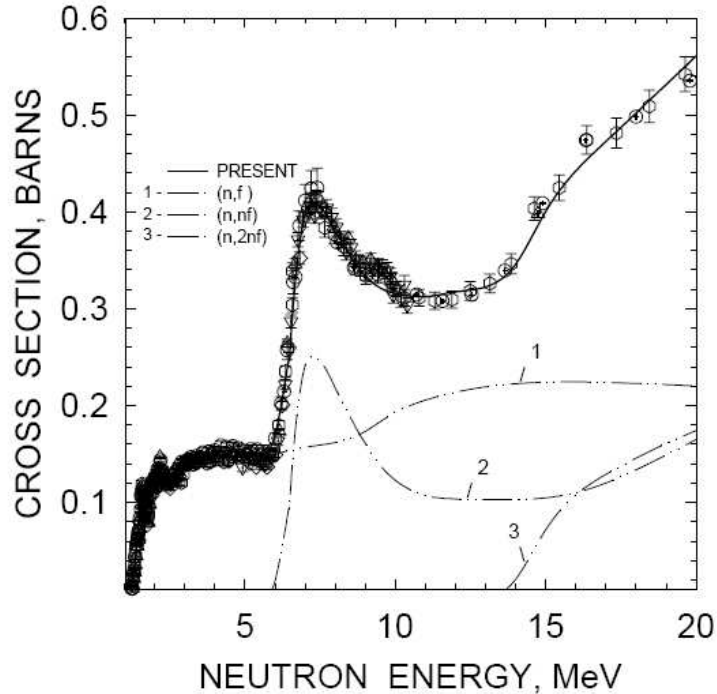


Figure 1.8: Chance fission contributions to the  $^{232}\text{Th}(n,f)$  cross section as given in Ref. [63].

### 1.5.1. Mass distribution of the fission fragments

As it was said in the introduction of this Chapter, nuclear fission is a process where a nucleus is split in two fragments of comparable mass. However, the mass of the fission fragments is not uniquely determined and a statistical mass distribution is observed for both fragments. Being  $A$  the mass of the fissioning nucleus, the fission is called *symmetric* when the fragment yield has a maximum in the mass  $A/2$ . In *asymmetric* fission, two peaks at different and almost complementary  $A$  values are attained.

This effect cannot be explained by the simple Liquid Drop Model, but the more sophisticated scission models presented in Section 1.4 do it: the mass yield depends on the pre-scission shape and on the random position where the neck has been broken. If the pre-scission shape is asymmetric, the thinnest part of the neck is not in the center and one light and one heavy fragment are produced, leading to a double-humped distribution for the mass yield. The width of the distribution allows to know the length of the neck since the longer the neck, the larger variety of fragments are produced.

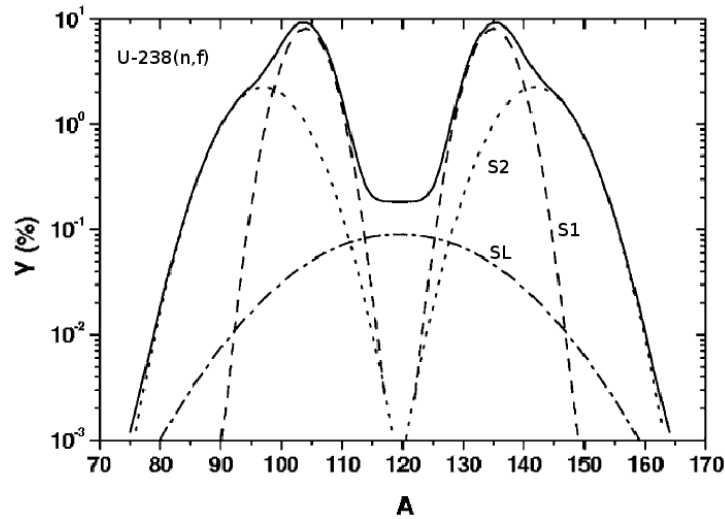


Figure 1.9: Contribution of the different fission modes to the mass distribution for  $^{238}\text{U}(n,f)$  [66].

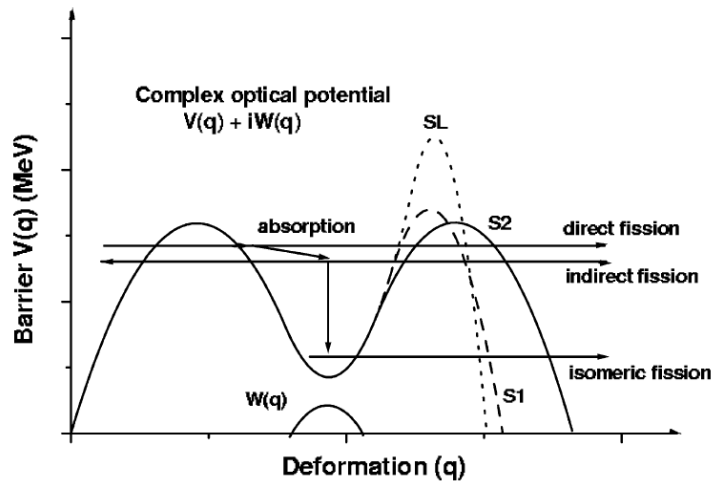


Figure 1.10: Double-humped fission barrier and the possible fission process [66].

The Brosa model [61] predicts three different modes: the superlong (SL), standard I (S1) and standard II (S2). The SL mode is related to the symmetric scission of the nucleus, and S1 and S2 correspond to asymmetric division, being the S2 more asymmetric than the S1, as it is shown in Fig. 1.9 for  $^{238}\text{U}(n,f)$  [66]. Fission of actinides is asymmetric, but as the excitation energy increases, the symmetric fission component becomes more important so that the ratio between asymmetric and symmetric yields decreases. This is

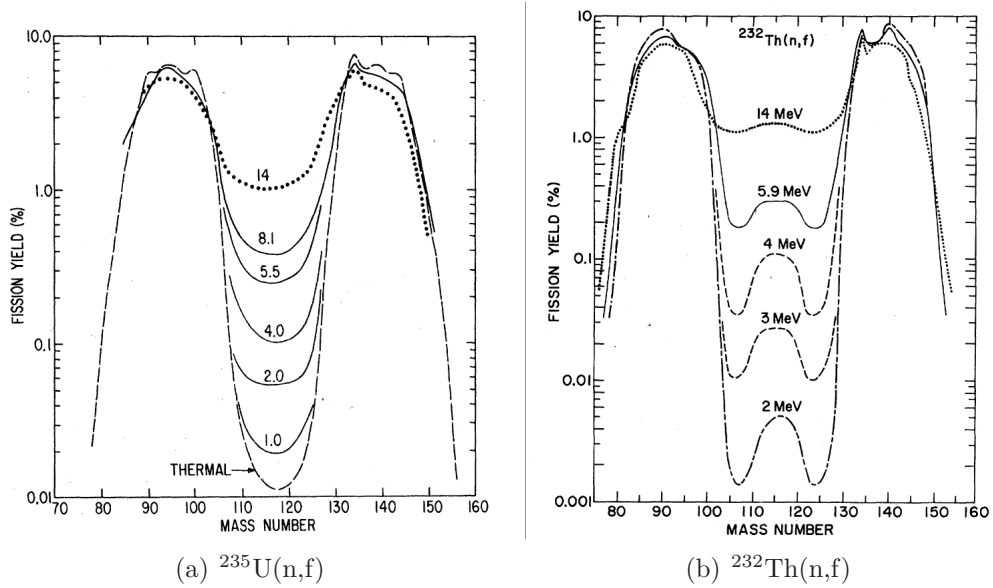


Figure 1.11: Fission fragment yield mass for the neutron induced fission of  $^{235}\text{U}$  [67] and  $^{232}\text{Th}$  [68]. A peak corresponding to symmetric fission is clearly seen in fission of  $^{232}\text{Th}$  for all neutron energies above 2 MeV, contrary to the  $^{235}\text{U}$  case, where the symmetric fission becomes important only above several tens of MeV.

explained by the presence of different outer barriers for each mode in the double-humped fission barrier, as it is illustrated in Fig. 1.10 [66] (the case of  $^{232}\text{Th}$  with a triple-humped barrier has been shown in Fig. 1.5). Fission of actinides is asymmetric, as it can be seen in Fig. 1.11. An unusual feature is found for Thorium, where a well defined third peak at mass symmetry appears for neutron-induced fission above 2 MeV [67, 68].

When studying different fissioning nuclei, another interesting effect is observed: the average mass of the heavy fission fragment remains nearly constant, while the mass of the light one increases linearly with the mass of the fissioning nucleus. This has been interpreted as a consequence of the shell structure, being the heavy fragment distribution centered near  $A=140$  (see, for instance, [34]).

### 1.5.2. Released energy in fission

Fission of actinides releases about 200 MeV, being the total kinetic energy of the fragments (TKE) the larger part of it, typically 170 MeV. The remaining energy is released by neutron and gamma emission, and  $\beta^-$  decay. The

high value of TKE can be understood by means of the high repulsive Coulomb force between the two fragments arising from the splitting of a charged liquid drop. Viola et al. [69], using experimental data from a broad range of fissioning nucleus, give a systematic on the total kinetic energy released as a function of the Coulomb parameter  $Z^2/A^{1/3}$ , obtaining the following relation:

$$TKE = (0.1189 \pm 0.0011) \cdot Z^2/A^{1/3} + 7.3 (\pm 1.5) \text{ MeV} \quad (1.30)$$

The kinetic energy  $E$  is related to the linear momentum  $p$  and to the mass  $m$  through the well known expression  $E = p^2/2m$ . Imposing momentum conservation:  $p_1 = p_2$ , we obtain the following result:

$$\frac{E_1}{E_2} = \frac{v_1}{v_2} = \frac{m_2}{m_1} \quad (1.31)$$

Because of the linear momentum conservation, the ratio between the kinetic energies of both fragments is equal to the inverse ratio of their masses so that, in asymmetric fission, the light fragment will carry more kinetic energy (and velocity) than the heavy fragment.

## 1.6. Fission fragment angular distribution

Non isotropic angular distribution of fission fragments was observed for the first time in 1952, when studying the photofission of  $^{232}\text{Th}$  (see Refs. [70, 71]) where fission fragments emitted preferentially at  $90^\circ$  with respect to the  $\gamma$  beam direction were found. Later experiments found similar results in neutron-induced fission reactions [72–74].

The standard theory is developed in Ref. [33] and is based on the model of axially symmetric transition states at the saddle point of the fissioning nucleus, that is supposed to be a symmetrical spinning top (i. e. a rigid body with two equal moments of inertia and different from the third one) as it can be seen in Fig. 1.12. The total angular momentum vector  $\vec{J}$  and its projection  $\vec{M}$  on the space-fixed axis  $z$  (that is usually taking in the beam direction) are constants of the motion and are conserved in the entire fission process, because of the conservation of the total angular momentum. The vector  $\vec{K}$  is the projection of  $\vec{J}$  on the symmetry axis of the top and  $\vec{R}$  is the projection of  $\vec{J}$  on any axis perpendicular to  $\vec{K}$ .

In the process to fission, the nucleus can suffer vibrations and changes in shape, redistributing its energy and angular momentum so that the  $K$  value of the transition nucleus is unrelated to the initial  $K$  values of the compound

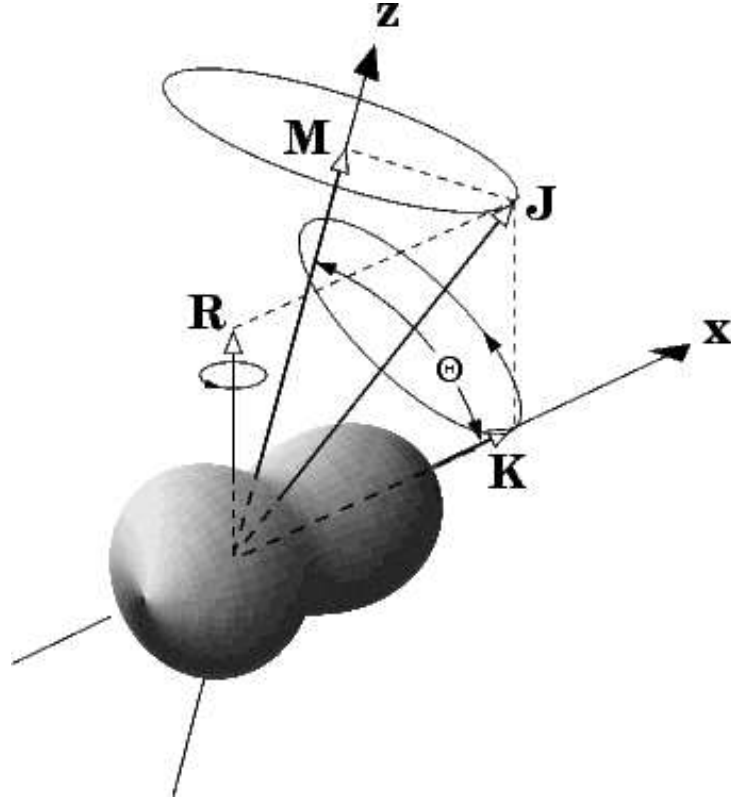


Figure 1.12: Fissioning nucleus.  $\vec{J}$  is the total angular momentum of the compound nucleus, and  $M$ ,  $K$  and  $R$  are, respectively, the projections on the space fixed axis  $z$ , on the symmetry axis of the compound nucleus, and on an axis perpendicular to  $\vec{K}$ .

nucleus. However, if we assume that  $K$  is a good quantum number in the passage of the nucleus from its transition state to the configuration of separated fragments, the directional dependence of fission fragments resulting from a transition state with quantum numbers  $J$ ,  $K$  and  $M$  is uniquely determined. In other words,  $K$  is a good quantum number after reaching the transition state deformation.

The wave equation for the symmetrical top with parallel  $J_{\parallel}$  and perpendicular  $J_{\perp}$  moments of inertia is given by:

$$\frac{\hbar^2}{2J_{\perp}} \left[ \frac{1}{\sin \theta} \frac{\partial}{\partial \theta} \left( \sin \theta \frac{\partial \psi}{\partial \theta} \right) + \frac{\left( \cos \theta \frac{\partial}{\partial X} - \frac{\partial}{\partial \phi} \right)^2 \psi}{\sin^2 \theta} \right] + \frac{\hbar^2}{2J_{\parallel}} \frac{\partial^2 \psi}{\partial X^2} + E\psi = 0 \quad (1.32)$$

The solution to this equation is:

$$\psi = \sqrt{\frac{2J+1}{8\pi^2}} e^{iM\phi} e^{iKX} d_{M,K}^J(\theta) \quad (1.33)$$

The  $d_{M,K}^J(\theta)$  functions are independent of the azimuthal angle around the space-fixed axis  $\phi$  and of the rotation angle of the top around its symmetry axis. They are given by:

$$d_{M,K}^J(\theta) = [(J+M)!(J-M)!(J+K)!(J-K)!]^2 \times \\ \times \sum_X (-1)^X \frac{[\sin(\theta/2)]^{K-M+2X} [\cos(\theta/2)]^{2J-K+M-2X}}{(J-K-X)!(J+M-X)!(X+K-M)!X!} \quad (1.34)$$

where the sum is over  $X=0, 1, 2, 3, \dots$  containing all terms in which no negative value appears in any of the quantities in parentheses in the denominator.

Although the wave function does not depend on the moments of inertia of the symmetric spinning top,  $J_{\parallel}$  and  $J_{\perp}$ , they determine its level spectrum, with energies of:

$$E = \frac{\hbar^2 [J(J+1) - K^2]}{2J_{\perp}} + \frac{\hbar^2 K^2}{2J_{\parallel}} \quad (1.35)$$

The probability of emitting fission fragments from a transition state with quantum numbers  $J$ ,  $M$  and  $K$  at an angle  $\theta$  is:

$$P_{M,K}^J(\theta) = \left[ \frac{(2J+1)}{4\pi R^2} \right] |d_{M,K}^J(\theta)|^2 2\pi R^2 \sin \theta d\theta \quad (1.36)$$

where  $\theta$  is the angle between the space-fixed axis and the symmetry axis of the fissioning nucleus.

The angular distribution for the fission fragments  $W_{M,K}^J(\theta)$  is obtained by dividing the probability for emitting fission fragments at an angle  $\theta$  (Eq. (1.36)) by  $\sin \theta$ :

$$W_{M,K}^J(\theta) = \left[ \frac{(2J+1)}{2} \right] |d_{M,K}^J(\theta)|^2 \quad (1.37)$$

### 1.6.1. Angular distribution in neutron-induced fission

Neutron-induced fission of even-even nuclei is useful to determine the level structure of the intermediate odd-mass transition nuclei. Neutron-induced

fission of  $^{232}\text{Th}$  [75] and of  $^{234}\text{U}$  [76] were used to provide the firsts explanations of the anisotropies observed in the fragments emitted in terms of particular  $K$  states of the transition nucleus.

For neutron-induced fission of an even-even target nucleus with zero spin,  $I=0$ . As the neutron spin is  $1/2$ ,  $M$  can only take two values,  $M = \pm 1/2$ , with equal probability. Therefore, after a few calculations, Eq. (1.37) gives the fission fragment angular distribution:

$$W_{\pm\frac{1}{2},\pm K}^J(\theta) = \left[ \frac{(2J+1)}{4} \right] \left[ |d_{\frac{1}{2},K}^J(\theta)|^2 + |d_{-\frac{1}{2},K}^J(\theta)|^2 \right] \quad (1.38)$$

The fission fragment angular distributions given by Eq. (1.38) are shown in Fig. 1.13. We see that, for  $K=1/2$ , the angular distribution is peaked to  $0^\circ$  with respect to the beam direction, while for  $K \neq 1/2$ , there are no fragments in that direction. In any case, we see that the anisotropy parameter defined as  $\sigma_f(0^\circ)/\sigma_f(90^\circ)$  is not enough to characterize the transition state and the full angular distribution is needed.

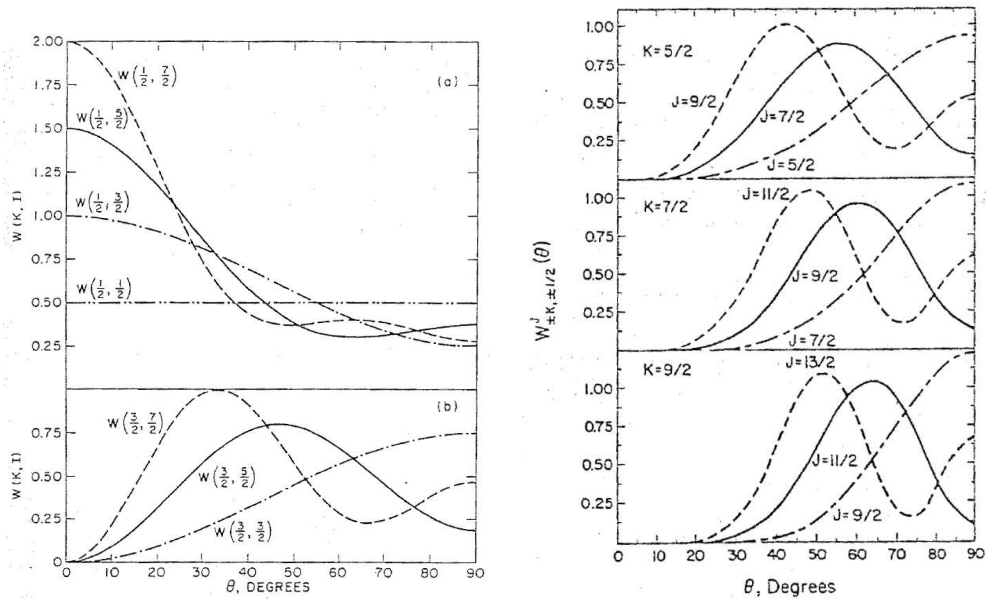


Figure 1.13: Theoretical fission fragment angular distributions for neutron induced fission of an even-even nucleus calculated with Eq. (1.38). Fig. from Ref. [33].

If the neutron energy exceeds several hundreds of keV, the compound nucleus can have several different  $J$  values, given by the orbital angular momentum  $l$  of the neutron, its spin  $s=1/2$ , and target spin  $I_0$ :  $J=|l \pm s|$ .

If the target nucleus is even-odd, the neutron capture produces an even-even fissioning nucleus. Due to the larger neutron binding energy, the excitation energy in the compound nucleus is much larger than the lowest fission barrier for the even-even transition nucleus and statistical methods are needed to describe the transition states.

The density of levels in a transition nucleus with spin  $J$  and projection  $K$  on the nuclear symmetry axis can be approximated by a Gaussian  $K$  distribution:

$$\rho(K) \propto \exp\left(-\frac{K^2}{2K_0^2}\right) \quad (K \leq J) \quad (1.39)$$

where  $K_0^2 = \mathfrak{J}_{eff}T/\hbar^2$ , being  $\mathfrak{J}_{eff}$  the effective moment of inertia and  $T$  the thermodynamic temperature of the fissioning nucleus.

The anisotropy depends on both  $J$  and  $K$  distributions. Angular distributions are more peaked along the beam direction as the beam energy or the projectile mass is increased. The anisotropy increases by increasing the weighting of high  $J$  states. On the other hand, the  $K$  distribution is characterized by  $K_0^2$ . This value increases with the excitation energy (directly related to the thermodynamic temperature) as given by Eq. (1.39). Therefore, the anisotropy decreases as the value  $K_0^2$  increases.

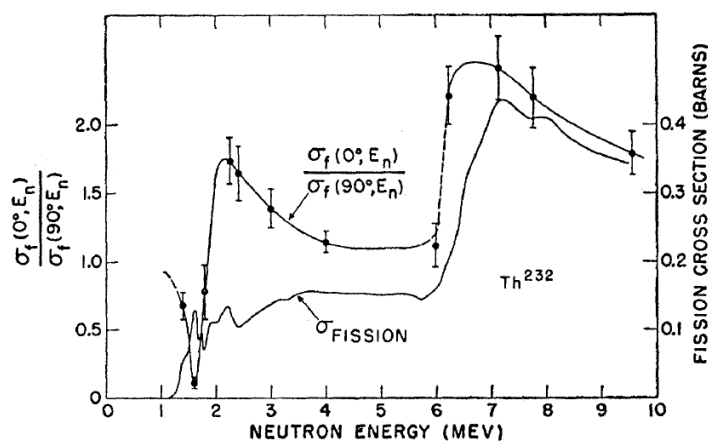


Figure 1.14: Comparison of fission cross section and anisotropy parameter for  $^{232}\text{Th}(n,f)$  from Ref. [74]. The multiple-chance structure is observed both in fission cross section and in the anisotropy parameter.

Anisotropy exhibits also a multiple chance structure similar to the exhibited by the fission cross section (Fig. 1.8). In addition to the low energy structure discussed at the beginning of this Section, a structure occurs at an excitation energy where second-chance ( $n,nf$ ), third-chance ( $n,2nf$ )... fission

becomes energetically possible (see Fig. 1.14). The anisotropy of the second-chance fission, around 6 or 7 MeV neutron energy, is specially large because of the small  $K_0^2$  value due to the low excitation energy near the fission barrier. This structure is more pronounced in even-even targets where the pairing energy gap plays an important role in the threshold energy region of second-chance fission.

# Chapter 2

## Experimental setup

### 2.1. Description of the n\_TOF facility

The neutron time-of flight (n\_TOF) facility at CERN [26, 77, 78] was primarily designed for the study of neutron-induced radiative capture and fission [6], which are of great relevance in nuclear astrophysics and in the development of new fuel cycles for both energy production and nuclear waste treatment [24, 25]. Neutrons are produced by the spallation reactions that occur when a 20 GeV/c proton beam from the CERN Proton Synchrotron (PS) accelerator impinges onto a lead target. The very high instantaneous flux of about  $2 \times 10^{15}$  neutrons/pulse makes it particularly well-suited for measuring the cross-sections of highly radioactive isotopic samples.

The spallation target is surrounded by a water moderator circuit that slows down the neutrons, resulting in a continuous energy spectrum from thermal energy to 1 GeV, with an excellent energy resolution of  $3 \times 10^{-4}$  up to a few keV. This resolution is obtained thanks to the long, 185 m flight path that makes it possible to obtain more accurate and complete information about fission cross sections, well above the capacities of any other neutron facility.

#### 2.1.1. The Proton Synchrotron beam

The Proton Synchrotron (PS) beam is driven to the spallation target via the FTN transfer line (installed in the TT2-A tunnel). The proton beam dedicated to the n\_TOF facility has a momentum of 20 GeV/c, the maximum energy that can be achieved with a PS cycle of 1.2 s. Each proton bunch has

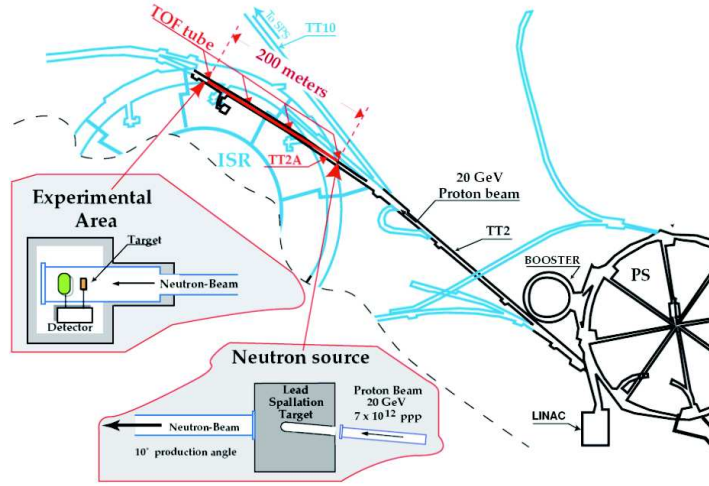


Figure 2.1: Schematic map of the  $n$ -TOF facility at CERN.

a width of 7 ns r.m.s. and contains around  $7 \times 10^{12}$  protons. It is possible to deliver up to 6 bunches in a PS supercycle, which is typically 14.4 s. However, due to the maximum power dissipation allowed in the spallation target, a maximum of five bunches per supercycle are delivered to the  $n$ -TOF target. This low repetition rate (0.4 Hz) prevents the overlapping of the low energy neutrons produced in one bunch with the high energy neutrons at the start of the next one.

During the spallation process, large amounts of secondary particles are produced, such as protons, muons, pions, and  $\gamma$  rays. Since most of them are emitted in the direction of the proton beam, the beam line has been designed to enter the target at an angle of  $10^\circ$  with respect to the TOF tube axis.

The  $n$ -TOF facility can receive proton beams from the PS in either a dedicated or parasitic extraction mode. If nominal intensity is reached in the dedicated mode, bunches of about  $4 \times 10^{12}$  protons are delivered in the parasitic mode, in which the  $n$ -TOF bunch is accelerated with a lower intensity one that is driven to the East Hall experimental areas. The bunch length is 7 ns r.m.s. in both dedicated and parasitic modes. The current status of the PS beam and the supercycle configuration is available via internet through PS-Vistars [79], as illustrated in Fig. 2.2.

Information on the proton beam is provided by several devices installed near the end of the FTN line: The Beam Current Transformer (BCT) monitor the proton intensity sent to the target, pulse by pulse. The Wall Current Monitor (WCM) provides a pulse (pick-up signal) that is related to the in-

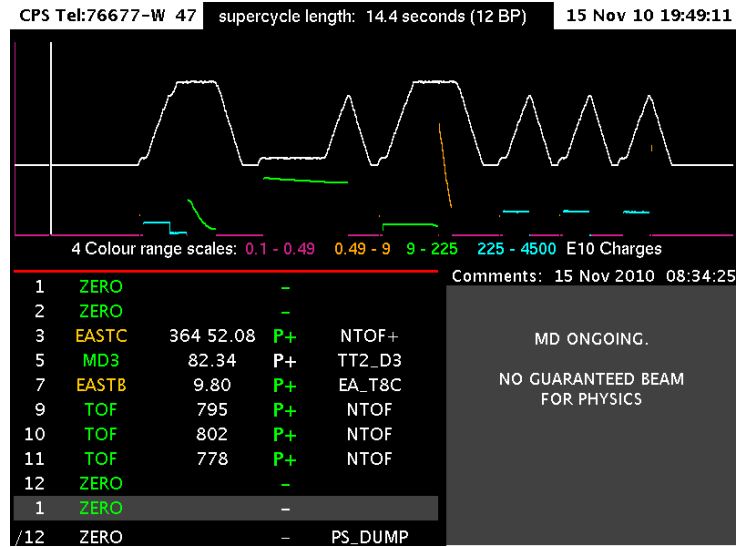


Figure 2.2: A view of PS-Vistars showing the current status of the proton beam [79]. The supercycle configuration and the intensity of each pulse are indicated. In this view, three dedicated and one parasitic pulse per supercycle are delivered to n\_TOF.

stantaneous proton beam intensity and can be also used for timing purposes. The BCT proton intensity and the pick-up signal are included in the Data Acquisition System (DAQ) for further use in data analysis. The BCT also provides the trigger signal for the n\_TOF DAQ. False trigger signals are sometimes provided without protons in the target, so that the pick-up signal must be used to confirm the presence of the beam.

### 2.1.2. The spallation target

The spallation target consists of a cylindrical lead block 60 cm in diameter and 40 cm in length, surrounded and cooled by a forced flow of water 1 cm thick. The water also acts as an energy moderator for the neutrons produced in the spallation target [80]. Although this 1 cm layer of water is well-suited to maintain the target surface temperature below the water boiling point and the inner temperature of the target below the lead melting point, is not thick enough for optimal redistribution of the neutron energies. For this purpose, an additional 4 cm-thick moderator volume was installed that can be filled with either water or borated water. The latter one absorbs most thermal neutrons in  $^{10}\text{B}(n, \alpha)$  reactions and thus minimizes the  $\gamma$  rays produced in the neutron capture of  $^1\text{H}$ .

The current n\_TOF spallation target was installed in 2008 to replace the original target [78]. Surface oxidation, especially in the proton impact area, had forced a shutdown of the facility in 2004. Both the mechanical design and the cooling system of the new target (shown in Fig. 2.3) give it much better performance. After its installation, it was commissioned [80] before restarting the physics programme at n\_TOF.

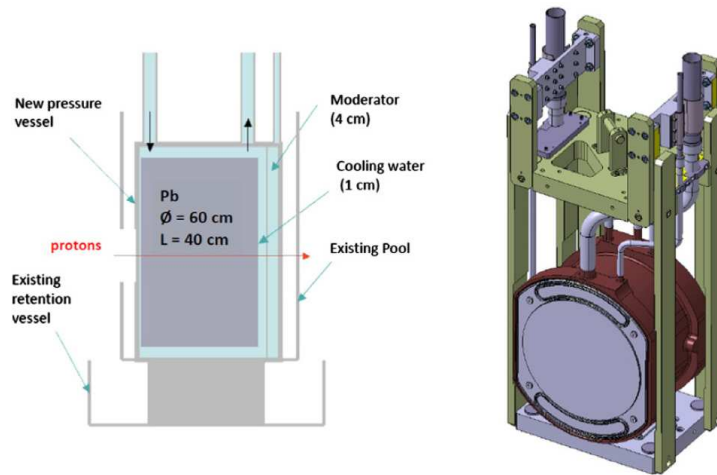


Figure 2.3: Design of the spallation target.

### 2.1.3. The TOF tube

The neutrons emitted from the spallation target travel in a vacuum tube (the TOF tube) towards the experimental area situated 185 m downstream from the target, and continue until they reach the beam dump in the Neutron Escape Lane located farther downstream at 200 m from the target. The vacuum tube is placed at an angle of  $10^\circ$  with respect to the proton beam, to reduce the high-energy charged particles and  $\gamma$  rays emitted mostly in the forward direction. A schematic view of the TOF tube can be seen in Fig. 2.4.

The TOF tube is made of stainless steel and divided into several sections of progressively reduced diameter, with an inner pressure of about 1 mbar. In the first section (starting from the spallation target), the tube has a diameter of 800 mm; after 70 m, the tube is reduced to 600 mm in diameter and passes through iron shielding 2 m thick that is embedded in 40 cm of concrete. After 140 m, the beam tube is reduced again to 400 mm in diameter just before the first collimator, which has an inner diameter of 110 mm. The collimator

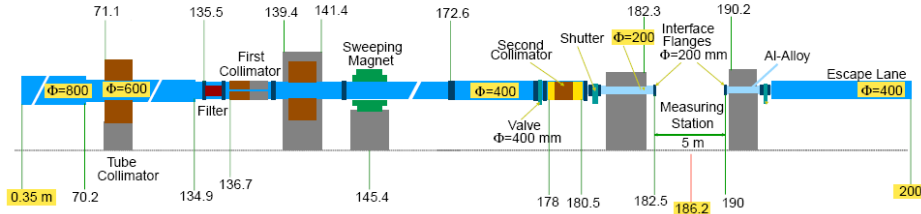


Figure 2.4: Schematic view of the TOF tube sections and components. Distances are measured from the center of the spallation target. The drawing is not to scale.

reduces the divergence of the beam at the Experimental Area.

A sweeping dipolar magnet 2 m long and with a magnetic rigidity of  $\sim 1$  T·m is located at  $\sim 145$  m from the target (see picture in Fig. 2.5(a)). Charged particles with a momentum of up to 10 GeV/c are deflected out of the neutron beam by the magnet before they can reach the Experimental Area. The  $\mu$  component of the background is eliminated by iron shielding that covers the entire tunnel cross section and a layer of concrete 3.2 m thick.

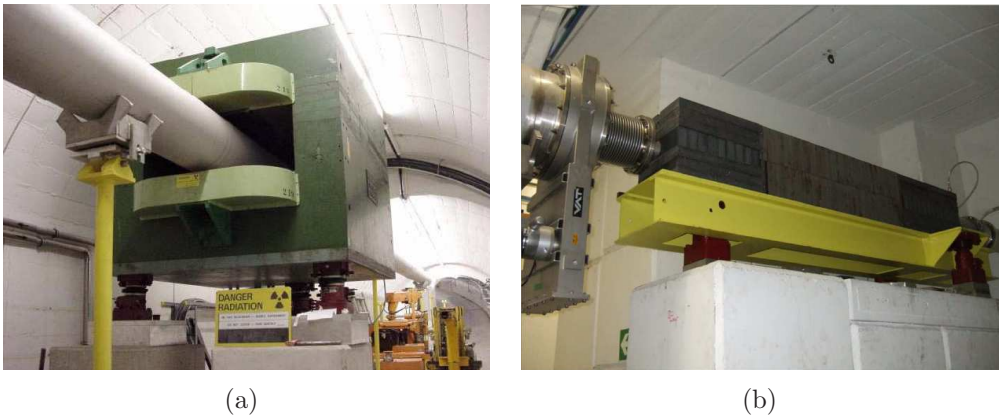


Figure 2.5: The sweeping magnet (a) and the second collimator defining the beam size (b).

After another reduction of the TOF tube from 400 mm to 200 mm in diameter, a second collimator is placed at  $\sim 178$  m, just before the Experimental Area, to define the size of the neutron beam at the Experimental Area (see picture in Fig. 2.5(b)). Two sizes are possible depending on the experiment: for capture measurements, targets are thick and small, so a small beam with an inner diameter of 1.9 cm is used. However, the inner diameter of the beam is 8 cm for fission measurements, which use larger and thinner target samples.

The detectors are placed in the low-background Experimental Area, a Class-A laboratory situated between two concrete walls located at 182.5 m and 190 m from the target. After leaving the Experimental Area, the neutron beam continues through the “Escape Lane”, which consists of 8 m of vacuum tube 200 mm in diameter. The tube ends in a polyethylene dumping block with cadmium foils, which reduces the neutron backscattering to the Experimental Area. Inside the block, three  $\text{BF}_3$  gas counters can be used to monitor the neutron beam pulse by pulse [81].

The front-end electronics and the data acquisition system are located in the Escape Lane area, where is also the access control to the class-A Experimental Area.

#### 2.1.4. Neutron beam characteristics

To characterize the neutron beam of an experimental facility such as n\_TOF, the neutron energy spectrum with its energy resolution must be accurately known. For this purpose, commissionings were performed at the beginning of the phase I experiments, with the old target [82, 83], and for the phase II, after the substitution of the old target by the new one [80]. The main characteristics of the neutron beam that relate to the experiment described in this thesis, were measured with the new spallation target using normal water as the moderator and are described in the following paragraphs.

#### Neutron flux

The n\_TOF neutron beam covers a very broad energy range, from thermal neutrons up to 1 GeV. The measured neutron spectrum can be seen in Fig. 2.6, expressed as neutron flux divided by  $\ln(E)$  and by the nominal beam intensity ( $\text{dn}/\text{d}(\ln E)/\text{cm}^2/7 \times 10^{12}$  protons). Isolethargic units are useful for describing neutron flux over an energy range covering several orders of magnitude, since they give the number of neutrons in a logarithmic energy interval. Fig. 2.6(a) and Fig. 2.6(b) show results from dedicated experiments and from simulations, respectively [84]. The integrated neutron fluence up to 1 MeV is  $\sim 10^5$  neutrons/ $\text{cm}^2/7 \times 10^{12}$  protons at the Experimental Area when using the capture collimator.

The shape of the neutron flux is dominated by a nearly isolethargic distribution between 1 eV and several hundred keV, and a thermal peak that disappears when borated water is used as the moderator instead of normal water (Fig. 2.6(b)). Transmission dips appear in the keV region, result-

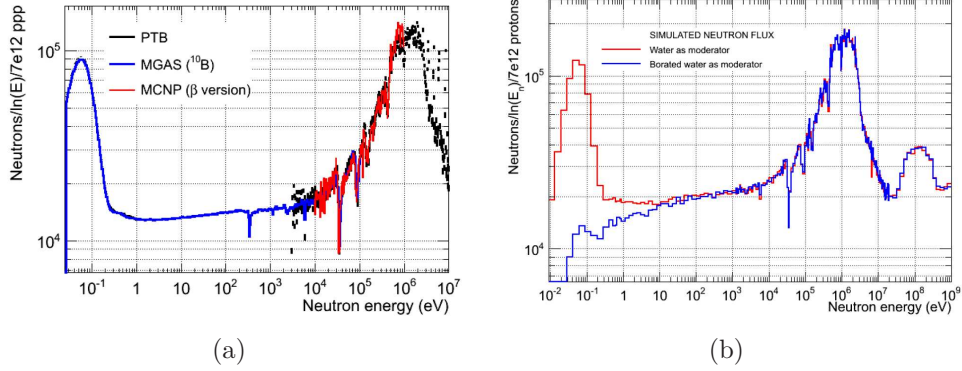


Figure 2.6: Neutron flux in the Experimental Area of n\_TOF: (a) Different results from dedicated measurements; (b) Simulation results showing the different effects of moderation with water or borated water in the low energy part of the spectrum.

ing from the aluminium windows along the beam line. Neutrons with energy below 0.02 eV do not reach the experimental area due to gravitational effects.

## Beam profile

The beam profile using the old target at the Experimental Area had been studied with a MicroMegas detector [85] and a solid state track detector (CR-39) [86]. For the commissioning of the new spallation target, a new X-Y MicroMegas detector [87] was used to obtain the spatial distribution of neutrons (Fig. 2.7). It is based on bulk technology and consists of a  $6 \times 6$  cm<sup>2</sup> active area divided into  $106 \times 106$  strips. A <sup>10</sup>B converter was used to produce the reaction  $^{10}\text{B} + n \rightarrow ^7\text{Li} + \alpha$ , where the detection of both final fragments gave the spatial position of the neutron interaction.

## Neutron energy resolution

In a neutron time-of-flight facility, the energy resolution depends on the uncertainty in the determination of the flight path and on the time resolution of the proton beam that hits the spallation target, as well as on the resolution of the detection system of the neutron reaction. However, we can neglect the latter one compared to the contribution of the neutron beam production related effects. Therefore, the main contribution to the uncertainty in the distance  $\delta L$  is due to the determination of the total flight-path, including the moderation distance that can be only obtained by simulations. The time uncertainty  $\delta T$  is due to the 7 ns width of the proton pulse, much greater

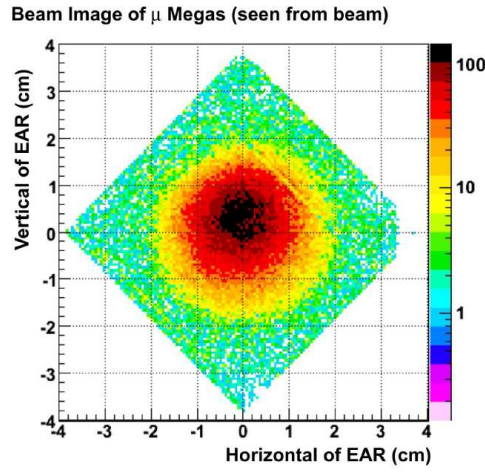


Figure 2.7: Neutron beam profile at the Experimental Area measured with X-Y MicroMegs Detector for neutron energies below 1 MeV, using the capture collimator. (Fig. from Ref. [87].)

than the response of the anode signal of the PPAC detectors used in the present work, that is less than 1 ns.

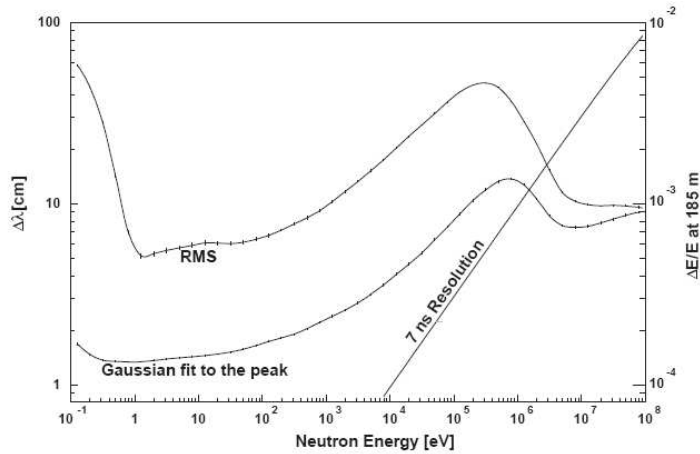


Figure 2.8: Monte Carlo simulation of the energy resolution at 185 m from the old target. The 7 ns resolution due to the proton beam dominates the resolution above a few MeV neutron energy (From Ref. [83]).

The resolution function  $\Delta E/E$  of a neutron beam is defined as the time spread of neutrons with energy  $E_n$  going out from the target-moderator assembly and it is usually expressed as a function of the flight path. Results from Monte Carlo simulations on the energy resolution at the n\_TOF ex-

perimental area are shown in Fig. 2.8 for the old target [83]. The quantity  $\Delta\lambda$  is the moderation distance, that is, the effective distance travelled by the neutrons during the moderation process inside the spallation target and the moderator. The 7 ns resolution curve represents the effect due to the proton pulse width, that dominates above several MeV. At low energies, the resolution function is dominated by the moderation distance determination.

### 2.1.5. The n\_TOF Data Acquisition System

One of the important features of the n\_TOF facility is its Data Acquisition System (DAQ), based on high-performance flash-ADCs [26, 77]. This DAQ was specifically developed to take advantage of low neutron repetition rates of about 0.4 Hz, which correspond to the maximum expected number of event rates due to target limitations. What makes this DAQ unique is its ability to store the full analog waveform of the detector signals for each neutron pulse using on-line zero-suppression, which makes it possible to reproduce the full response of the detector in a later off-line analysis. In this way, pile-up effects, baseline shifts or background events can be solved.

The n\_TOF DAQ currently consists of about 60 Flash-ADC (FADC) channels with 8-bit resolution, sampling rates up to 2 GHz and 8 or 16 MB of internal buffer memory. Each detector signal in the experimental setup is registered by a FADC channel. The FADC modules are Acquis Digitizers with two or four data inputs plus one external trigger input, which are installed in a cPCI crate housing up to 4 modules.

The pulsed structure of the PS beam causes the DAQ to be triggered by the impact of the proton beam on the spallation target, opening a 16 ms time window. This is the time needed to completely fill the 8 MB buffer memory at a sampling rate of 500 MHz (which corresponds to a 2 ns time binning), the typical working value for most n\_TOF detectors, including PPACs. The lowest neutron energy available is therefore 0.7 eV, which corresponds to the 16 ms time of flight. The data stored in the 8 MB memory of a FADC channel contains the full detector information for a neutron pulse.

To reduce the large amount of data generated, a fast zero-suppression algorithm is used to select only the data frames containing true detector signals above a set threshold on the FADC. A certain number of pre-samples at the beginning and post-samples at the end of the frames facilitates the pulse shape analysis. The speed of this operation is limited by the transfer rate of the existing DAQ PCs (typically 80-100 MB/s per PC). To ensure complete data transfer during the 1.2 s time minimum between two proton

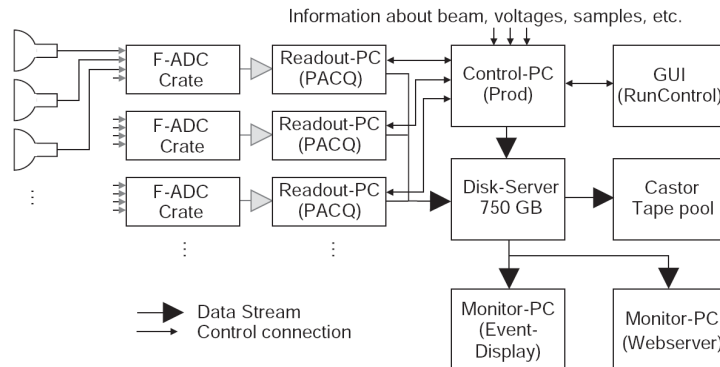


Figure 2.9: Schematic view of the  $n$ \_TOF data acquisition system. The output produced by the detectors (left) is digitized by flash-ADCs over a period of 16 ms. The data are transferred via cPCI/PCI adaptors into the readout PCs and the disk server before being transferred to the CASTOR storage system at CERN. A few monitor PCs can access the data temporarily stored on the disk-server, allowing a near-on-line monitoring of events. (From Ref. [88]).

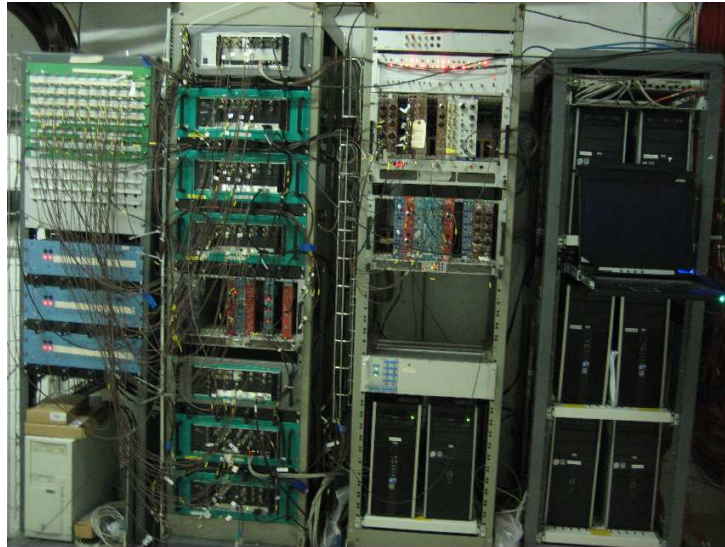


Figure 2.10: View of the  $n$ \_TOF DAQ, situated in the Escape Lane. In the picture, from the left to the right: the patch panel with connectors of the detector signals; the cPCI crates with FADC modules; trigger electronics; and readout PCs.

bunches, the number of FADC channels connected to each readout PC is limited to 8, in what is called a *stream*. Special care has been taken in the distribution of the modules to avoid overloading any of the crates. The information of one event is distributed among several data streams (7 streams

and 50 FADC channels are used in the PPACs), which reduces the readout time, preserves modularity and allows for expansion of the system. Event reconstruction and the physics analysis are done in a later stage, after the raw data have been stored on tape and disk. However, several monitor PCs have access to these data while they are temporarily stored on the disk-server. This makes it possible to read the raw data and the digitized signals almost immediately, facilitating a near on-line monitoring.

When raw data files exceed 2 GB, they are closed and transferred via GigaBit ethernet to the CASTOR (CERN Advanced STORage manager) storage system [89]. This size limitation was introduced to minimize data losses in case of file corruption. After migration to tape, each raw data file is mirrored to a disk pool for pulse shape analysis of the different FADC data sets corresponding to the detectors. Each detector has a different algorithm with specific features. During this analysis, the relevant parameters of each signal (time or amplitude, for example, depending on the detector) are extracted from the pulse shapes, saved on a Data Summary Tape (DST) and stored on both tape and disk. This continuous process creates a DST file a few hours after the raw data file was migrated to tape. The entire process is illustrated in Fig 2.9, and a photograph of the real system can be seen in Fig. 2.10.

The n\_TOF DAQ functions and features are described in detail in Ref. [88].

## 2.2. The experimental fission detection setup

Fission measurements at n\_TOF are carried out with several different detectors: the Fast Ionization Chamber (FIC) [90], which has been used to measure the fission cross sections of  $^{233}\text{U}$ ,  $^{241}\text{Am}$ ,  $^{243}\text{Am}$  and  $^{245}\text{Cm}$  [91, 92]; the MicroMegs, which has been used to measure the fission cross section of  $^{240}\text{Pu}$  and  $^{242}\text{Pu}$  [93] and Parallel Plate Avalanche Counters (PPACs), that are the detector that has been used to measure the fission cross sections of different actinides ( $^{233}\text{U}$ ,  $^{234}\text{U}$  and  $^{237}\text{Np}$  [3]) and subactinides ( $^{nat}\text{Pb}$  and  $^{209}\text{Bi}$  [4]). In the present work, we used a different PPAC configuration with tilted planes, making so possible to extend the angular range of the detected fission fragments, by which we could measure the angular distribution of the fragments emitted in the fission of the different samples included in the setup.

### 2.2.1. Parallel Plate Avalanche Counters

The Parallel Plate Avalanche Counter (PPAC) is a type of gas detector that operates in a proportional mode. Most proportional gas counters use anodes made of thin wires that create a high electric field very close around them, being just where the avalanche grows. In contrast with the cylindrical geometries of the wire counters, the PPAC electrodes are plates in a parallel configuration, with small distances separating them. The gas pressure varies from 1 to 20 mbar and a reduced field of approximately 300 V/cm·mbar is enough to reach the proportional regime. The low-pressure gas is so contained in a uniform electric field and the avalanche region occupies the entire counter volume in between the electrodes.

The basic operating principle of gas detectors is explained in most books on radiation detection (see, for instance, Refs. [94–96]): a charged particle entering between the plates produces a track of primary ion pairs, and the electrons and positive ions drift to the anode and the cathode, respectively. During this drift, electrons can collide with neutral gas molecules, generating more ion pairs. The electrons liberated by this secondary ionization process are also accelerated by the electric field and can collide again with other neutral gas molecules, creating a *swarm* of electrons that drift to the anode. Under certain reduced electric field conditions, which will differ according to the gas mixture, this multiplication process stops when all the electrons have been collected in the anode, in what is known as the Townsend avalanche [94]. The increase of the number  $n$  of electrons per unit path length,  $x$ , is given as:

$$\frac{dn}{n} = \alpha \cdot dx \quad (2.1)$$

where  $\alpha$  is named as the first Townsend coefficient. When the electric field is constant and uniform, as is the case in parallel plate geometry, the coefficient  $\alpha$  is a constant, and the solution to Eq. (2.1) is given by:

$$n(x) = n(0) \cdot e^{\alpha x} \quad (2.2)$$

Both ions and electron swarms will increase until the space-charge effect causes the local field to drop.

Positive ions drift towards the cathode at a velocity of around 1% of the velocity of the free electrons. The output shape signal consists of a fast-rising component generated by the electron collection (typically of the order of nanoseconds), and a much slower component produced by the motion of the positive ions. Only the fast component is used for timing purposes, being

the slow component eliminated by the shorter time constant of the collection circuit.

Pure hydrocarbons were commonly used in PPACs, with isobutane ( $C_4H_{10}$ ) providing the highest gain and reaching up to 100% detection efficiency in an ample range of deposited energy. The energy resolution is only around 20% because of straggling in the gas. Octafluoropropane ( $C_3F_8$ ) is now most frequently used because, unlike hydrocarbons, which can be explosive under certain conditions, it offers the same advantages as isobutane but being not at all flammable. The gas is continuously renewed during detector operation, to evacuate the molecular radicals and gas and water desorption produced during the ionization process.

PPACs are designed in such a way that the Townsend avalanche is self-extinguished due to their short multiplication path. Therefore, PPACs are less sensitive to minimum ionizing particles (mips) and must be triggered by the very high ionization produced by the fission fragments.

PPACs are distinguished from RPCs (Resistive Plate Counters) because the electrodes are made of a metallic layer (backed usually by a Mylar foil), whereas in the RPCs the plate electrodes are conversely made of a resistive material (usually a glass sheet). Apart of this, their functioning principle is the same, basically.

It is worth to mention here that, when used to track intermediate energy heavy ions (as fission fragments are), PPACs take advantage of the fact that such ions will sputter out many electrons from the electrode foils, when they are passing through. It is, indeed, well known (see, for instance, [97] and references therein) that fission fragments at near 1 MeV/A will create 100 to 200 primary electrons sputtered out from an aluminized Mylar foil. These primary electrons will be the seeds of the growing avalanche, giving as a result a close-to-one detection efficiency for fission fragment detection.

From their beginning, PPACs [98, 99] offered great improvements over other types of detectors with regard to their time resolution, which is typically less than 1 ns, though values below 200 ps have been reported even with light particles [100]. Since PPACs are insensitive to long-range particles, they are widely used to detect fission fragments [101–103], even in a background with high levels of  $\gamma$  rays or light charged particles. Unlike scintillator or semiconductor detectors, they are not damaged by radiation and high counting rates; this makes them useful for in-beam applications of neutron and proton-induced reactions [104, 105]. PPACs have been also used as neutron detectors where a  $^{10}B$  or  $^6Li$  electrode serves as a converter [106].

The detector design used for fission at n\_TOF consists of a double PPAC

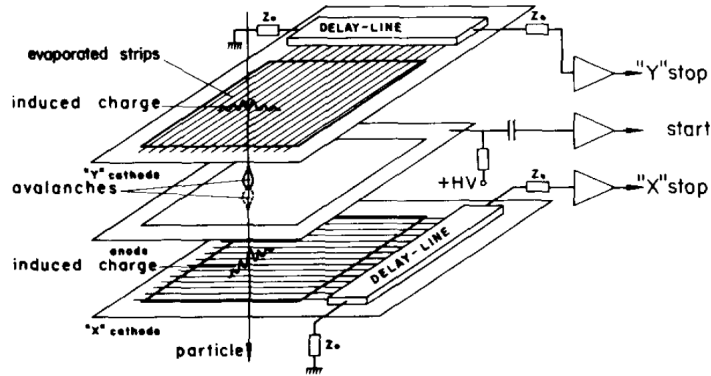


Figure 2.11: Schematic view of a position-sensitive PPAC with a common anode and two stripped cathodes [107].

with a common anode and two stripped cathodes in orthogonal directions, as illustrated in Fig. 2.11. With this design, it is possible to obtain the spatial position of the impinging fission fragment [107]. The avalanche produced induces a positive pulse in the cathode strips closer to the avalanche position. Each strip acquires part of the induced charge and the centroid of the charge distribution provides accurate information about the position of the avalanche. Among the several methods developed to measure the centroid of the induced charge, the delay-line read-out method shows characteristics that are useful for us. Each of the strips is connected to a delay line and a preamplifier is connected to each end. The position of the avalanche is obtained by measuring the delay time between the pulse on the anode and the pulses propagating along the delay lines. An advantage of this method is that only two signals are obtained per cathode, instead of one per strip, which reduces the number of readout channels.

In addition to the advantages listed above, PPAC detectors are relatively easy and inexpensive to build with large sensitive areas [108]. This makes them the most convenient and appropriate detectors for our work at the n\_TOF facility, where they are exposed to the high-intensity neutron flux that has a  $\gamma$  background characteristic of spallation neutron sources.

### 2.2.2. The n\_TOF detection setup

Several PPACs with a  $20 \times 20$  cm<sup>2</sup> surface area were developed and built at the IPN d'Orsay Laboratory (France) [109, 110], for use at the n\_TOF facility. The anode is a  $1.5 \mu\text{m}$  layer of Mylar foil aluminized on both sides and glued

onto a frame. The frame is made of an epoxy resin, coated with a thin, metalized copper layer to shield the detector against electromagnetic noise. The copper is gold-plated to prevent its oxidation, giving it the characteristic golden colour that can be seen in Fig. 2.12.

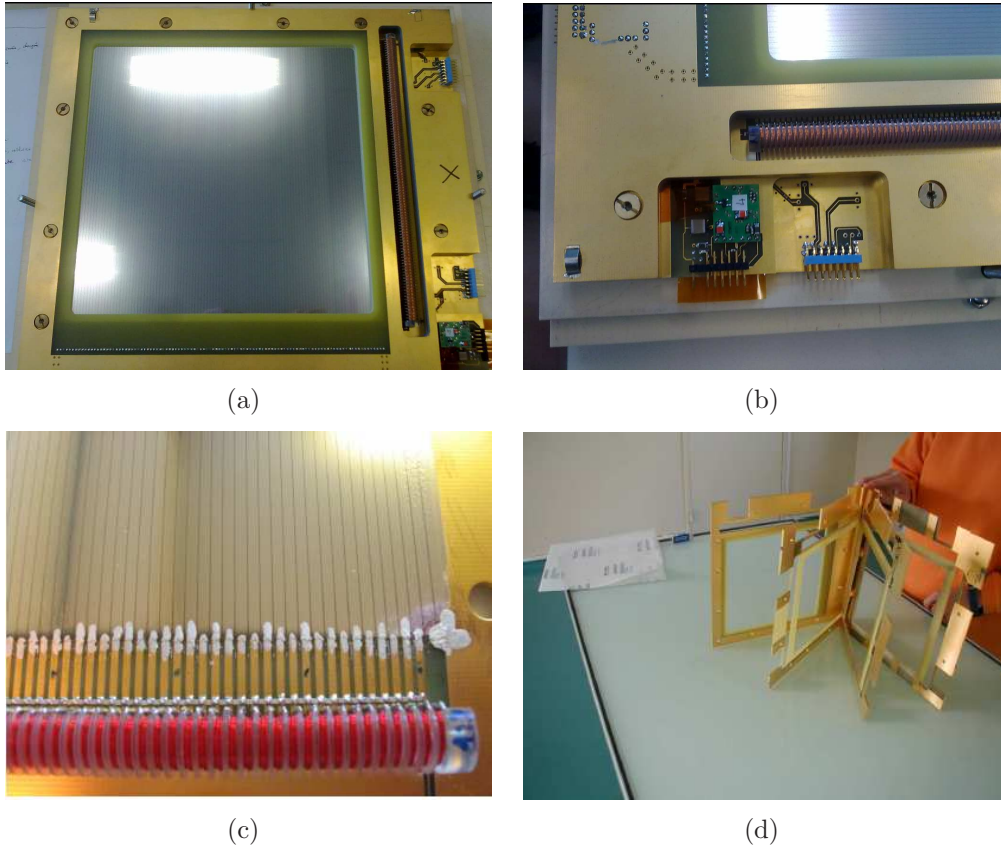


Figure 2.12: Photograph of a PPAC detector (a). The active area is  $20 \times 20 \text{ cm}^2$  and the delay line is on the right, with the anode readout preamplifier and the sockets for the cathode preamplifiers. A detailed view of the delay line and the readout preamplifiers is shown in (b), while the connections to the strips are shown in (c). The different epoxy frames that forms a single PPAC detector are shown in (d), before the installation of the electrodes.

The cathodes, placed on either side of the anode, are also made of Mylar foils with 2 mm wide strips of deposited aluminium and  $100 \mu\text{m}$  gaps in between the strips. Each strip of the cathode is connected to a delay line cell. The two stripped cathodes are orthogonally placed to get the two-dimensional position (X, Y) of the fission fragment hit. The delay line, also developed and built at IPN d'Orsay, is a plastic rod with a coiled copper

wire. The effective length of the rod is 20 cm and an intermediate space of 6 cm at each end connects the delay line to the readout preamplifiers.

The cathodes were connected to ground while a voltage of around 500 V was applied to the anodes. Such a value is a compromise between the amplification of the signals and the stability of the detector.

The 3.2 mm distance between the anode and each cathode is later filled with octafluoropropane ( $C_3F_8$ ) at 4 mbar pressure, circulating with a flux of 50 l/h for a set of 10 PPACs (corresponding to 5 l/h per detector).  $C_3F_8$  is a non-flammable gas with a fast signal rise time and large ion energy loss. Before 2003, isobutane ( $C_4H_{10}$ ) at 7 mbar was used, but it was changed because of new constraints on the safety requirements.

All this is enclosed in a stainless steel cylinder 1.63 m long, with its axis along the neutron beam line. The cylinder has a curved aluminium bottom that holds a maximum of 10 detectors and 9 interleaved targets. It is connected to the beam pipes by two flanges of 12 cm in diameter with 125  $\mu\text{m}$  Kapton foils to ensure the sealing of the chamber. To study the angular distribution of the fission fragments, the detectors and the targets are tilted 45° with respect to the neutron beam. The disposition of the detectors and the targets inside the chamber is shown in the right side of Fig. 2.13. The stainless steel cylinder is shown in the left side.

### 2.2.3. Description of the targets

A total of nine targets were used in this experiment, as indicated in Table 2.1: six  $^{232}\text{Th}$  targets, one  $^{237}\text{Np}$  target, one  $^{235}\text{U}$  target and one  $^{238}\text{U}$  target. The latter two were used as references, since their fission cross sections are considered as standards [111].

Target	Purity (%)	Number of targets	Mass (mg)	Activity
$^{232}\text{Th}$	99.99	6	6×12	6×60 Bq
$^{237}\text{Np}$	99.99	1	15	0.49 MBq
$^{235}\text{U}$	92.71	1	14	25 kBq
$^{238}\text{U}$	99.99	1	11.5	140 Bq

Table 2.1: Targets used in this experiment.

The targets were made of a thin radioactive layer (around 0.3 mg/cm<sup>2</sup>) deposited as an 80 mm diameter disk over aluminium foil. The thickness

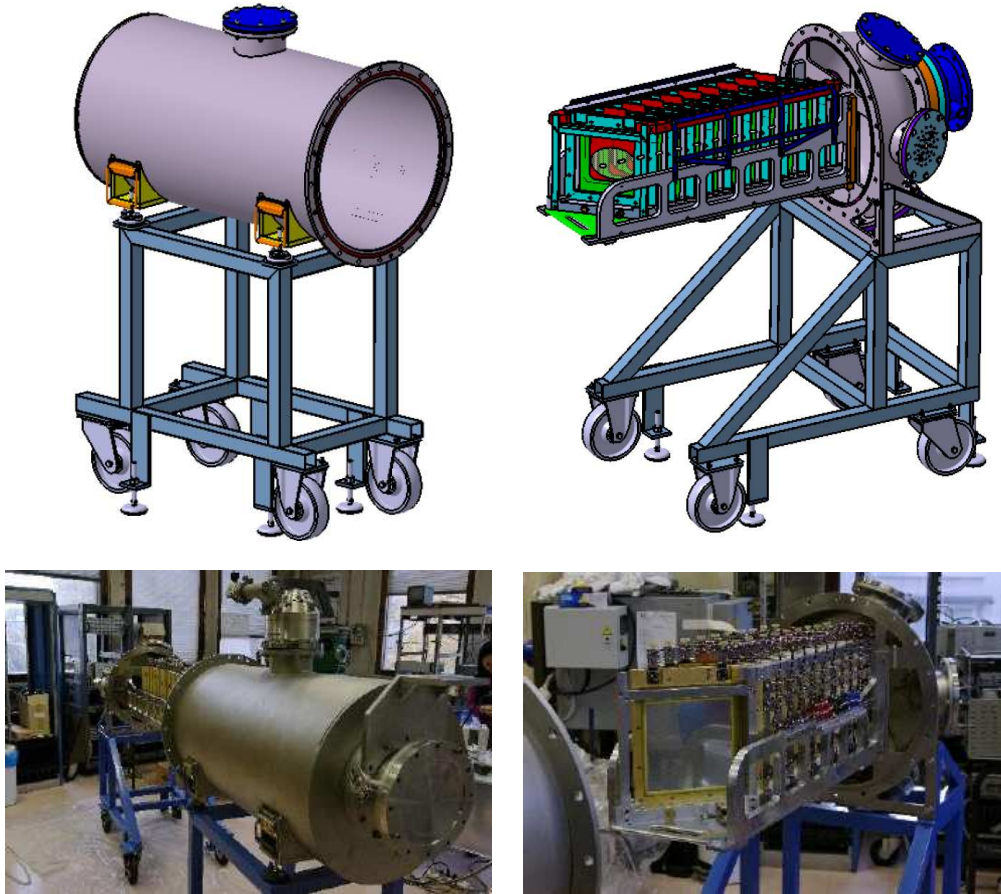


Figure 2.13: Artistic and real views of the fission chamber. In the left side, the stainless steel cylinder is shown. In the right side, the detectors and the targets inside the chamber can be seen.

of the aluminium foil was  $0.75\ \mu\text{m}$  for the  $^{232}\text{Th}$  targets and  $2.5\ \mu\text{m}$  for the remaining targets ( $^{235}\text{U}$ ,  $^{238}\text{U}$ , and  $^{237}\text{Np}$  targets). The aluminium foil was glued to a 1.5 mm thick epoxy frame.

The materials were deposited by a chemical method known as molecular plating, where a nitrate of the element is dissolved in isopropyl alcohol with a small amount of water. A 600 V potential is then applied for 15 minutes between a platinum foil and the aluminium foil used as backing to obtain an adequate amount of each material by electrodeposition. The material is then placed in an oven for a few hours to remove the residual alcohol and water. The resulting deposits are in the form of oxides ( $\text{UO}_2$  for the uranium samples, and  $\text{ThO}_2$  for the  $^{232}\text{Th}$ ) [110]. Very pure isotopes with negligible impurities were obtained for the  $^{232}\text{Th}$ ,  $^{238}\text{U}$ , and  $^{237}\text{Np}$  targets. In the  $^{235}\text{U}$

target, isotopic impurities of  $^{238}\text{U}$  (6.28% in number of atoms),  $^{234}\text{U}$  (0.74%) and  $^{236}\text{U}$  (0.27%) were found.

The targets were made by the radiochemistry group at IPN d'Orsay and had to be placed inside the target chamber prior to their transport to CERN.

# Chapter 3

## Experimental analysis

### 3.1. Raw data treatment

The previous chapter provided a description of how the experimental raw data are stored in the CASTOR system at CERN, after applying a zero-suppression algorithm that selects only those data frames crossing the threshold. Data are converted into Data Summary Tape (DST) files using a software package developed for the n\_TOF data. This software has a common component for use by all the n\_TOF detectors as well as specific routines for the pulse shape analysis of each one. As a result, only the relevant signal parameters for each detector are kept in the DST files.

The analysis routine for the PPAC detectors removes the high-frequency oscillations in the baseline by means of a peak recognition function based on a derivative filter. The original signal takes a bipolar shape after it has been derived, which can be seen in Fig. 3.1. Peak discrimination is done by applying certain conditions to the derived signal. The negative part must arrive first, to ensure the negative polarity of the signal. The bipolar signal must then cross two thresholds (one positive and one negative) which were determined from the study of real signals. Additionally, the time between both peaks of the derived signal and the ratio of both amplitudes are limited to certain values.

Signals fulfilling all these requirements are kept and two parameters are stored for them in the DST file: the zero-crossing time of the bipolar signal and its peak-to-peak amplitude. The same pulse shape analysis is applied to all the PPAC detector channels, though different conditions must be established for anodes and for cathodes.

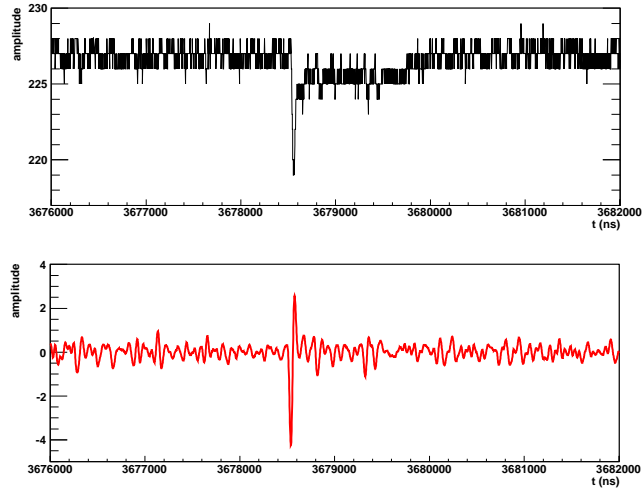


Figure 3.1: Raw data before (upper panel) and after (lower panel) the derivative filtering.

### 3.2. Fission event building

Each target is flanked by two PPAC detectors, so that the two fission fragments emitted in opposite directions hit both PPACs almost simultaneously. Two anode signals inside a time coincidence window is the signature of a fission event, as shown in Fig. 3.2. It is this time coincidence condition that makes it possible to reject most of the background produced by the  $\alpha$  emission of the radioactive targets and by spallation reactions in the materials surrounding the samples.

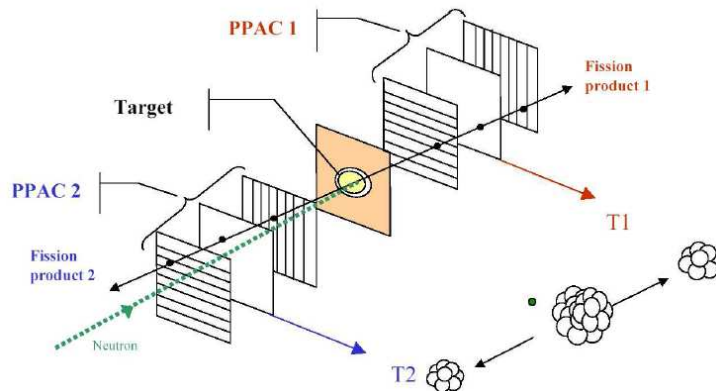


Figure 3.2: Fission event detected with two PPAC detectors.

The setup used for this experiment (Fig. 3.3) included nine targets interleaved in ten detectors in order to optimize the beam time. The task of identifying fission events is more complicated with this multiple target configuration, because each detector (except those at the ends) is reached by most of fragments emitted from two targets. Furthermore, as each fission fragment can cross more than one PPAC, more than two detectors are involved in the event building process. These ambiguities are solved by evaluating the timing conditions of the signals, which will be discussed in the following sections.

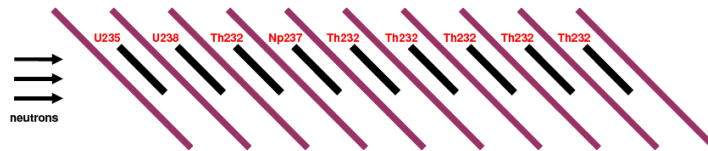


Figure 3.3: Top view of the experimental setup with ten PPAC detectors and nine targets in between. All the elements are tilted  $45^\circ$  around the vertical axis to cover a broader angular range. Targets are labelled from 0 to 9 following the neutron beam direction.

### 3.2.1. Anode signal coincidences

The algorithm used to search for the coincidences in this experiment was similar to the one used in previous PPAC measurements at n\_TOF [112]. Starting with the first anode (labeled as 0), a time window of 120 ns was opened to search for coincidences in the anode of the adjacent detector. This window is large enough to contain the signals from the complementary fragment crossing a first and a second detector. For every matching signal in the second detector, a new coincidence window was opened to search inside the anode signals of the next detector. This iterative process was stopped when no matching signal is found or when four different detectors have been searched, since the probability for a fission event of hitting more detectors is not significant. When several signals were available for the same fission event, we selected the combination that maximized the amplitudes in the detectors. All signals not included in the selected combination were kept for the next search. The different types of configurations obtained with this procedure were labeled as Type 2, Type 3, or Type 4, depending on the number of detectors involved (see Fig. 3.4). Once all the signals belonging to the anode of the first detector had been treated, the same procedure was

repeated with the next detector, excluding the signals that were included in any previous configuration.

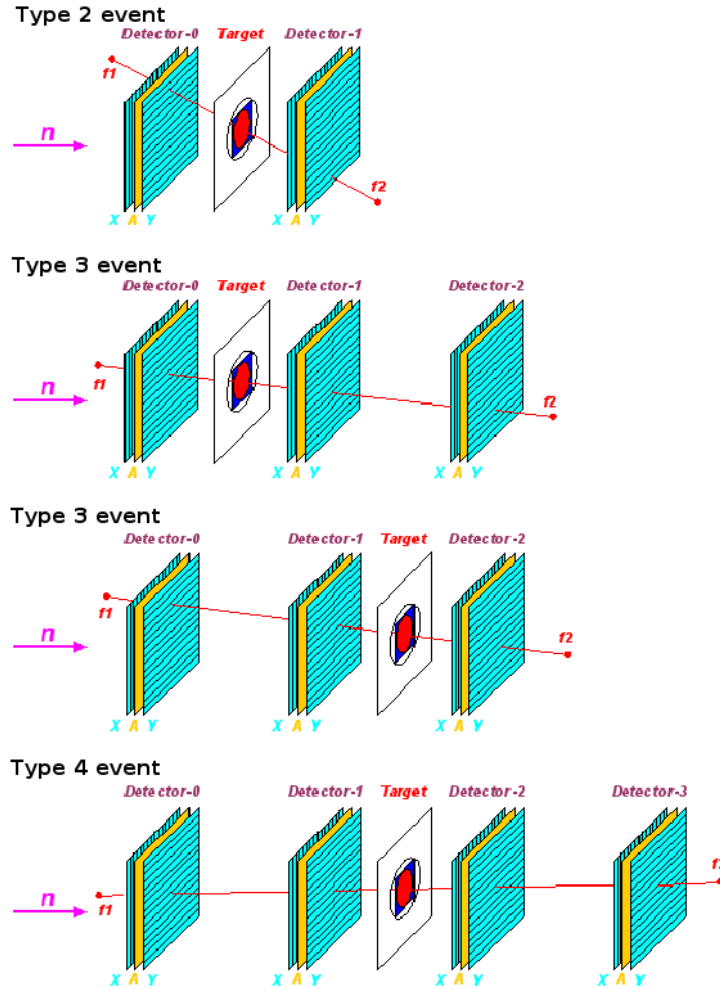


Figure 3.4: Schematic view of different possible configurations in which two, three or four PPAC detectors are hit by fission fragments. To facilitate comprehension of the figure, only the target producing the fission event is indicated. Note that two different cases are possible if three detectors are hit, depending on which fission fragment passes through two detectors.

Type 3 events involve detectors 0, 1 and 2. By comparing the time differences between  $t_0 - t_1$  and  $t_1 - t_2$ , it is possible to identify fission events coming from target 0 (the target between detectors 0 and 1) and distinguish them from events coming from target 1 (the target between detectors 1 and 2). This is shown in the bi-dimensional plot of Fig. 3.5. As expected,

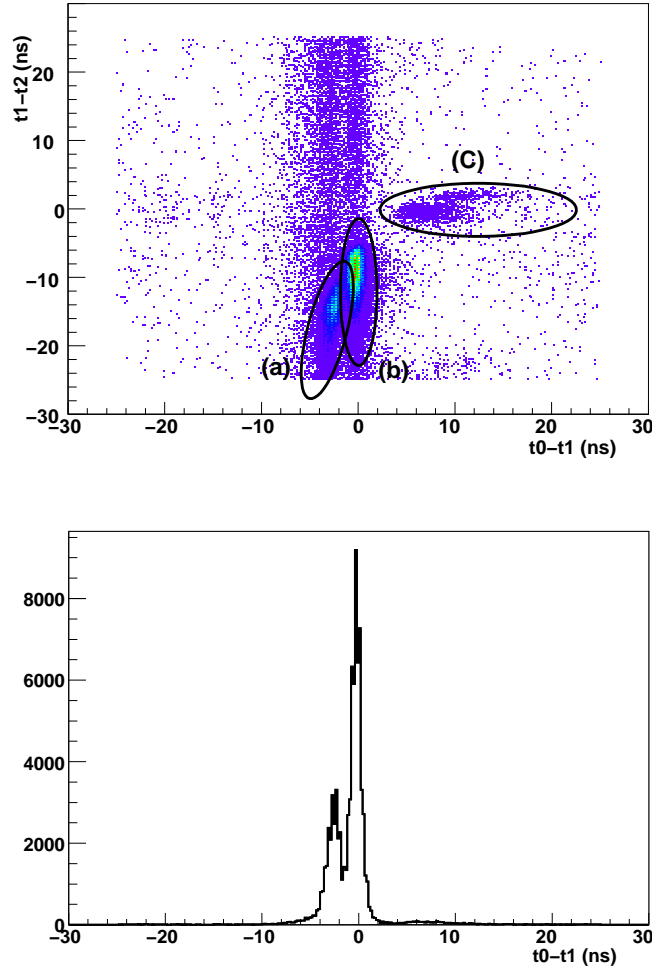


Figure 3.5: A two-dimensional plot of the time difference distribution for Type 3 events is shown in the upper panel. The fissions produced in target 0 ( $^{235}\text{U}$  sample) are labeled (a) if the heavy fission fragment passes through the backing, and (b) if the light fragment goes through. Events (c) correspond to fissions in target 1 ( $^{238}\text{U}$  sample). The projection on the X-axis is shown in the lower panel.

there is an accumulation of events around  $t_1 - t_2 = 0$ , which correspond to fissions in target 1 (sample of  $^{238}\text{U}$ ) and are therefore not correlated with the time difference  $t_0 - t_1$ . Fissions from target 0 (sample of  $^{235}\text{U}$ ) occur around  $t_0 - t_1 = 0$  and do not show any correlation with  $t_1 - t_2$ ; except that the difference is negative and below the value for the time needed to cross the distance between detectors.

Those events around  $t_0 - t_1 = 0$  and having a positive value of the difference

$t_1 - t_2$  correspond to coincidences between a Type 2 fission in target 0 and fragments coming from a fission produced in another target.

The average time difference for  $t_0 - t_1$  is not exactly zero due to the presence of the backing on the right side of the setup (facing detector 1) which slows down one of the fission fragments. In fact, in the upper panel of Fig. 3.5, two event families, labelled as (a) and (b), can be observed for fissions in Target 0. When the light fission fragment (LFF) goes through the backing and the heavy fragment (HFF) goes directly to the detector,  $t_0 - t_1 = 0$  (events (b) in Fig. 3.5). When the HFF goes through the backing, it slows down much more, leading to a greater difference in the  $t_0 - t_1$  arrival time (events (a) in Fig. 3.5). The same situation is observed for fissions in target 1, labeled as events (c) in the same figure. The time difference between two complementary fission fragments in adjacent detectors is less than 10 ns.

The number of counts for events (a) and (b) is greater than the number for events (c) due to the larger cross section for  $^{235}\text{U}$  than for  $^{238}\text{U}$ .

By using these bidimensional plots, the time windows for each detector were adjusted to keep only Type 2 events in a later step of the analysis. In other words, only the time and amplitude data from the two detectors adjacent to the target are saved. The coincidence method makes it possible to very efficiently reject the background due to the  $\alpha$  emission of radioactive targets. Fig. 3.6 shows how most of the low amplitude signals disappear after the coincidence condition between two PPACs is imposed. The high amplitude signals corresponding to fission fragments are reduced when the coincidence is imposed because only fragments coming from one of the two targets facing each detector are kept.

### 3.2.2. Looking for cathode signals

As explained in Chapter 2, each PPAC detector has two segmented cathodes placed in perpendicular directions. The strips are connected to a delay line where the signal is propagated reaching the readout preamplifiers at both ends. Therefore, the time difference between both signals provides either horizontal or vertical position information, depending on the orientation of the strips. The combined data from both cathodes allow us to know the impact position of the fission fragment in the PPAC.

The reading principle of the delay line position is described below with the help of Fig. 3.7. When the PPAC signal reaches the delay line at a position  $x$ , it is propagated in both directions arriving to the ends in times

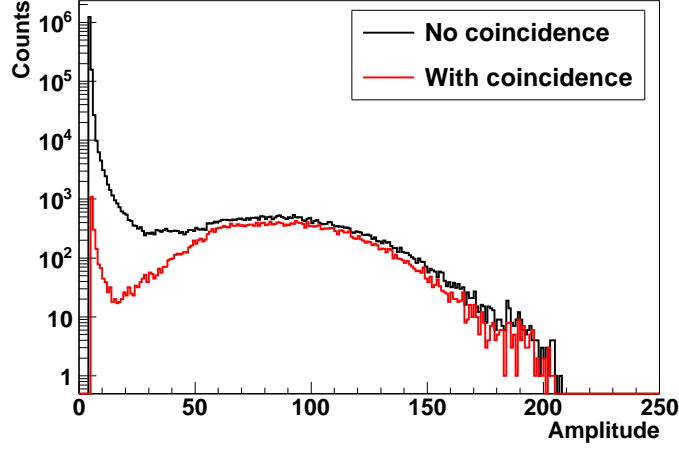


Figure 3.6: A good rejection of the background is achieved with the detection in coincidence of two PPACs. The low amplitude signals mainly correspond to the  $\alpha$  emission of the sample ( $^{235}\text{U}$  in this case). As each PPAC detects fission fragments from two targets, only events coming from one of them are kept.

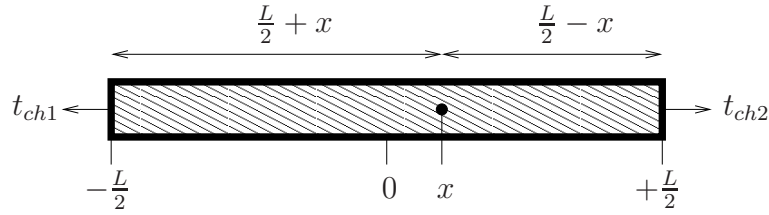


Figure 3.7: Signal propagation in a delay line of total length  $L$ .

$t_{ch1}$  and  $t_{ch2}$  after the signal creation, given by:

$$t_{ch1} = t_0 + \frac{1}{v} \left( \frac{L}{2} + x \right) \quad (3.1)$$

$$t_{ch2} = t_0 + \frac{1}{v} \left( \frac{L}{2} - x \right) \quad (3.2)$$

where  $t_0$  is the reference time given by the corresponding anode signal, and  $v$  is the propagation velocity of the signal along the delay line.

By subtracting Eqs. (3.1) and (3.2), the position  $x$  in the delay line can be obtained:

$$x = \frac{v}{2} (t_{ch1} - t_{ch2}) \quad (3.3)$$

And by summing the propagation times in both directions given by Eqs.

(3.1) and (3.2), we obtain the following relation:

$$t_{ch1} + t_{ch2} - 2t_0 = \frac{L}{v} \quad (3.4)$$

If we assume that the delay line length  $L$  and the propagation velocity  $v$  in it are constant, it is useful to define the total delay line propagation time (DLT), expressed in time units, as:

$$DLT = \frac{L}{v} \quad (3.5)$$

And, therefore, Eq. (3.4) becomes:

$$t_{ch1} + t_{ch2} - 2t_0 = DLT \quad (3.6)$$

Eq. (3.6) is known as the *diagonal condition*, because of the appearance of the two-dimensional time distribution  $t_{ch2} - t_0$  against  $t_{ch1} - t_0$ , which can be seen in Fig. 3.8. The real delay value for each cathode can be obtained by plotting the first term of Eq. (3.6), as in Fig. 3.8(b). These distributions peak at around 360 ns for all the cathodes and have a width of tens of ns because of the limited time resolution for the cathode signal readouts. The 60 ns difference with respect to the nominal length of 300 ns is due to the different readout preamplifiers used for the cathodes and for the anodes.

To find the cathode signals corresponding to a fission event, we start with an anode signal at time  $t_0$  and look for signals within  $t_0$  and  $t_0+400$  ns at the ends of both PPAC cathodes. A valid cathode event must produce a pair of signals, one at each end, with a sum of times about the DLT value and their amplitude ratio has to be between 0.5 and 2 (an attenuation of the signal along the delay line smaller than 50%). If these conditions are fulfilled, the signals are kept for further selection.

In this first stage of the analysis, every possible combination of the cathode signals found close to a selected anode signal was stored in a TTree ROOT object, so that a larger number of events than real ones were saved. Further signal selection will determine the correct combination in each case.

### 3.2.3. The spatial position of hits

As expressed in Eq. (3.3), the position of fission fragment hits in the PPAC can be obtained from the time difference of the cathode signals at both ends of the delay lines of each cathode (X and Y). We assume that a

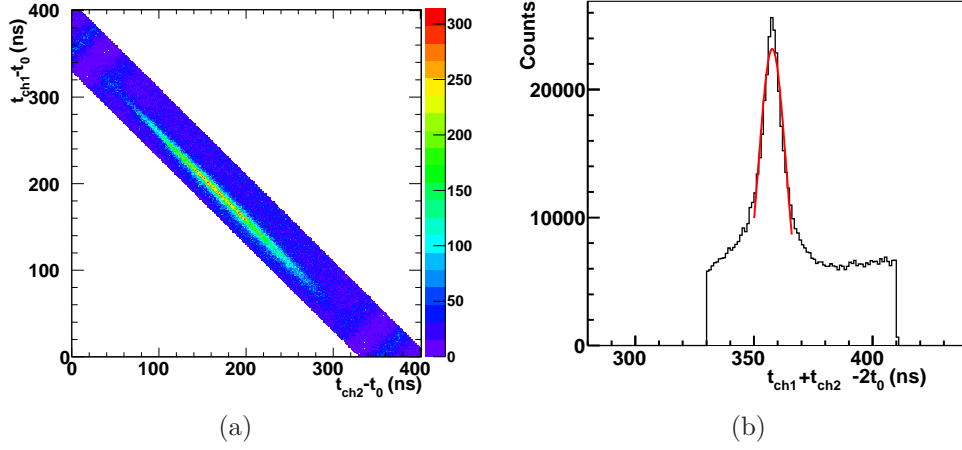


Figure 3.8: The correlation between the propagation times along the delay line gives a diagonal shape (a). The real length of the delay line, in time units, is shown in (b) where the center of the distribution is at 360 ns rather than at the nominal value of 300 ns due to the preamplifiers.

time difference equal to zero in both signals of each cathode corresponds to the mid-position of the delay line, since a signal produced at the delay line center position reaches both ends at the same time, and the delay introduced by the electronics is much smaller than the length of the delay line. The propagation velocity  $v$  of the signals along the delay line is required for Eq. (3.3) and is equal to the length of the delay line (200 mm) divided by the propagation time. Thus:

$$\frac{1}{2} (t_{ch1} - t_{ch2}) = \frac{x}{v} = t_{prop} \quad (3.7)$$

where  $t_{prop}$  is the propagation time of the signal along the delay line. If we represent the experimental values of the first term of Eq. (3.7), we obtain the distribution shown in Fig. 3.9. The real limits of the delay line are around +150 ns and -150 ns and the sharp peaks beyond these values correspond to signal reflections where the delay line connects to the readout preamplifiers. The limits measured in this way are given in Table 3.1, though a dedicated measurement at the laboratory is also foreseen. It is also possible to identify time differences introduced by both preamplifiers which would shift the center of the distribution out of zero.

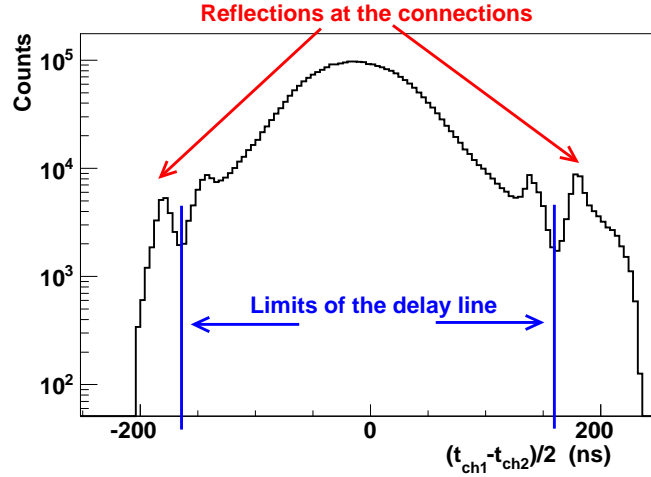


Figure 3.9: Propagation time differences along a delay line. The values beyond the indicated limits line correspond to signal reflections in the connections between the delay line and the readout preamplifiers.

Detector	Delay line propagation time (ns)			
	Cathode X		Cathode Y	
	Lower limit	Upper limit	Lower limit	Upper limit
0	-160.0	+160.0	-163.5	+162.0
1	-160.0	+160.0	-160.0	+160.0
2	-162.5	+160.0	-160.0	+162.5
3	-160.0	+160.0	-160.0	+160.0
4	-160.0	+160.0	-160.0	+162.0
5	-160.0	+160.0	-162.5	+164.0
6	-156.0	+164.0	-160.0	+160.0
7	-160.0	+156.0	-160.0	+160.0
8	-160.0	+160.0	-160.0	+158.0
9	-160.0	+160.0	-156.0	+160.0

Table 3.1: Propagation time in both directions of each delay line of the different PPAC detectors, as measured from the experimental data.

### 3.2.4. Selection of cathode signals

As mentioned in Sec. 3.2.2, for each fission event, every possible combination of cathode signals close to a given anode signal is stored if its ratio of amplitude is between 0.5 and 2. In this way, the number of saved events is

larger than the number of real ones. To determine the spatial position of the fragments hitting in both PPACs, the combination of signals corresponding to each fission event must be ascertained so that, finally, we keep only two signals per cathode in a fission event.

Several conditions were applied to the cathode signal pairs in order to select only one combination from among all those available for each anode signal. Every pair of cathode signals that did not fulfill the diagonal condition given by Eq. (3.6) within the limits  $330 \leq DLT(\text{ns}) \leq 410$  was discarded. The selection routine searches for the combinations with a more strict time window around the corresponding DLT. If several combinations were still available after this step, a further selection is performed according to the ratio of amplitudes of the cathodes. As the ratio of the amplitudes of both signals is related to the attenuation along the delay line, this ratio must vary linearly with the position as shown in Fig. 3.10, so that a graphical cut is performed in order to eliminate those signals far from this linear function.

Finally, the spatial position (X and Y) in the detector was calculated for the remaining combinations and those found to be outside the real limits of the detector were discarded. With this procedure, we obtain a unique set of cathode signals for each anode signal, which are saved into an object of a TTree class in a ROOT file.

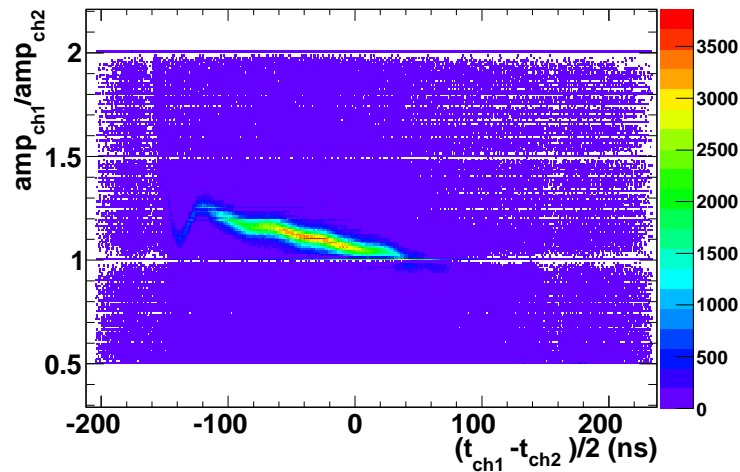


Figure 3.10: Example of the linear dependence of the ratio of amplitudes between both cathode signals with the position, given by their time difference.

### 3.3. Reconstruction of the fission fragment trajectory

Once fission events have been defined by unambiguously associating cathode signals with anode signals, the fission fragment trajectory can be reconstructed using the position information provided by these signals. If we assume that they are emitted from the target in opposite directions in the center-of-masses frame, we can reconstruct their trajectories from the X and Y positions where the fission fragments hit the two adjacent PPACs. This hypothesis is valid for neutron energies up to 100 MeV, where fission occurs at rest. Above this energy, such an approximation is no longer valid and the linear momentum transferred to the nucleus must be taken into account. The effect of this assumption will be discussed later on.

In order to study the angular distribution, the relevant physical parameter is  $\cos \theta$ , where  $\theta$  is the emission angle of the fission fragments with respect to the neutron beam. The reference frame is shown in Fig. 3.11. The coordinate origin is in the center of the target, and the detector surfaces are parallel to the X-Y plane. The detectors and the target are placed along the Z axis. It is easy to determine the coordinates of the impact point in each detector using this reference system, since the X and Y coordinates are given directly by the cathode signals, being the value of the Z coordinate the distance from the target to the detector. A displacement in the X coordinate of both detectors with respect to the center of the target has to be taken into account. If the impact points in the detectors are  $P_0 = (x_0, y_0, z_0)$  and  $P_1 = (x_1, y_1, z_1)$ , the emission direction is given by the vector:

$$\vec{V} = P_1 - P_0 = (x_1 - x_0, y_1 - y_0, z_1 - z_0)$$

And as indicated in the same figure, the direction of the neutron beam is given by:

$$\vec{W} = (1, 0, -1)$$

The angle between both vectors can be obtained by using the scalar product:

$$\cos \theta = \frac{\vec{V} \cdot \vec{W}}{|\vec{V}| \cdot |\vec{W}|} \quad (3.8)$$

where  $|\vec{V}|$  and  $|\vec{W}|$  are the magnitudes of  $\vec{V}$  and  $\vec{W}$ .

The relationship between this reference system determined by the detectors, and a reference system where the beam axis determines the z direction

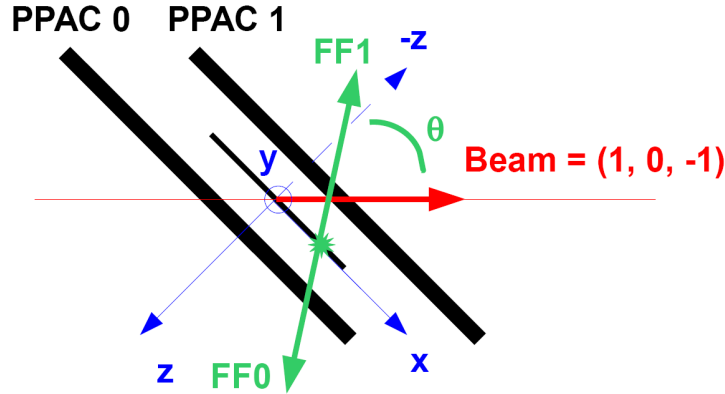


Figure 3.11: Reference frame used in the calculation of the emission angle of the fission fragments,  $FF0$  and  $FF1$ , with respect to the beam direction.

is given by a rotation of  $45^\circ$  around the  $y$  axis. Therefore, the angle  $\phi$  around the beam axis can be calculated in the rotated coordinates (primed) as:

$$\phi = \arctan\left(\frac{y'_1 - y'_0}{x'_1 - x'_0}\right) \quad (3.9)$$

In a certain number of fission events, some of the cathode signals are not found. When this occurs, the position at the detectors and the emission angles  $\cos\theta$  and  $\phi$ , are saved with a dummy value so that they can be easily identified as non-localized fission events. This prevents them from being discarded, as they are useful for calculating the fission cross section; even though they provide no information on the angular distribution.

### 3.3.1. Linear momentum transfer

In neutron-induced reactions, part of the kinetic energy of the incident neutron is transferred to the target nucleus, so that fission does not occur at rest and, therefore, the fission fragments are emitted in an angle that is not equal to  $180^\circ$  in the laboratory frame.

It is well-known that there is a kinematical limit for the fraction of the longitudinal momentum of the incident particle being transferred to the target. In the case of a target being a composite system, the transfer limit drops as a function of the projectile energy. Experimental studies [113, 114] have shown that, in the case of proton-induced fission of thorium and uranium, the transfer of longitudinal momentum is a smooth function of the proton

energy, with a maximum around 350 MeV/c at proton energies of 1 GeV. Neutrons are expected to have a similar behaviour. In Fig. 3.12, a comparison with reactions induced by deuteron,  $\alpha$  and heavy ions is shown; the hypothetical case of a full momentum transfer is indicated by the solid curve.

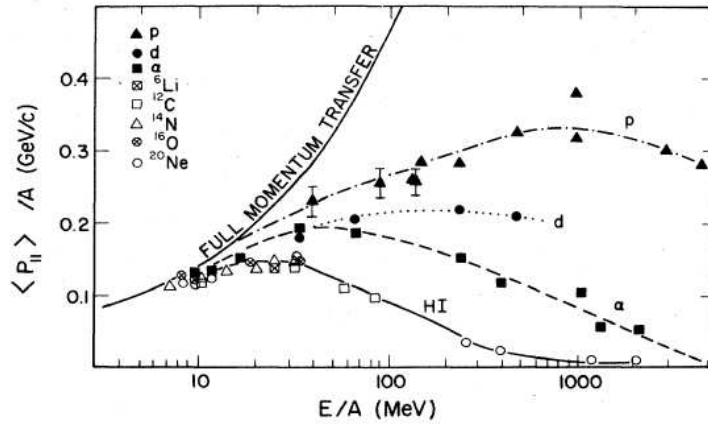


Figure 3.12: Average linear momentum transfer per projectile nucleon as a function of the projectile energy per nucleon for reactions with Th and U targets. Fig. from Ref. [114].

This effect implies that, at large neutron energies, the fission fragments are not emitted at  $180^\circ$ . However, the angle measured in our setup is not the emission angle given in laboratory frame since we have no information on the emission point of the fragments. Therefore, the measured trajectory given by the impact points of both fission fragments results in a measured angle  $\theta_m$  that is close to the angle in CM frame  $\theta_{cm}$ , even at large neutron energies, as it will be shown in the simulation results given in Chapter 4.

### 3.4. Neutron energy calculation

As it was stated previously, our fission studies rely on the precise measurement of the neutron kinetic energy, calculated from the length of the flight path and the time of flight, according to the relativistic formula:

$$E = (\gamma - 1)m_n c^2 \quad (3.10)$$

where  $\gamma$  is the Lorentz factor and  $m_n$  is the rest mass of the neutron. Using the flight path  $L$  and the time-of-flight  $T$ , this equation leads to:

$$E = m_n c^2 \left( \sqrt{\frac{1}{1 - \frac{1}{c^2} \left(\frac{L}{T}\right)^2}} - 1 \right) \quad (3.11)$$

Since the neutrons are produced at a spallation source, the effective length of the flight path is the sum of the geometrical length and the “moderation distance”: the effective distance travelled by the neutrons during the moderation process inside the spallation target and the moderator. The effective length  $L$  can be expressed as the sum of a fixed length  $L_0$  and an energy-dependent term  $\Delta L(E)$ , where  $L_0$  accounts for the geometrical distance and the independent-energy term of the moderation distance [115].

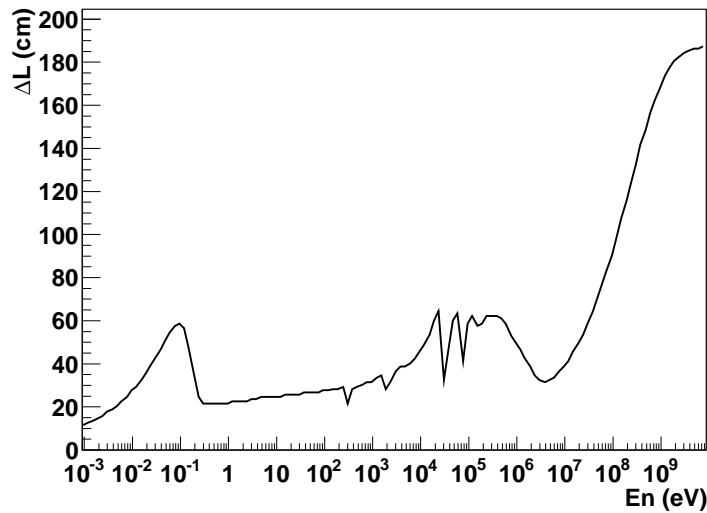


Figure 3.13: Energy dependence of the moderation distance in the  $n$ -TOF facility with the new spallation target, based on simulations [116].

The energy-dependent term of the moderation distance  $\Delta L$  has been studied by means of FLUKA<sup>1</sup> simulations [116] and is shown in Fig. 3.13. This term is much smaller than the geometrical distance  $L_0$  of about 185 m. Therefore, the neutron energy can be calculated through an iterative procedure in which a first approximate value of the neutron energy  $E_0$  is calculated from the geometrical distance  $L_0$ . This energy is used to calculate a moderation distance  $\Delta L(E_0)$ , and a new value of the energy  $E_1$  is obtained

<sup>1</sup>FLUKA is a Monte Carlo simulation package for calculations of particle transport and interactions with matter. It is widely applied in nuclear and particle physics [117, 118].

from  $L_0 + \Delta L(E_0)$  in Eq. (3.11). The process is repeated until the result converges. In our case, only three iterations are needed to reach a convergence value with  $|E_n - E_{n-1}|/E_n < 10^{-4}$ .

The precise value of the length  $L_0$  was calculated by comparing our fission rate with the lowest-energy evaluated resonances of  $^{235}\text{U}(\text{n},\text{f})$  found in the ENDF-B/VII.1 evaluation [13]. Our experimental values were systematically compared with the evaluated values in the entire resolved resonances range (see examples in Fig. 3.14), resulting in a value  $L_0 = 183.8$  m for the  $^{235}\text{U}$  sample. The  $L_0$  value for the other samples was obtained by adding the existing distance between the  $^{235}\text{U}$  sample and each target. The fission cross section ratio  $\sigma_f(^{238}\text{U})/\sigma_f(^{235}\text{U})$  was used to check the energy calculation above 1 MeV, and we can conclude that the energy calculation is correct in the entire studied range.

The time of flight  $T$  is given by the difference between the anode signal  $t_0$  of the detector nearest the neutron source and the  $\gamma$ -flash signal  $t_g$ , which determines the origin of time and will be explained in Sec. 3.4.1. An additional offset  $t_{\text{offset}} = L/c$  due to the time needed for the  $\gamma$ -flash to travel along the flight path must also be included.

### 3.4.1. Properties of the $\gamma$ -flash

A large amount of gamma rays and relativistic muons are produced when the proton beam hits the spallation target. The magnet located in the beam line deflects most of the charged particles, but not the  $\gamma$  rays, which arrive at the Experimental Area before the neutron beam at the speed of light. The exact composition of this  $\gamma$ -flash is unclear and it temporarily “blinds” most detectors, thereby imposing a limit on the highest neutron energy that can be achieved. However, the  $\gamma$ -flash effect in the PPACs is less dramatic due to their  $\gamma$  insensitivity. In fact, the signal produced by the  $\gamma$ -flash in a PPAC is similar to those produced by the fission fragments, with an amplitude that depends on the proton beam intensity.

Since the  $\gamma$ -flash passes through all the detectors within 2 ns, an interval equivalent to the 500 MHz sampling rate, it can be considered instantaneous and provides a common time reference for each proton pulse. To identify the  $\gamma$ -flash, an anode coincidence search routine is implemented to identify simultaneous hits in at least 8 detectors. In this way the  $\gamma$ -flash signal can be distinguished from earlier signals produced by  $\alpha$  disintegration or by nuclei emitted in reactions induced by neutrons with no correlation to the proton pulse. The time values of the hit detectors are averaged and the resulting

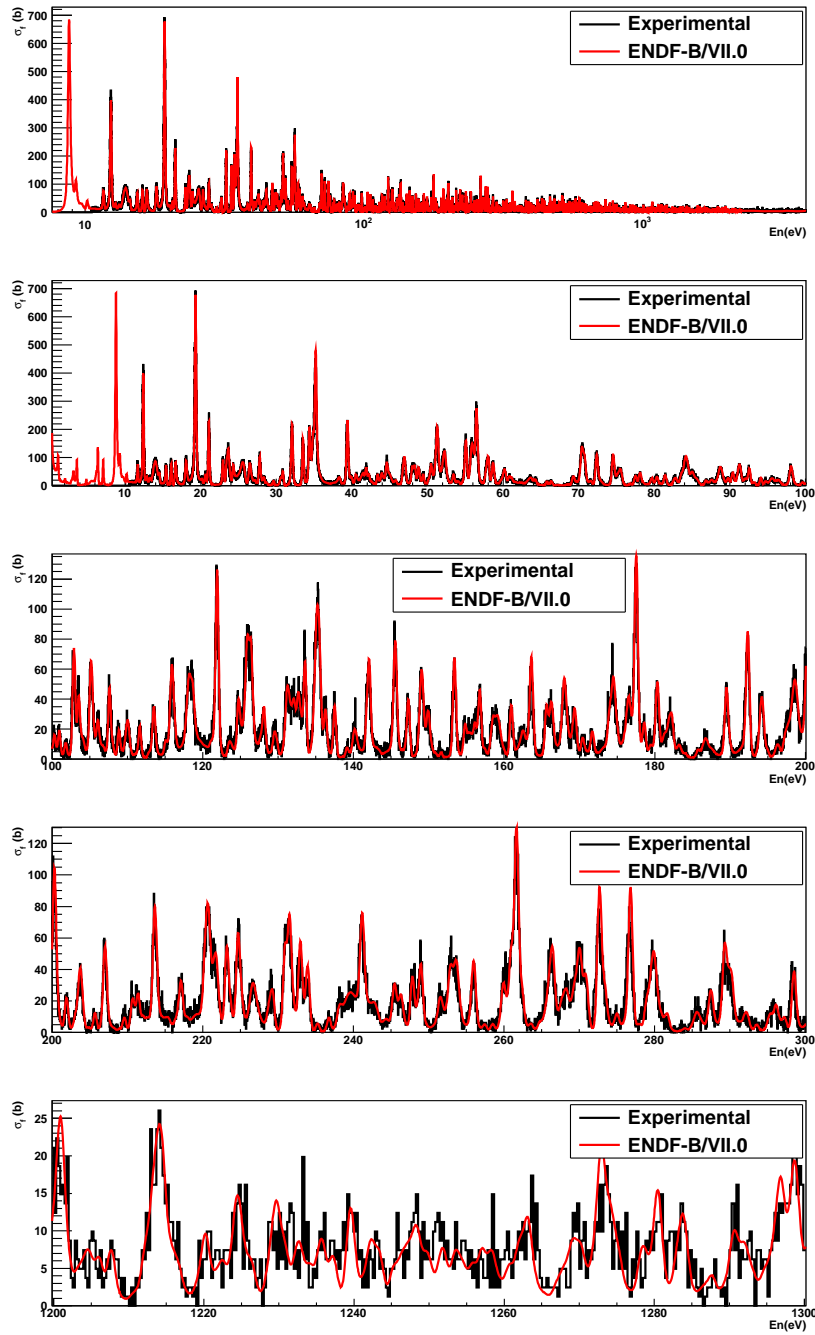


Figure 3.14: Experimental fission rate of  $^{235}\text{U}$  at resolved resonances region energy, compared with the ENDF-B/VII.1 evaluation [13].

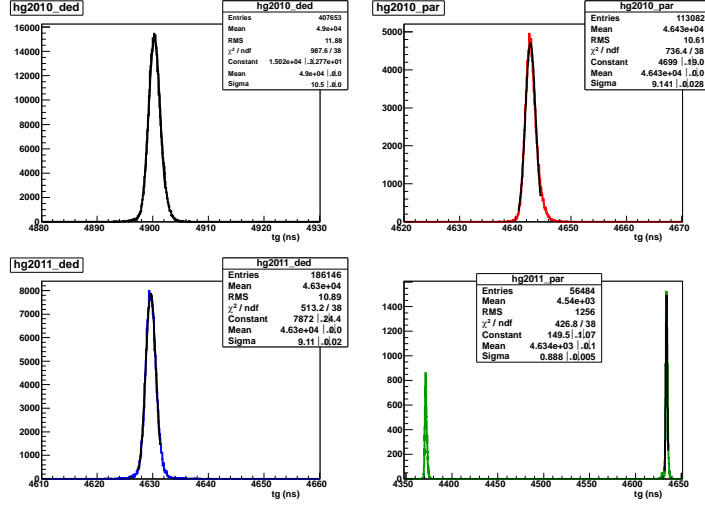


Figure 3.15: Time distribution of the  $\gamma$ -flash for every PS pulse during the 2010 and 2011 runs. The dedicated and parasitic pulses have different times, but the width of the distribution is around 1 ns for all pulses.

value is considered the origin of time which is used to calculate the neutron energy in Eq. (3.11) of Section 3.4.

The  $\gamma$ -flash timing depends on the type of PS pulse (dedicated or parasitic), since the PS trigger signal is different for each type of pulse. Fig. 3.15 shows the time distribution of the  $\gamma$ -flash signals for dedicated and parasitic pulses in both experimental campaigns (2010 and 2011). In the 2011 campaign, the delivery time of some of the parasitic pulses was very close to that of the dedicated pulses. The width of the time distributions was around 1 ns for all pulses.

### 3.5. Selection of fission events

Fission events were saved into an object of the TTree class to a ROOT file. After applying the selection procedure described in this chapter, the amplitude and time variables were stored for the remaining anode and cathode signals from the two PPACs adjacent to each of the nine targets. The neutron energy is also calculated and saved for each event. Other values calculated from the cathodes are also stored for each fission event, such as the X-Y positions at the detectors and the  $\cos\theta$  and  $\phi$  of the emission angles. The ROOT file also stores other technical parameters, including the time of the  $\gamma$ -flash, the type (dedicated or parasitic) and intensity of the proton

pulse, and the run and event numbers.

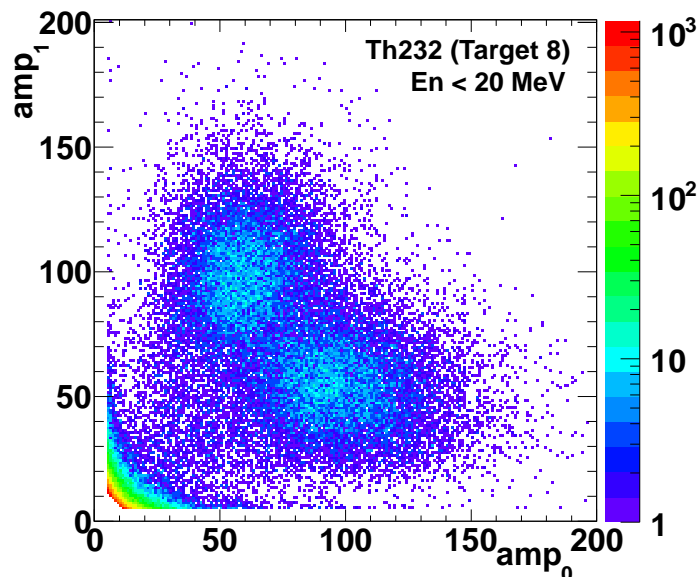


Figure 3.16: Two dimensional plot of both PPAC amplitudes for a  $^{232}\text{Th}$  target. The fission events are well separated from the random coincidences, which present lower amplitudes.

These time and amplitude variables can be represented in bi-dimensional plots that make it possible to discriminate fission events from the remaining background caused by random coincidences in two PPAC detectors. An example of the amplitudes from both PPACs is shown in Fig. 3.16 for one of the  $^{232}\text{Th}$  targets, where the  $amp_1$  variable corresponds to the amplitude of the PPAC that faces the backing. Fission events are well separated from random coincidences that correspond to the low-amplitude background. The presence of the backing breaks the symmetry in the amplitude distributions since one of the fission fragments must pass through it so that part of its energy is deposited inside the backing. Its resulting lower energy produces a lower amplitude signal in the detector.



# Chapter 4

## Simulation work

Knowing the detection efficiency of the present setup is an important issue in the data analysis. To study the angular acceptance for the experimental setup and how the detection efficiency depends on the emission angle of the fission fragments, a simulation was done using Geant4. The effect of the thicker backing where the reference sample  $^{235}\text{U}$  is deposited, compared to the thinner backing used for  $^{232}\text{Th}$  samples was also studied to properly account for this effect in the analysis of the experimental data, which will be presented in Chapter 5.

To show the advantages of the present geometrical configuration for measuring the angular distributions of fission fragments, the results obtained for this setup with detectors and targets tilted  $45^\circ$  with respect to the beam direction were compared with results from a perpendicular target-detector placement.

Geant4 is a software toolkit implemented in the C++ programming language that uses Monte Carlo methods and object-oriented technology to simulate the passage of particles through matter [119]. It includes features that allow the user to control all aspects of the simulation process. Thus, complex geometries can be defined involving a wide variety of materials that reproduce the constitution of the real system. The generation of primary particles from events is also defined by the user. Geant4 tracks the particles through materials and external electromagnetic fields, and simulates the response of sensitive detector components in such a way that all the information on events and tracks can be stored for later use in specific analysis frameworks. Geant4 was designed and developed through an international collaboration and is widely used in different applications including high energy, nuclear and accelerator physics, space science, nuclear medicine and

radiation protection studies.

For the simulation work presented here, the detection setup and a fission event generator were implemented in Geant4. The fission reaction between the neutron and the nucleus was not considered in the event generator that directly provides two fission products according to the procedure described in the next section. The effect of the linear momentum transferred to the nucleus in the outgoing angles and kinetic energies of the fission fragments was studied for a few particular cases.

## 4.1. Description of the simulation setup

A simplified version of the real setup was implemented with Geant4, using only two PPAC detectors with one target in between, as shown in Fig. 4.1. In each event, two fission fragments were emitted in opposite directions from a random point inside the target and then propagated through the material layers of the detectors. Since our interest was specifically the slowing down of the fission fragments in the detection setup, only those material layers participating actively in this process were included in the simulation and the epoxy frames of the PPACs and the target support were ignored.

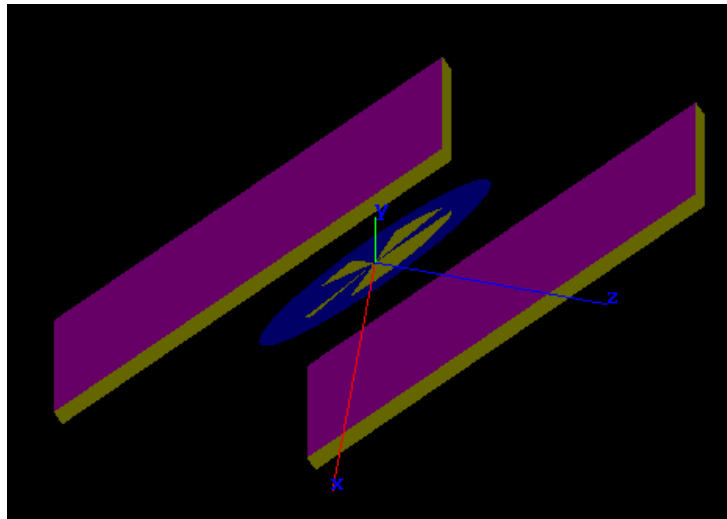


*Figure 4.1: Geometry used in the Geant4 simulation, with one circular target deposited over an aluminium backing and placed between two PPAC detectors.*

Each simulated PPAC detector consisted of three thin layers: one for the central anode and two for the cathodes on either side of it. All the electrodes

were simulated using Mylar foils  $20 \times 20 \text{ cm}^2$  and  $1.5 \text{ }\mu\text{m}$ -thick, separated by a 3.2 mm gap filled with gas. The stripped characteristic of the cathodes and the production of detector signals were not included, since they were not relevant to the slowing down of fragments.

The simulated target was a circular layer 80 mm in diameter made of 15 mg of uranium or thorium oxide ( $\text{UO}_2$  or  $\text{ThO}_2$ ) deposited over an aluminium backing. The thickness of the backing layer was  $0.75 \text{ }\mu\text{m}$  for the  $^{232}\text{Th}$  samples, and  $2.5 \text{ }\mu\text{m}$  for the  $^{235}\text{U}$  and  $^{238}\text{U}$  samples (see Section 2.2.3). The distance between the target and each detector was 25 mm.

All the materials were immersed in  $\text{C}_3\text{F}_8$  gas at 5 mbar pressure. To simplify the task of comparing two different geometrical configurations, the simulation code was written in such a way that the angle of targets and detectors could be easily set to the desired values of  $0^\circ$  or  $45^\circ$ , with respect to the beam direction.

## 4.2. Fission event generator

We recall from Section 3.2 that detection of both fission fragments is required in order to define a fission event. In each simulated event, therefore, two complementary fission fragments were emitted, in opposite directions, from a random position inside the target volume. The fission fragment characteristics (charge, mass, kinetic energy and emission angle) of each simulated event were selected from among certain values, using a fission event generator specifically created for this purpose. The possible values depend on the target material as are explained in the following sections.

### 4.2.1. Mass and charge distribution

Fission fragments are emitted with a certain mass distribution (and hence a charge distribution) that depends on the target nucleus and on the energy of the incident neutron (see Chapter 1). Evaluated fission yield data for neutron-induced fission in a large variety of nuclei are available in the ENDF/B-VII.1 library [13] and were used in our fission event generator to weight the selection of complementary pairs of fission fragments. The mass distributions of the fragments in  $^{235}\text{U}(\text{n},\text{f})$  and  $^{232}\text{Th}(\text{n},\text{f})$  reactions are shown in Fig. 4.2 for different neutron energies.

To simulate a fission event, a first fission fragment is randomly selected according to a probability distribution given by the evaluated fission yield of

the reaction of interest. For the sake of simplicity, the complementary fission fragment is chosen as the one needed to get the total amount of protons and neutrons of the fissioning nucleus, after randomly removing a number of neutrons in this second fragment, given by a Gaussian distribution centered in 2 neutrons and  $\sigma=1.5$ .

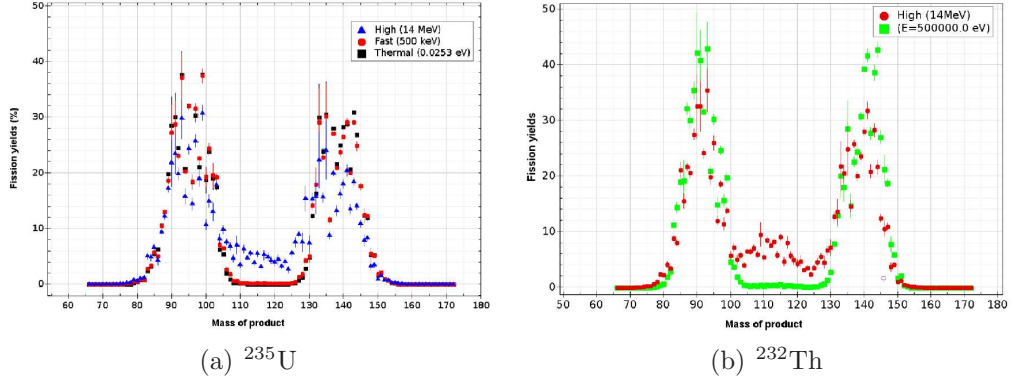


Figure 4.2: Fission yields of  $^{235}\text{U}(n,f)$  and  $^{232}\text{Th}(n,f)$  given by the ENDF/B-VII.1 evaluation [13] for different neutron energies.

#### 4.2.2. Energy distribution

The total kinetic energy released in fission (Section 1.5.2) is given by Viola's systematic [69], which is expressed by Eq. (1.30), and repeated here for convenience:

$$TKE = 0.1189 \cdot Z^2/A^{1/3} + 7.3 \text{ MeV} \quad (4.1)$$

Because of momentum conservation, this energy, which depends on the fissility parameter of the compound nucleus that is formed by neutron capture in the target nucleus, is distributed between both fission fragments according to the inverse relation of their masses, so that:

$$\frac{E_{HFF}}{E_{LFF}} = \frac{A_{LFF}}{A_{HFF}} \quad (4.2)$$

The subindexes HFF and LFF correspond to Heavy and Light Fission Fragments, respectively. In addition:

$$TKE = E_{HFF} + E_{LFF} \quad (4.3)$$

From this system of equations, the kinetic energies of both fission fragments are given by:

$$E_{HFF} = \frac{TKE}{\left(1 + \frac{A_{HFF}}{A_{LFF}}\right)} \quad \text{and} \quad E_{LFF} = \frac{TKE}{\left(1 + \frac{A_{LFF}}{A_{HFF}}\right)} \quad (4.4)$$

Due to neutron evaporation, the energy of the second fission fragment (which can be either heavy or light) will be reduced according to the number  $\nu$  of emitted neutrons by a factor  $(A - \nu)/A$ .

Thus, the kinetic energies  $E_{HFF}$  and  $E_{LFF}$  obtained from these calculations are corrected by neutron emission and associated to the fission fragments by the event generator.

### 4.2.3. Angular distribution

Fission fragments are not emitted isotropically, as was discussed in Chapter 1, but with an angular distribution that depends on the nucleus and on the neutron energy. This angular distribution can be expressed as a series of Legendre polynomials in  $\cos \theta$ , where  $\theta$  is the angle between the direction defined by the emitted fragment and the direction of the neutron beam:

$$W(\cos \theta) = \sum_{n=0}^N A_n P_n(\cos \theta) \quad (4.5)$$

As we impose the detection of both fission fragments, there is a forward-backward symmetry of the fission process, so that only even-order polynomials are considered. Appendix A provides a brief summary of the mathematical properties of the Legendre polynomials.

In our fission event generator, the two fission fragments were emitted in opposite directions in the center-of-mass frame, and the linear momentum transferred to the fissioning nucleus by the incident neutron can be set to the desired value. In this center-of-mass frame, the emission angle with respect to the beam direction was randomly chosen according to a probability distribution given by a series of Legendre polynomials. A specific angular distribution could be easily defined by setting the coefficients  $A_n$  to the desired values.

The low-energy neutron-induced fission of  $^{235}\text{U}$  is isotropic so that it is used as a reference to measure angular distributions. Therefore, in order to calculate the efficiency of the detection setup, an isotropic distribution was

used for the low-energy neutron-induced fission of  $^{235}\text{U}$ . This was achieved by setting  $A_0 = 1$ , and all other  $A_n$  coefficients equal to zero.

Up to here, the characterization of the fission fragment properties was given assuming that the fission occurs at rest. However, for neutrons of the higher energies, the nucleus acquires a linear momentum that is not negligible. In order to take into account this linear momentum transfer, the kinetic energies and the emission angles of the fission fragments have been transformed from the center-of-mass frame (where fission happens at rest) to the laboratory frame by using the Lorentz transformations presented in Appendix B. It is worth to mention that, actually, the velocity  $v_{cm}$  acquired by the nucleus is lower than the one corresponding to an elastic collision. Data used in this work were taken from the experimental results shown in Fig. 3.12 for proton-induced reactions. It can be seen that the linear momentum transferred to the nucleus increases more slowly than the energy of the incident particle, and reaches a maximum of  $\sim 350$  MeV/c for proton energies around 1 GeV.

This transfer of momentum causes that the relative angle of emission between both fission fragments is not  $180^\circ$ , contrary to what was assumed in the trajectory reconstruction of fission events. However, the angle  $\theta_m$  measured in this setup is different from the emission angle in the laboratory frame since it is not possible to know the emission point of the fission fragments, but only their final positions at the PPACs.

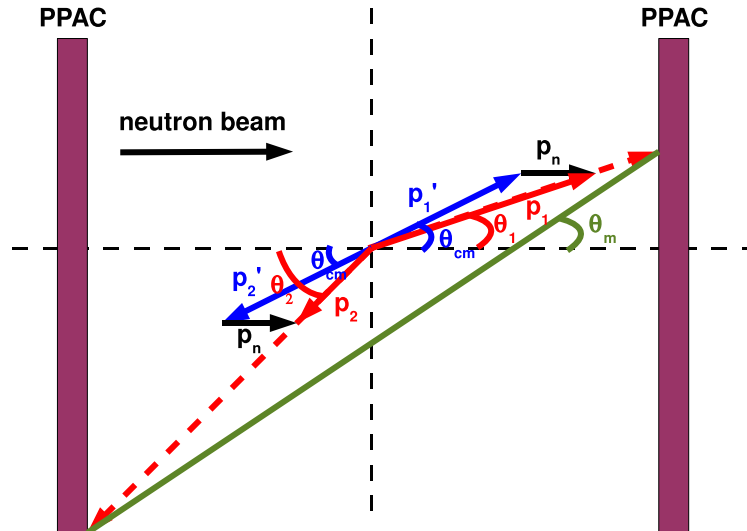


Figure 4.3: Kinematics of a fission event detected with two PPACs.

This situation is schematically shown in Fig. 4.3, where the PPACs were drawn perpendicularly to the neutron beam for the sake of simplicity: two fission fragments are emitted in opposite directions in the center-of-mass frame, with momenta  $p'_1$  and  $p'_2$  at an angle  $\theta_{cm}$ . The incident neutron transfers a momentum  $p_n$  to the nucleus and, therefore, the fragments are emitted with momenta  $p_1$  and  $p_2$  at angles  $\theta_1$  and  $\theta_2$  in the laboratory frame. The measured angle  $\theta_m$  is determined by the neutron beam direction and by the straight line between the hits in both PPACs being, as it will be demonstrated in the next sections, quite close to the angle in the center-of-mass frame  $\theta_{cm}$ , even at large neutron energies, so that the error introduced by the momentum transfer in the angle measurement becomes negligible. Therefore, and unless explicitly indicated, the simulation results presented below were obtained by assuming a zero-momentum transfer.

### 4.3. Simulation of fission events

Geant4 tracks the propagation of the fission fragments produced by the event generator from their emission point inside the target until they leave the volume containing all the detectors and materials involved in the simulation, the “universe”, or until they are completely stopped due to the energy losses in the setup materials.

An object of the TTree class from ROOT stores all relevant data produced during the simulation in an output ROOT file. The characteristics of the fission fragments produced by the event generator are saved, including charge, mass, kinetic energy, position of the emission point in the target and outgoing angle (both in CM and laboratory frames, to take into account the linear momentum transfer). As both fragments travel through the setup, the energy losses in each material layer are also saved for each event. From the spatial position and the arrival time of the impact in those materials after generation of the fission event it is possible to determine the velocities and the trajectories of the fragments. Thus the fission fragment arrival times to the active layers of the detector are a key factor in understanding the behaviour of the PPAC detectors.

Some routines using the impact point coordinates in the cathodes were included in the code to calculate the  $\theta$  and  $\phi$  angles and obtain a more realistic comparison with the experimental results. Thus, any correlation between any pair of variables could be studied, including these calculated angles, which were also saved to the output ROOT file. These angles were calculated in two different coordinate systems: the beam-system, where the

angles are expressed in reference to the direction of the neutron beam; and the detector-system, where the angles are expressed in reference to the axis that passes through the centers of the two PPACs ( $z$  axis in Fig. 4.4). Although the angular distribution must be given in the first system, it is often easier to work in the second one, where the thickness of materials to go through is only dependent on the cosine of the angle given in this system.

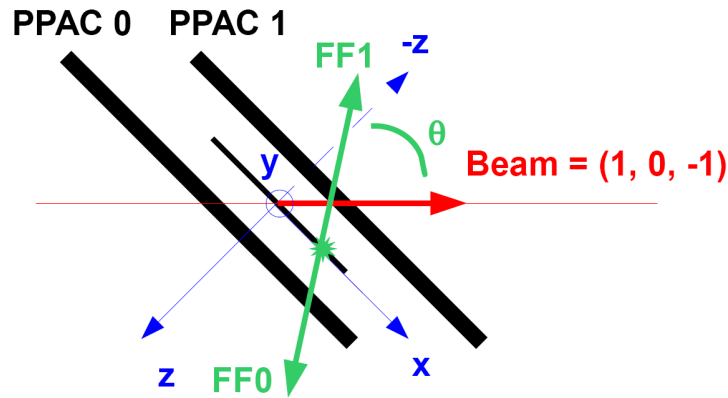


Figure 4.4: Coordinate system used in this work. The detectors and the targets are tilted  $45^\circ$  with respect to the beam direction. The origin of coordinates is at the center of the target, and the  $X$  and  $Y$  axis are parallel to the target plane (and to the plane defined by the surface of each detector). Both fission fragments ( $FF0$  and  $FF1$ ) are emitted in opposite directions at an angle  $\theta$  with respect to the beam direction. This angle  $\theta$  is the variable of physical interest to measure the angular distribution of the fission fragments.

### 4.3.1. Detected events

The most important objective of this simulation work was to evaluate the detection efficiency of the actual experimental setup and compare it with the efficiency of a configuration where detectors and targets are perpendicular to the beam direction. In both cases, the efficiency is limited by the finite geometry of the setup and by the energy losses of the fission fragments in the material layers. These layers include the target (the thickness to be crossed depends on the position of the emission point inside the target volume), the backing (which will be crossed by one of the fragments, since they are emitted in opposite directions), the gas volume between the target and the detectors and finally the three electrodes and two gas-filled gaps that conform each PPAC.

At this point we must define what can be considered a “detected event” and recall how the signals are produced in a real PPAC. Each PPAC consists of a central anode flanked by two stripped cathodes with gas-filled gaps in between. The localization signals given by both cathodes are needed to determine the spatial position of a hit. To produce a hit, the fission fragment must be able to deposit a minimum amount of energy in the two gaps to ionize the gas and generate the avalanche, which induces electric signals in the three electrodes. If we are only interested in registering the fission event without determining the position, only the anode signal is needed, requiring ionization of the gas in only one gap. This reduces the number of layers that must be traversed and increases the acceptance angle, resulting in a higher detection efficiency than that obtained when both cathode signals are required for localization.

In our simulation, the signal generation procedure was not implemented, and we assumed that the fission fragment would be detected if it deposited any energy greater than zero in both gas-filled gaps. Since we required the detection of both fission fragments, a fission event was detected and reconstructed when both fission fragments produced by the event generator deposit some energy in the two gas gaps of their respective PPACs. Events in which both fragments reach one gap of their respective PPACs were kept as fission events where the localization information was missing. Specific variables were included in the object of the TTree class to label each event according to whether it had been detected or not, and if the localization information was available.

## 4.4. Simulation results

### 4.4.1. Detection efficiency

The detection efficiency is defined as the ratio between the number of detected events and generated events, including both the geometrical efficiency and the self-absorption effects. An intrinsic efficiency of 100% was assumed for the production of the detector signals, since this process was not implemented. To obtain sufficient statistics in a reasonable computing time, a total of  $10^6$  fission events were generated for each simulation.

We will start with the simplest case, in which the PPACs and the target are perpendicular to the neutron beam direction and there is an axial symmetry around the beam axis. The distance travelled by the fission fragment inside the material layers is proportional to  $\cos\theta$ , so that the energy

loss increases with  $\cos\theta$ . Therefore, the energy loss is minimal for fission fragments crossing the detectors in the direction of the beam (perpendicular to the detector surface) and increases until the maximum polar angle of  $\theta$  is reached for the emitted fragments, which corresponds to the limits of the PPAC detector surface. However, due to the energy lost in the material, which depends on the charge, mass and initial kinetic energy of the fragment, the counting efficiency drops dramatically before reaching this limiting value of the  $\theta$  angle. There is no dependence on the azimuthal angle  $\phi$  around the axis in this process, and the  $\theta$  angle defining the geometrical acceptance also defines the angular distribution with respect to the beam direction.

Since both fission fragments must be detected, the most restrictive case occurs when the heavy fission fragment passes through the backing. Geant4 simulations for the fragments emitted by our nuclei of interest indicate the maximum angle to be around  $65^\circ$ . Fig. 4.5(a) shows the relation between  $\cos\theta$  and  $\phi$ , when the detection of both fission fragments is imposed, identifying the minimum  $\cos\theta$  value for which the fission fragments can be detected. There is no dependence on the  $\phi$  angle. The detection efficiency, defined as the ratio between the number of detected and generated fission events, is shown in Fig. 4.6 as a function of  $\cos\theta$ . The efficiency is very close to 1 for  $\cos\theta \geq 0.48$  ( $\theta \leq 61^\circ$ ) and drops quickly to zero for larger angles. This simulation was done using the fission yields for  $^{235}\text{U}(n,f)$  at thermal energies and assuming an isotropic emission.

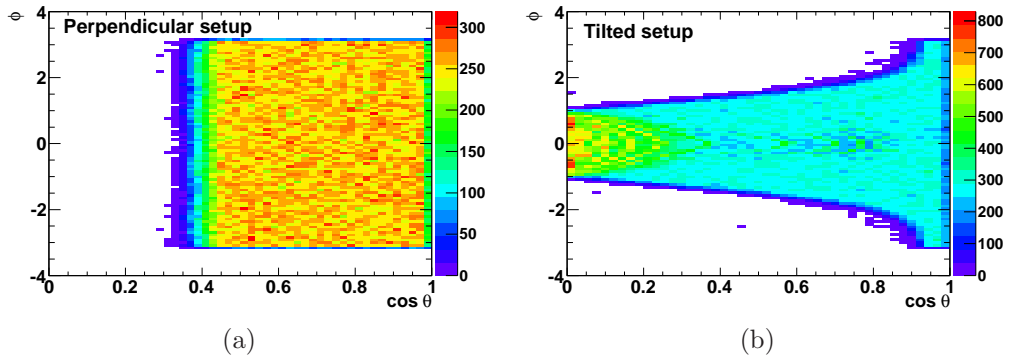


Figure 4.5: Detected events as a function of  $\cos\theta$  and  $\phi$  for both geometrical setups: In the perpendicular configuration (a), the cosine of the polar angle  $\theta$  is limited to angles below  $65^\circ$  and does not depend on the azimuthal angle  $\phi$  around the beam axis. However, in the tilted setup (b), the angular acceptance covers all the possible values of  $\theta$  but the acceptance in the azimuthal angle  $\phi$  decreases as  $\theta$  increases ( $\cos\theta$  decreases).

In the experimental setup used for the present experiment, the PPAC detectors and the targets were tilted  $45^\circ$  with respect to the beam direction. The most important advantage of such a configuration is the extended angular range that is covered for  $\cos\theta$ . There is no axial symmetry in this case, which is easily seen in Fig. 4.4. To better understand this, let us assume that the emission point is in the origin of coordinates placed in the geometrical center of the sample and the emission angle  $\theta$  is near to zero (i. e., emission within a small cone along the beam direction). In this case, all the fragments would be detected, independently of the value of the  $\phi$  angle around the beam. If  $\theta = 90^\circ$ , two extreme situations can be observed: if the fragments were emitted in the plane of this paper, they would be detected; however, if they were emitted in a direction perpendicular to this paper, they would not be detected, although the angle with respect to the beam direction is again  $\theta = 90^\circ$ . The difference between both situations is the value of the angle  $\phi$  around the axis. This is a simple way to demonstrate that, for this geometrical configuration, the efficiency depends not only on the  $\theta$  angle but also on the  $\phi$  angle. The relation between  $\cos\theta$  and  $\phi$  is represented in Fig. 4.5(b), requiring the detection of both fission fragments. In this case, all the possible values of  $\cos\theta$  between 0 and 1 are covered, but the  $\phi$  angle has a limited range that increases with  $\cos\theta$ .

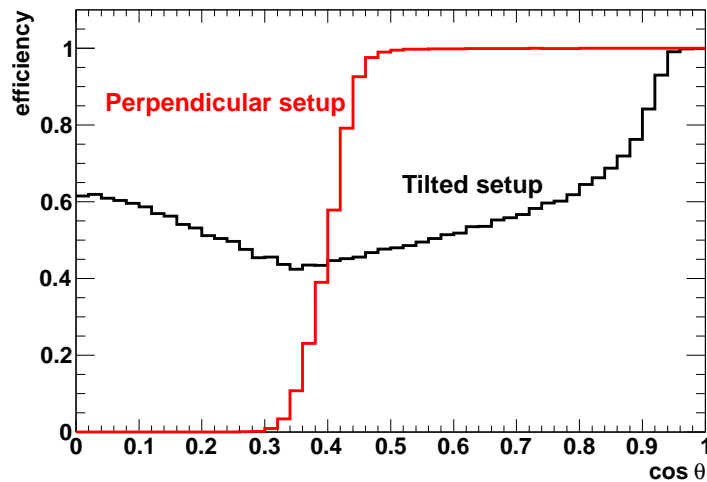


Figure 4.6: Comparison of the detection efficiency for perpendicular and tilted setups.

The efficiency as a function of  $\cos\theta$ , the variable that defines the angular distribution, is also shown in Fig. 4.6. Contrary to what happens in the perpendicular setup, the tilted setup presents a non-zero efficiency for all

values of  $\theta$ , even though this is never constant. The fact that it is possible to detect fission fragments emitted at every  $\theta$  angle converts this geometrical configuration into an excellent experimental setup for measuring fission fragment angular distributions. Despite the different behaviour of the angular acceptance in both cases, the overall detection efficiency is nearly the same for both geometrical dispositions: 0.60 and 0.59 for the perpendicular and the tilted configurations, respectively (Fig. 4.6).

#### 4.4.2. The effect of the backing thickness

In Section 2.2.3, we explained how the aluminium backings of  $^{232}\text{Th}$  samples are thinner ( $0.75\ \mu\text{m}$ ) than those of the  $^{235}\text{U}$  and  $^{238}\text{U}$  ( $2.5\ \mu\text{m}$ ) reference samples. The difference in the backing thickness will lead to a difference in the detection efficiency of the fragments emitted in the fission of both samples. The low-energy neutron-induced fission of  $^{235}\text{U}$  is isotropic, so that the experimental angular distribution obtained for  $^{235}\text{U}$  with neutron energies below 1 keV will be used to normalize the measured angular distributions of  $^{232}\text{Th}(n,f)$ .

Fig. 4.7 shows the efficiency detection obtained for the fission fragments from the  $^{235}\text{U}(n,f)$  reaction at thermal energies and with an isotropic distribution, using the two values of the backing thickness. This provides an estimate of how much the thicker backing of the  $^{235}\text{U}$  sample reduces the detection efficiency. The ratio between the efficiency curves obtained with the thicker backing and the thinner one is shown in Fig. 4.8. This ratio, using the reference efficiency of the low energy neutron-induced fission of  $^{235}\text{U}$ , must be included when normalizing the angular distributions, as explained in Chapter 5. The ratio of the measured fission cross sections  $^{235}\text{U}(n,f)/^{232}\text{Th}(n,f)$  will also be affected, having so to be corrected.

#### 4.4.3. The effect of the linear momentum transfer

To study the effect of the linear momentum transferred to the nucleus by the incident neutron, simulations have been done using several typical values of the neutron energy. The relation between the cosine of the emission angle in the CM frame,  $\theta_{cm}$ , and the cosine of the measured angle  $\theta_m$  given by the position of the hits in the two PPACs, can be seen in Fig. 4.9 for a momentum transfer of  $350\ \text{MeV}/c$ , which corresponds to the maximum momentum transfer achievable within our neutron energy range, that is reached at 1 GeV. The linear behaviour is clear, and a fit to the data indicates a slope

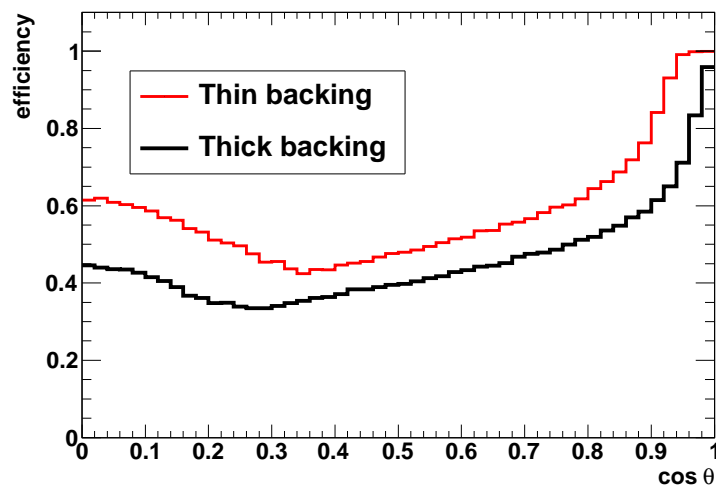


Figure 4.7: Comparison of the detection efficiency for the thinner ( $0.75 \mu\text{m}$ ) and thicker ( $2.5 \mu\text{m}$ ) aluminium backings that correspond to the real thickness of the backings for the  $^{232}\text{Th}$  and  $^{235}\text{U}$  samples, respectively.

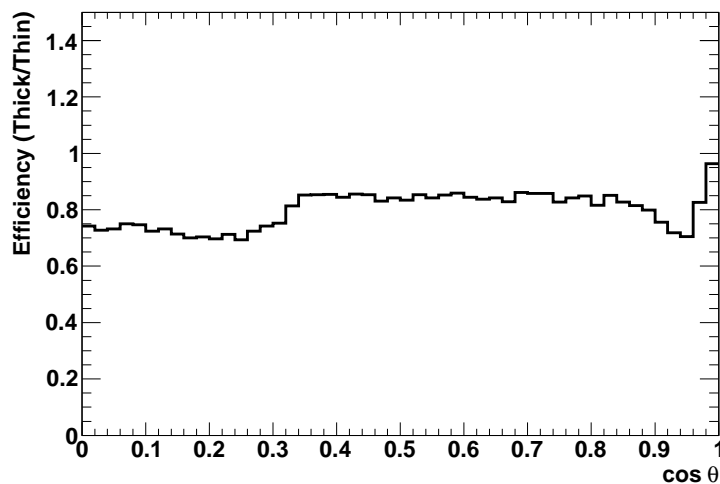


Figure 4.8: Ratio of the detection efficiencies obtained for the two backing thicknesses in Fig. 4.7.

very close to one (0.999), what means that the difference between the cosine of the measured and the cosine of the CM angles is less than 0.1%. The same procedure was repeated for some values of the transferred momentum (from 0 up to  $350 \text{ MeV}/c$ , in  $50 \text{ MeV}/c$  steps) and this variation was found to be less than 0.1% in all the cases. This value is smaller than the angular resolution of the experimental setup. The strips of the cathodes are 2 mm

wide, so that an uncertainty of  $\pm 2$  mm in the horizontal and vertical positions would lead to an uncertainty in the cosine of the angle of each fission fragment of about 4% for the larger values of  $\theta$ , being lower for the smaller ones. However, the delay line does an integration over the strips and, using time differences, provides the spatial position with a much better resolution than the strip width.

In any case, one can conclude that, due to the geometrical characteristics of this setup, the variation introduced by the momentum transfer is negligible compared to the uncertainty in the measured angle.

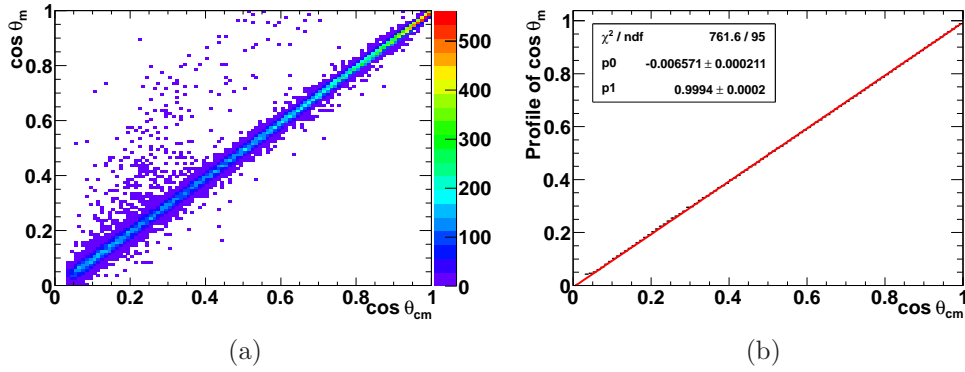


Figure 4.9: Relation between the measured angle  $\cos \theta_m$  and the emission angle in center-of-mass frame  $\cos \theta_{cm}$  as given by the simulation for a momentum transfer of  $350 \text{ MeV}/c$ , corresponding to a neutron energy around  $1 \text{ GeV}$ . The histogram is fit to a straight line in (b).

#### 4.4.4. Relation between the time difference and the emission angle

One important observable is the time difference between the signals in the anodes of both PPACs. We have already mentioned that the coincidence in anode times is the signature of a fission event. By representing this time difference (for the tilted setup) against the cosine of the angle measured in the detector reference system, it is possible to separate the events according to the fragment that is passing through the backing (Fig. 4.10). The distribution is not centered at zero time because the backing introduces an additional layer of material that slows down only one of the fragments. Since the stopping power increases with  $Z^2$  (which is included in the Bethe-Bloch formula), when the heavy fission fragment passes through the backing, the time needed

for this fragment to reach the anode is greater. The time increases with the distance travelled, which is inversely proportional to the cosine of the angle. The accumulation of negative values in Fig. 4.10 corresponds to this scenario. If the light fission fragment goes through the backing, this effect is less dramatic and tends to make the time difference equal to zero (see the accumulation around time difference equal to zero in the same figure).

Thanks to the presence of the backing and the time resolution of the PPACs it is possible to distinguish the existence of a significant mass difference between the complementary fission fragments using this experimental setup and, therefore, we could investigate the contributions of symmetric and asymmetric mass division in the fission process at the different neutron energies, as it will be developed in Chapter 5.

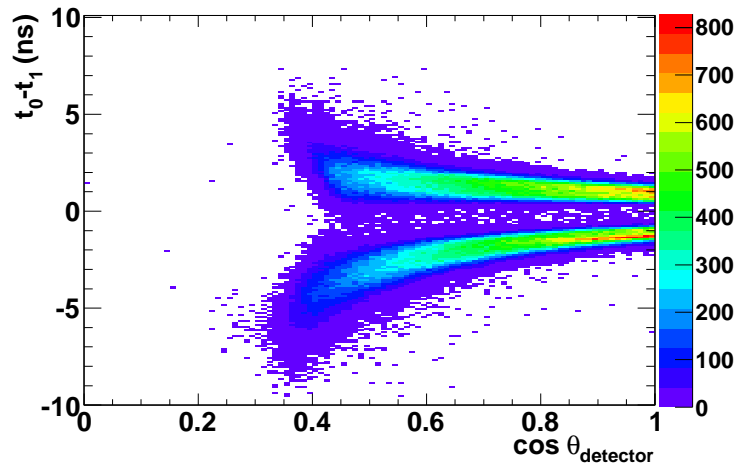


Figure 4.10: Simulated fission fragment time difference at the anodes in the tilted setup as a function of the angle cosine measured in the detector reference system for the asymmetric fission of  $^{235}\text{U}$  at low energies. The two possible cases with the heavy or the light fission fragment crossing the backing are clearly distinguished.



# Chapter 5

## Results on $^{232}\text{Th}(\text{n},\text{f})$

The procedure for obtaining the fission fragment angular distribution (FFAD) of  $^{232}\text{Th}(\text{n},\text{f})$  is described in this chapter. The results on the anisotropy parameter that characterize the angular distribution as a function of the neutron energy, from fission threshold up to 1 GeV, are then discussed and compared with previous experimental data.

The neutron-induced fission cross section of  $^{232}\text{Th}$  by using the  $^{235}\text{U}(\text{n},\text{f})$  cross section as reference was also obtained for the entire energy range, normalizing it to the ENDF/B-VII.1 evaluation. The detection efficiency correction takes into account the angular distribution of the emitted fragments, and its effect on the cross-section is here discussed. The obtained value for the  $^{232}\text{Th}(\text{n},\text{f})$  cross section is compared with results from other experiments and with different evaluations.

Finally, the bimodal behaviour with the neutron energy of the fission process is described. The time difference between the detection of the two fragments allowed us to determine whether the fission occurs in the symmetric or the asymmetric mode.

### 5.1. Fission fragment angular distribution

The number of fission events emitting fission fragments in a direction at an angle  $\theta$  with respect to the beam direction is given by:

$$W(E, \theta) = \Phi(E) \cdot N \cdot \frac{d\sigma(E, \theta)}{d\Omega} \quad (5.1)$$

where  $\Phi(E)$  is the time-integrated neutron fluence (measured in  $n \cdot \text{cm}^{-2} \cdot \text{MeV}^{-1}$ ) for the full measuring time,  $N$  is the number of atoms in the tar-

get, and  $d\sigma(E, \theta)/d\Omega$  is the differential cross section for emission of fission fragments at an angle  $\theta$ .

The number of detected fragments is given by multiplying this expression by an efficiency factor,  $\epsilon$ , which for a given fragment depends on the distance travelled through the setup layers. This distance will depend on the outgoing angles  $\theta$  and  $\phi$ , so that:

$$W(E, \theta)_{\text{detected}} = \Phi(E) \cdot N \cdot \frac{d\sigma(E, \theta)}{d\Omega} \cdot \epsilon(\theta, \phi) \quad (5.2)$$

### 5.1.1. Experimental FFAD in $^{232}\text{Th}(n,f)$

The fission fragment angular distribution (FFAD) is defined with respect to the cosine of the angle between the beam axis and the direction of the fission fragments, assumed to be emitted back to back. This direction is obtained from the spatial positions of the two fission fragments detected in both PPACs (see Chapter 3). As it was demonstrated in Chapter 4, the effect in the emission angle of the linear momentum transferred by the impinging neutron is negligible even at the highest energies, and henceforth the measured value is taken as the angle given in the center-of-mass frame.

In order to obtain the FFAD for each neutron energy, the energy binning must be taken as narrow as possible while keeping enough statistics for studying the angular dependence. In order to have around 2000 counts per energy bin, we chose a logarithmic binning where the bin width was different for each logarithmic decade. These energy bins were larger than the energy resolution given by the n\_TOF facility and, for the sake of simplicity, the energy corresponding to every event inside a bin was taken as its central value.

For each energy interval, the distribution of the number of fission events as a function of  $\cos \theta$ , from 0 to 1, was obtained. To analyse the FFAD, we divided each one of these distributions into 15 bins of  $\cos \theta$ , which represents a trade-off between the resolution and the statistical uncertainty of the number of counts for the most unfavourable cases of  $^{232}\text{Th}(n,f)$ .

When trying to study the angular behaviour of the  $^{232}\text{Th}(n,f)$  reaction, one needs to accurately know the efficiency factor  $\epsilon(\theta, \phi)$  introduced in Eq. (5.2). For this purpose we used our  $^{235}\text{U}$  data, obtained in the same conditions as the  $^{232}\text{Th}$  ones. As  $^{235}\text{U}(n,f)$  below 1 keV is known to be isotropic, the detection efficiency can be directly obtained from this distribution. The experimental distribution obtained with the neutron-induced fission of  $^{235}\text{U}$  below 1 keV is shown in Fig 5.1, along with the results obtained from a

Geant4 simulation (see explanation in Chapter 4, Fig. 4.6) after normalizing to the experimental total number of counts. A good agreement was found between the experimental and simulated results. It can be seen that this distribution, even coming from an isotropic distribution, is not flat at all because the efficiency is dependent on  $\cos\theta$ . The angular distributions of  $^{232}\text{Th}(n,f)$  were so divided by the  $^{235}\text{U}$  experimental one at low energy in order to correct them for the detection efficiency.

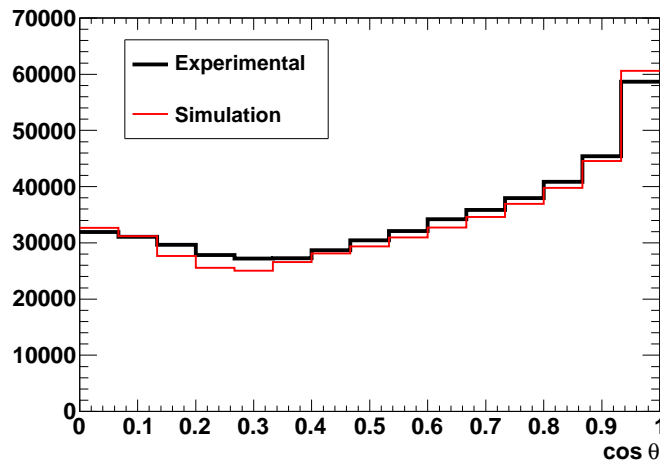


Figure 5.1: Experimental cosine distribution of  $^{235}\text{U}(n,f)$  for  $E_n < 1\text{ keV}$ , compared with that of the Geant4 simulation.

The resulting cosine distributions were parametrized by a sum of Legendre polynomials  $P_L(\cos\theta)$ :

$$W(\theta) = \sum_{L=0}^{L_{max}} a_L P_L(\cos\theta) \quad (5.3)$$

where  $L$  is the order of the polynomial and  $a_L$  are the fitting coefficients. In our physical case, only even terms in  $\cos\theta$  were taken into account because of the backward-forward symmetry of the emitted fragments. Appendix A provides a brief summary of the Legendre polynomials and their properties.

The zero-order polynomial is a constant,  $P_0(\cos\theta)=1$ , and restricting to even terms, the least-squares fit of the angular distribution for each neutron energy interval has been performed using the following Legendre polynomial series:

$$W(\theta) = A_0 \left[ 1 + \sum_{\substack{L=2 \\ L \text{ even}}}^{L_{max}} A_L P_L(\cos \theta) \right] \quad (5.4)$$

The choice of the best suited value of  $L_{max}$  will be discussed later. Two examples of the normalized angular distributions are shown in Fig. 5.2, where (a) corresponds to a case where the preferred emission was in the beam direction and (b) shows a side peaked distribution with a maximum at  $45^\circ$  and a minimum at  $0^\circ$ . The error bars represent the statistical uncertainty. The fact of having the explicit constant factor  $A_0$  in Eq. (5.4), allow us to normalize the experimental values at  $90^\circ$  so that the different distributions can be compared more easily. In both cases, fits to the  $2^{nd}$ ,  $4^{th}$ , and  $6^{th}$  order polynomials are also drawn showing that at least the  $4^{th}$  order must be included in the fit to obtain good results.

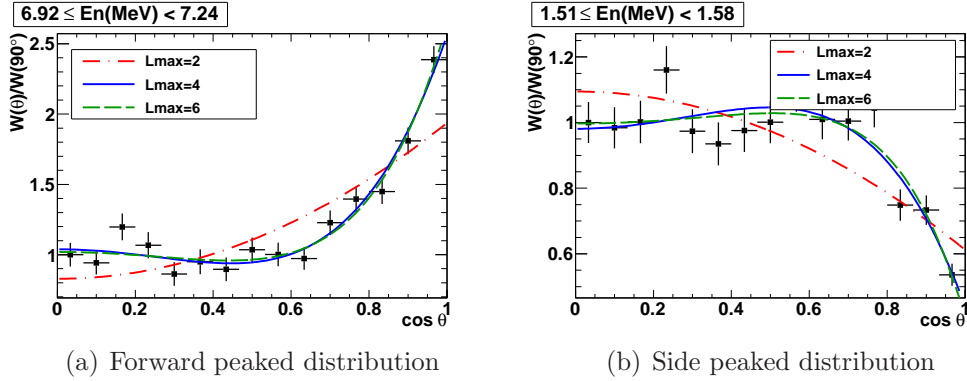


Figure 5.2: Examples of angular distributions of fragments emitted in  $^{232}\text{Th}(n,f)$  reaction. Fig. (a) corresponds to a forward peaked distribution, where most of the fragments are emitted in the beam direction; whereas in Fig. (b), the maximum of the emitted fragments is located at around  $45^\circ$  and the minimum is found in the beam direction. In both cases, fits to the  $2^{nd}$ ,  $4^{th}$ , and  $6^{th}$  order are drawn. The error bars represent statistical uncertainties.

ROOT was used to find the  $L_{max}$  that provides the best fit for each case by minimizing the value  $(\chi_\nu^2 - 1)$  for  $L_{max} = 2, 4$  and  $6$ , being  $\chi_\nu^2 \equiv \chi^2/\nu$ , where  $\nu$  is the number of degrees of freedom, equal to the number of data points minus the number of parameters of the function. The calculated values of  $\chi_\nu^2$  corresponding to the different values of  $L_{max}$  are shown in Fig. 5.3(a) for each energy bin.

The contribution of the  $A_2$ ,  $A_4$  and  $A_6$  coefficients of the best fits corresponding to each value of the neutron energy is shown in Fig. 5.3(b). From

both graphics it can be seen that a fit restricted to the  $2^{nd}$ -order polynomial is not enough to reproduce the dependence of the fission fragment angular distribution with the angle. At least, the  $4^{th}$  order is always needed, while the  $6^{th}$  order coefficient is only different from zero in a few energy intervals.

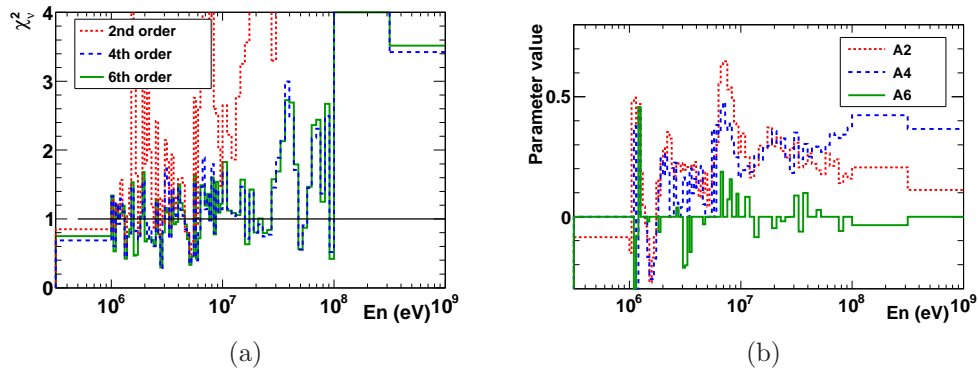


Figure 5.3: The  $\chi_v^2$  value for fits to Legendre polynomial series with  $L_{max} = 2, 4$  and  $6$  are shown in (a). The  $A_2, A_4$  and  $A_6$  coefficients for the best fit in each energy bin are given in (b).

The entire set of normalized angular distributions of the fragments emitted in  $^{232}\text{Th}(n,f)$ , as well as the best fit in each case, can be found in Appendix C for all the energies between fission threshold and 1 GeV.

In Fig. 5.4, tridimensional histograms of the fits for each energy interval are shown as a function of the emission angle  $\theta$ . It is important to notice that each curve has a different shape, with maxima and minima in some cases, being the most striking around the first and the second chance thresholds ( $\sim 1$  MeV and  $\sim 7$  MeV, respectively). This behaviour reinforces the idea that a measurement covering all the possible values of the emission angle, like presented in this work, is needed to characterize the angular distribution of the fragments, that is required for a precise determination of the (n,f) cross sections.

As the fits of the fission fragment angular distribution of  $^{232}\text{Th}$  were normalized to  $90^\circ$ , the projection of this plot on the energy axis, at  $\theta = 0^\circ$ , represents what is known as the anisotropy parameter. A discussion on this parameter will be given in the next section.

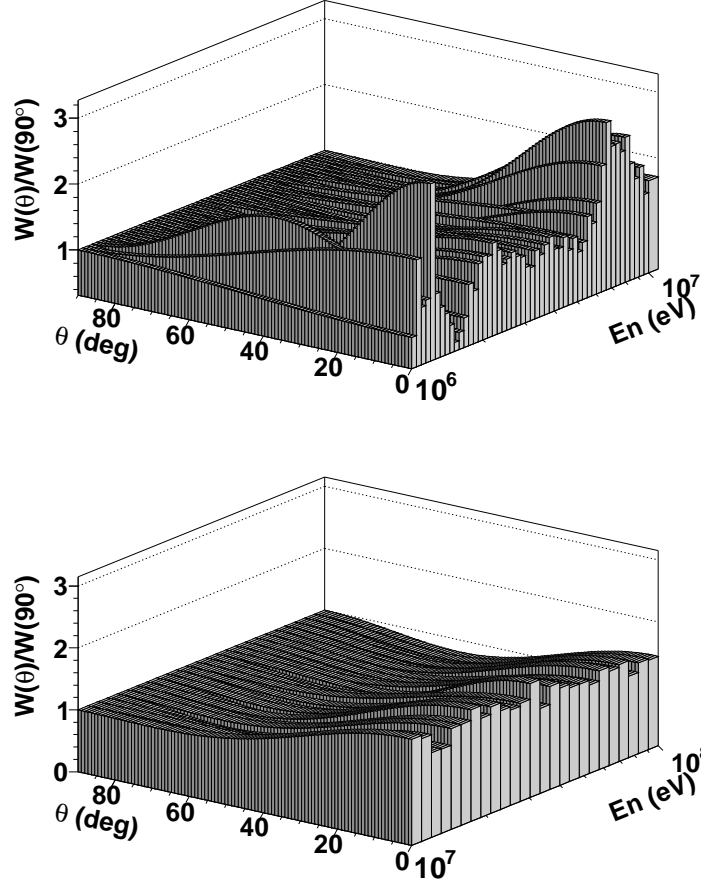


Figure 5.4: Fits of the fission fragment angular distribution of  $^{232}\text{Th}(n,f)$ , normalized at  $\theta = 90^\circ$ , as a function of the emission angle  $\theta$  for each neutron energy interval.

### 5.1.2. The anisotropy parameter

The anisotropy parameter is customary used to characterize the behaviour of the angular distribution with the neutron energy. It is defined as:

$$A = \frac{W(0^\circ)}{W(90^\circ)} \quad (5.5)$$

where  $W(0^\circ)$  and  $W(90^\circ)$  represent the number of fission fragments emitted at  $0^\circ$  and at  $90^\circ$  with respect to the neutron beam direction. By inserting Eq. (5.4) in this expression, and evaluating the different Legendre polynomials, given in Table A.1, at  $0^\circ$  and at  $90^\circ$ , the following analytical expression for

the anisotropy parameter is obtained:

$$A = \frac{W(0^\circ)}{W(90^\circ)} = \frac{1 + A_2 + A_4 + A_6 + \dots}{1 - \frac{1}{2}A_2 + \frac{3}{8}A_4 - \frac{5}{16}A_6 + \dots} \quad (5.6)$$

This expression shows how the anisotropy parameter depends only on the coefficients  $A_2$ ,  $A_4$ , and  $A_6$ , given by the fits to the cosine distributions described in the previous section. This equation works for any  $L_{max}$  simply by making equal to zero the coefficients  $A_L$  of higher order than  $L_{max}$ .

The anisotropy parameter itself only provides information on the ratio of the number of fragments emitted at  $0^\circ$  and  $90^\circ$ , while the behaviour at intermediate angles remains hidden, as it was shown in Fig. 5.4. An exception occurs for those cases where fitting with  $L_{max} = 2$  produces a  $\chi^2_\nu$  close to 1 because, in this case, only one parameter is needed to describe the shape of the distribution, since  $A_0$  is a global constant.

Despite this limitation, the anisotropy parameter is useful to find at what neutron energies the angular distribution is not isotropic: an anisotropy parameter equal to one does not imply isotropy, but a value different from one implies an anisotropic behaviour. This will be shown in Section 5.1.4, where the anisotropy parameter obtained with an experimental setup of perpendicular PPACs will be described.

The anisotropy parameter calculated from the previous fits for the  $^{232}\text{Th}(n,f)$  reaction is shown in Fig. 5.5, from fission threshold up to 1 GeV. This is the first anisotropy measurement ever done covering such a broad energy range. The uncertainty bars correspond to the propagation in Eq. (5.6) of the parameter uncertainties given by the fits shown in Appendix C. The fission cross section given by the ENDF/B-VII.1 evaluation [13] is also drawn to show the existing relationship between the peaked structure of the anisotropy and the multiple chance fission; the arrows indicate the threshold energies of the first, second and third-chance fission channels, according to Fig. 1.8. Large variations of the anisotropy appear at these energies because only a few states (with well-defined angular momentum) are available above the fission barrier, as was explained in Section 1.6.

### 5.1.3. Discussion on the FFAD results

Despite the relevance of the neutron-induced fission of  $^{232}\text{Th}$  for the nuclear fuel cycle, only a few measurements on the angular distribution of the emitted fragments have been done to date, as it can be seen in Fig. 5.6 where they are compared to the present data.

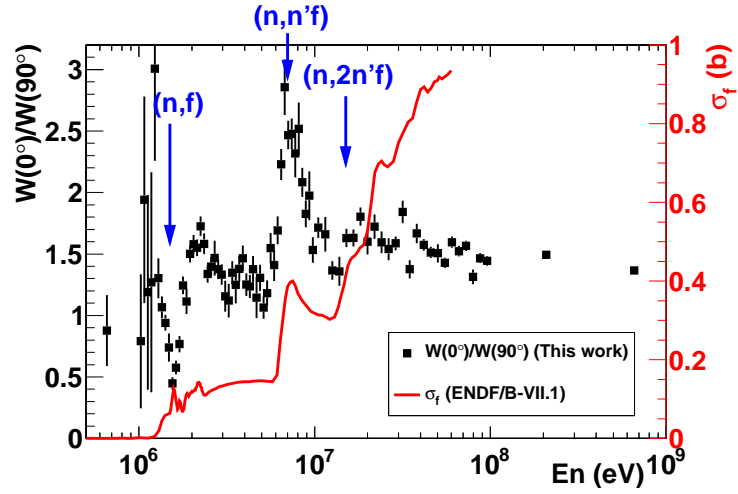


Figure 5.5: Dependence of the anisotropy parameter on the neutron energy in the  $^{232}\text{Th}(n,f)$  reaction. The fission cross section of  $^{232}\text{Th}$  given by the ENDF/B-VII.1 evaluation [13] is drawn to show how the peaked structure exhibited by the anisotropy is related to the existence of different multiple-chance fission channels (indicated by the arrows, according to Ref. [63]).

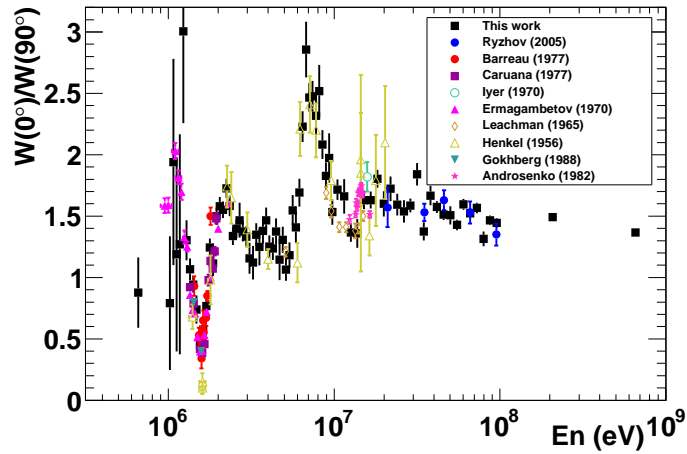


Figure 5.6: Dependence of the anisotropy parameter on the neutron energy in the  $^{232}\text{Th}(n,f)$  reaction are given by the black markers, compared with previous results from other authors [64, 74, 120–126].

It can be seen that most of the available data cover the energy range between 1 and 2 MeV [74, 120–123], where there is a marked minimum in the anisotropy around the first-chance fission threshold. In this range, our

data had enough statistics to allow for a fine enough energy binning accurately reproducing the expected behaviour: a maximum of the anisotropy at the fission threshold and a deep minimum at somewhat larger energies, indicating a situation where the preferred emission of the fragments is side-peaked. Above these energies, another maximum follows this minimum. This behaviour is pointing to the existence of vibrational resonances around the fission threshold.

Above the first-chance fission threshold, the up-to-date experimental data are scarce and having large uncertainties [74, 124–126].

Big variations of the anisotropy can be also seen at the onsets of the second-chance ( $\sim 7$  MeV) and third-chance ( $\sim 15$  MeV) fission. The identification of a well-defined minimum at 13 MeV in our data is remarkable since several measurements [74, 120, 127, 128] had previously been done in this energy region, but their large uncertainties and their poor energy resolution did not allow for a clear identification of the third-chance fission threshold.

The data obtained here improve the current situation by providing results in a continuous energy range up to 1 GeV. The only formerly measurement done above 20 MeV and up to 100 MeV [64] claimed for a value of the anisotropy parameter significantly higher than 1. Our data confirm such a result but improving the energy resolution and showing, for the first time, an anisotropy parameter greater than 1 in all the range up to 1 GeV. Therefore, fission of  $^{232}\text{Th}$  at those neutron energies is not isotropic.

Our experimental setup presents better capabilities than most of the used for the previous measurements. The use of a continuous energy neutron beam makes possible to study the energy dependence with high resolution, only limited by the available statistics. In addition, the position-sensitive PPACs employed in the present work allow to measure over all the possible values of the emission angle so that the full angular distribution is measured and fitted to a Legendre polynomial from which the anisotropy parameter is obtained. This situation is not achieved by most of the previous results shown in Fig. 5.6, where the angle measurement is affected by the size of the detector, worsening the angular resolution.

This impose constraints in the anisotropy parameter calculation: for instance, Leachman et al. [124] measured the fragments emitted only at 6 values of the angle and calculated the anisotropy as the ratio of counts detected at  $0^\circ$  and at  $90^\circ$ , with an uncertainty of  $8.8^\circ$  in the angle measurement. Henkel et al. [74] measured fragments emitted at only five different angles between  $0^\circ$  and  $90^\circ$  and fitted the angular distributions to a series of even Legendre polynomial including terms up to  $6^{\text{th}}$ -order to calculate the

anisotropy. A similar procedure was used by Caruana et al. [122], with a fit up to 4<sup>th</sup>-order Legendre polynomial.

Position-sensitive gas detectors were used by Ryzhov et al. [64], allowing a better angular resolution with respect to the above mentioned works. The anisotropy was calculated, in this case, from a fit to a  $\cos^2\theta$  function, giving the only previous results up to 100 MeV.

#### 5.1.4. Comparison with a perpendicular PPAC setup

Throughout this thesis work, the advantages of the tilted-planes setup used in this experiment to measure angular distributions of fission fragments have been presented. The quality of the obtained results represents the best demonstration of its suitability. However, for the sake of completeness, it is worthwhile to take a glance to the results provided by the same PPAC detectors placed in a perpendicular configuration, as they were used at n\_TOF in those former campaigns where fission cross sections of several nuclei [3, 4], including  $^{232}\text{Th}$ , were measured.

##### Fission fragment angular distribution

As it was discussed in Chapter 4, the angular acceptance when using the perpendicular-planes setup was limited to emission angles below  $\sim 60^\circ$  (that means,  $\cos\theta \geq 0.5$ ). Moreover, in the particular case of that experiment, thresholds on cathode signals were unhappily set to too high values reducing even more the acceptance, so that only fragments emitted at a  $\theta$  angle below  $\sim 45^\circ$  ( $\cos\theta \geq 0.7$ ) were detected. The direct consequence of this limitation of the angular acceptance is that high-order Legendre polynomials cannot be used to fit those experimental data and, therefore, only 2<sup>nd</sup>-order polynomials were used [129]. Two examples of the experimental cosine distributions and their fits can be seen in Fig. 5.7 (compare it with Fig. 5.2).

The extrapolation up to  $90^\circ$  of the fitted function provided a rough estimate of the anisotropy parameter  $A = W(0^\circ)/W(90^\circ)$ , which is represented in Fig. 5.8 together with those previous results already shown in Fig. 5.6. It is evident that the obtained values for the anisotropy parameter do not agree with the available data. The reason of such a discrepancy is the reduced angular range available, do not allowing us to fit the angular distributions to polynomials of an order higher than 2. However, it can be seen that the behaviour of the anisotropy parameter with the neutron energy is qualitatively reproduced, as its largest variations occur at the multiple-chance fission thresholds, as in Fig. 5.6.

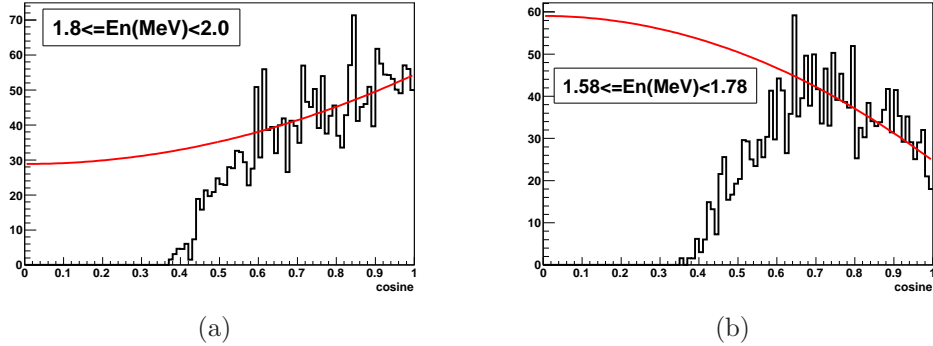


Figure 5.7: Examples of angular distributions of fragments emitted in  $^{232}\text{Th}(n,f)$  measured with a setup of PPACs perpendicularly placed to the beam direction. A forward-peaked (a) and a side-peaked (b) distribution are shown. The curves are fits to a  $2^{\text{nd}}$ -order Legendre polynomial. (From Ref. [129].)

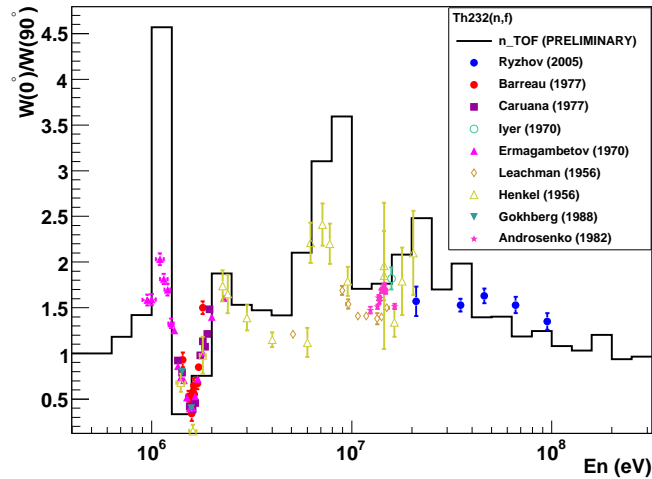


Figure 5.8: Anisotropy parameter obtained for the  $^{232}\text{Th}(n,f)$  reaction using a setup where PPACs were perpendicularly placed to the neutron beam. Previous results from other authors are shown, as it was done in Fig. 5.6. (From Ref. [129]).

In light of the above results, the ratio  $W(0^\circ)/W(45^\circ)$  was calculated from the same fits, providing results that are still useful to examine the behaviour of the anisotropy, even though only  $2^{\text{nd}}$ -order polynomials could be used. The results for several nuclei are shown in Fig. 5.9.

Several common features can be seen. First is the noticeable difference

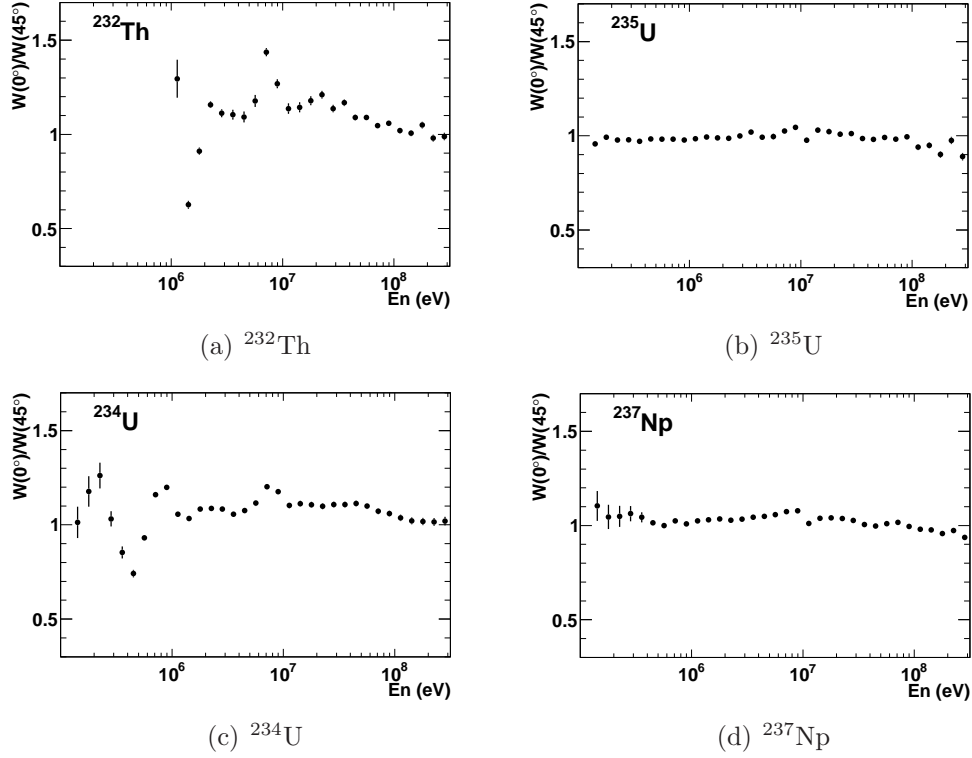


Figure 5.9: Calculated ratio  $W(0^\circ)/W(45^\circ)$  for the fission of different nuclei using the setup with perpendicular PPACs. The error bars represent only the statistical uncertainties.

between even and odd isotopes. In the case of  $^{232}\text{Th}$  (Fig. 5.9(a)) and  $^{234}\text{U}$  (Fig. 5.9(c)), both even-even nuclei, a deep minimum appears at the fission threshold. The large variations of their angular distributions at this energy are attributed to a 0 spin in the ground state, so that fission happens through a few states of well-defined angular momentum, given by the orbital angular momentum of the neutron  $l$ , as it was explained in Section 1.6. On the other hand,  $^{235}\text{U}$  and  $^{237}\text{Np}$  (Figs. 5.9(b) and 5.9(d)) are thermally fissionable so that there is no first-chance threshold. That is why the peak in the anisotropy is much smaller at this energy than for the even-even nuclei. In addition, the small variations on the angular distribution along all the energy range are due to their high spin (7/2 and 5/2, respectively) allowing the compound nucleus to undergo fission from a number of states of different angular momentum, even if the neutron has  $l = 0$ , so that the observed behaviour is a superposition of many different angular distributions that results in an almost isotropic angular function. The second fact to bring out is that

the second-chance threshold appears always around 7 MeV independently whether the first-chance threshold exists or not.

On the other hand, high-energy neutrons present large values of  $l$ , so that fission can take place through a number of states of different angular momentum, with independence of the spin of the nucleus. Therefore, fission of any nucleus becomes more isotropic as the neutron energy increases.

### Fission cross-sections

Previous experiments done at n\_TOF with this experimental setup provided accurate measurements on the fission cross section of several nuclei. However, as the anisotropy values there obtained were not accurate enough, results from other authors were needed to properly correct the cross-section results by the detection efficiency. Conversely, with the tilted setup used in the present experiment, the angular distribution of the emitted fragments and the fission cross section can be measured simultaneously for both the target under study and the reference one, so that the efficiency factor due to the limited angular acceptance can be precisely taken into account. In the following sections, the procedure to extract the fission cross section is described.

## 5.2. Fission cross section measurement

In the present experiment, the fission cross section of the  $^{232}\text{Th}(n,f)$  reaction has been measured using the  $^{235}\text{U}$  sample as reference, as described in Chapter 2 when dealing with the experimental setup. The number of detected fission events (per unit of incident energy) induced by neutrons in a target during the full measuring time is:

$$C(E) = \Phi(E) \cdot N \cdot \sigma(E) \cdot \epsilon(E) \quad (5.7)$$

where  $\Phi(E)$  is the time-integrated neutron fluence (in  $n \cdot \text{cm}^{-2} \cdot \text{MeV}^{-1}$ ),  $N$  is the total number of atoms in the sample,  $\sigma(E)$  is the fission cross section and  $\epsilon(E)$  is the detection efficiency.

MCNP simulations [110] have demonstrated that the neutron flux attenuation in the entire experimental setup, including targets, backings, detectors and kapton windows, is less than 1%. Therefore, the neutron flux ratio between two targets can be assumed to be equal to one, and the ratio of the

fission cross-sections becomes independent of the neutron flux intensity:

$$\frac{\sigma_i(E)}{\sigma_j(E)} = \frac{C_i(E)}{C_j(E)} \cdot \frac{N_j}{N_i} \cdot \frac{\epsilon_j(E)}{\epsilon_i(E)} \quad (5.8)$$

where the target labelled as  $j$  is the reference target ( $^{235}\text{U}$  in our case) for which the fission cross section is assumed to be accurately known. The number of detected fission events for  $^{235}\text{U}$  and for one target of  $^{232}\text{Th}$  are shown in Fig. 5.10.

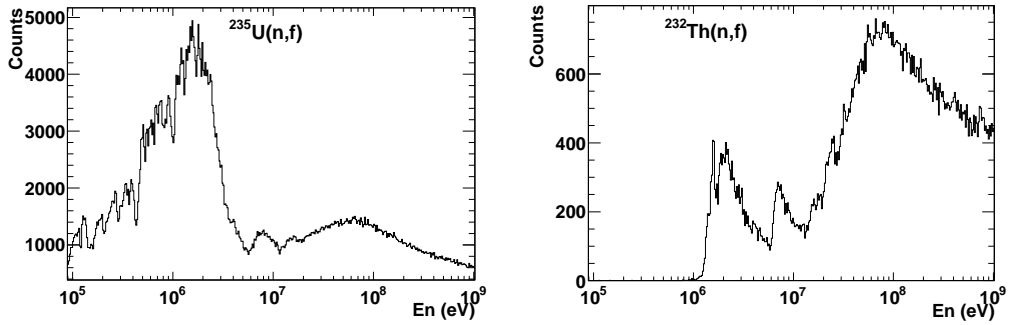


Figure 5.10: Fission rates for  $^{235}\text{U}$  and  $^{232}\text{Th}$  samples.

### 5.2.1. Detection efficiency

A deep analysis of detection efficiency is an important issue for cross section measurements. The coincident detection of both fission fragments that is required to unambiguously identify the fission events affects the detection efficiency, because the fragments must pass through material layers before reaching the active part of the detector. In order to maximize detection efficiency, only detection in the anodes was required, which occurs before the fission fragments have to pass through the extra material layers needed for measuring their trajectory. With this procedure, the detection efficiency was increased from 59% when the localization signals were required to 64%. Both values were calculated with the Geant4 simulations explained in Chapter 4.

The quantity of interest in Eq. (5.8) is the ratio between the efficiencies of the reference and of the studied samples. Because the geometry and the materials are approximately the same for all the targets, the detection efficiency is nearly equal for all of them, except for the contribution from the thicker aluminium backing of the  $^{235}\text{U}$  reference sample with respect to the  $^{232}\text{Th}$  ones. Thus, an absolute value of the detection efficiency is not needed

for each sample and the ratio of detection efficiencies can be considered as unity plus a number of small deviations:

$$\frac{\epsilon_j(E)}{\epsilon_i(E)} = 1 + \delta_{thick} + \delta_{inh} + \delta_{thresh} + \delta_{W(E)} \quad (5.9)$$

These deviations are due to differences in the thicknesses of the backing and the detectors ( $\delta_{thick}$ ), the mass distribution throughout the samples ( $\delta_{inh}$ ), the different detection thresholds ( $\delta_{thresh}$ ) of the detectors and the angular distribution  $\delta_{W(E)}$  of the emitted fragments, which is different for each isotope and depends on the energy. This angular distribution effect cancels out when counting-rates from samples of the same isotope are compared, making so possible to estimate the effect of the other contributions. The fission yield of each of the six  $^{232}\text{Th}$  samples was divided by the average fission yield of the other five samples, and the results are presented in Fig. 5.11. As it will be explained in Section 5.2.3, fission rates are normalized to the integral value between 3 and 5 MeV of the evaluated fission cross section ratio  $^{232}\text{Th}(n,f)/^{235}\text{U}(n,f)$  given by the ENDF/B-VII.1 evaluation because, to date, there is no a precise measurement for the mass of the  $^{232}\text{Th}$  targets.

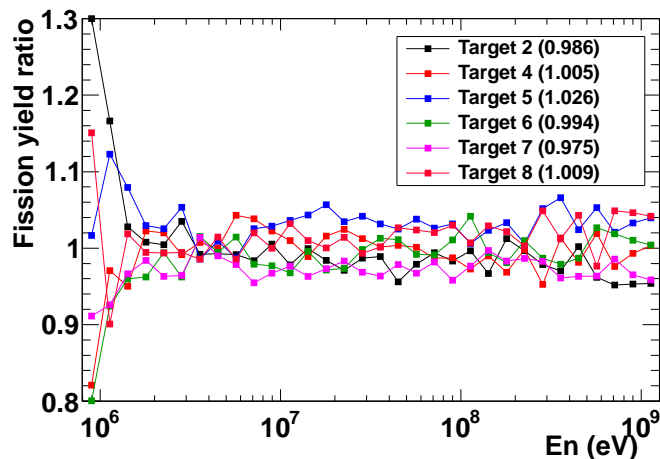


Figure 5.11: Fission yield ratios between each sample of  $^{232}\text{Th}$  over the average value of the other ones. The mean values of these ratios are indicated inside the legend box for the six targets.

The observed result was nearly constant and therefore energy-independent, being the observed  $\pm 5\%$  spread due to the statistical fluctuations of the fission yields. The mean values of these ratios, calculated above 5 MeV to avoid the normalization region, are indicated inside the legend box for the

six targets. The largest values are  $-2.6\%$  for target number 5, and  $+2.5\%$  for target 7, and include the contributions from  $\delta_{thick}$ ,  $\delta_{inh}$  and  $\delta_{thresh}$ .

### 5.2.2. Anisotropy correction in $^{232}\text{Th}(\text{n},\text{f})$ cross section

All along this work, reference has been made to how the angular distribution of the fission fragments depends on the incident neutron energy and how each nucleus displays a different behaviour. The fission process is isotropic at low neutron energies, but becomes anisotropic at higher energies, presenting large variations at the multiple-chance fission thresholds. The angular acceptance of the PPAC setup is not  $4\pi$ ; therefore, the differences in the angular distributions of the involved nuclei must be taken into account when correcting the missing solid angle in the fission cross section ratios.

In the present work, the FFAD was calculated for  $^{232}\text{Th}$  and  $^{235}\text{U}$ . The detection efficiency for a target at a given energy, related to the angular distribution of the fragments and to the limited angular acceptance, is:

$$f_{\theta} = \frac{\int_0^1 W(\theta) \cdot \epsilon(\theta) \cdot d(\cos \theta)}{\int_0^1 W(\theta) \cdot d(\cos \theta)} \quad (5.10)$$

where  $W(\theta)$  is the angular distribution for the nucleus at the given energy, and  $\epsilon(\theta)$  is the geometrical efficiency of the detection setup, which depends on the emission angle  $\theta$ .

The  $f_{\theta}(^{235}\text{U})/f_{\theta}(^{232}\text{Th})$  ratio is shown in Fig. 5.12 and it had to be included in Eq. (5.9). The factor was close to unity in the entire energy range, with variations not larger than  $6\%$  appearing at the first-chance and second-chance fission thresholds for  $^{232}\text{Th}$ , where the largest variations in the anisotropy are found.

### 5.2.3. Fission cross section ratio $^{232}\text{Th}/^{235}\text{U}$

The central issue of the n\_TOF PPAC experiments was to accurately measure ratios of neutron-induced fission cross sections, without depending on the knowledge of the neutron flux, which according to Eq. (5.8) cancels out due to the negligible attenuation of the neutron beam intensity as it passes through the whole reaction chamber.

In the experiment of this work, it has been possible to measure the fission cross section ratio  $^{232}\text{Th}(\text{n},\text{f})/^{235}\text{U}(\text{n},\text{f})$  from fission threshold up to 1 GeV neutron energy, but due to the lack of a precise measurement of the masses

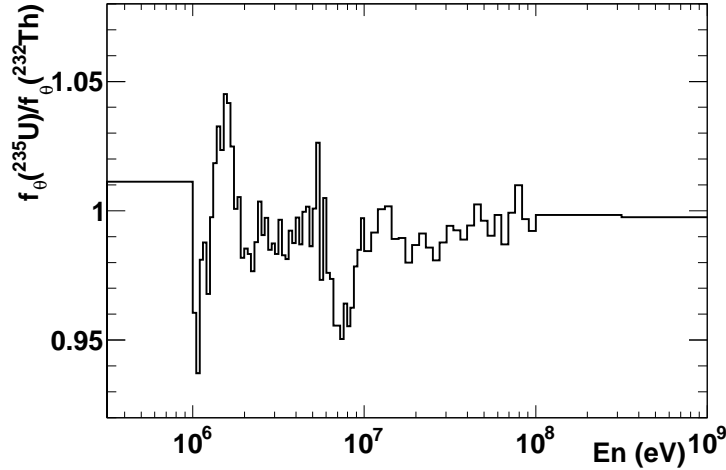


Figure 5.12: Dependence of the  $f_{\theta}(^{235}\text{U})/f_{\theta}(^{232}\text{Th})$  ratio on the neutron energy. The largest deviations from unity appear at the first- and second-chance fission thresholds of  $^{232}\text{Th}$ , where this nucleus has the largest variations in the anisotropy.

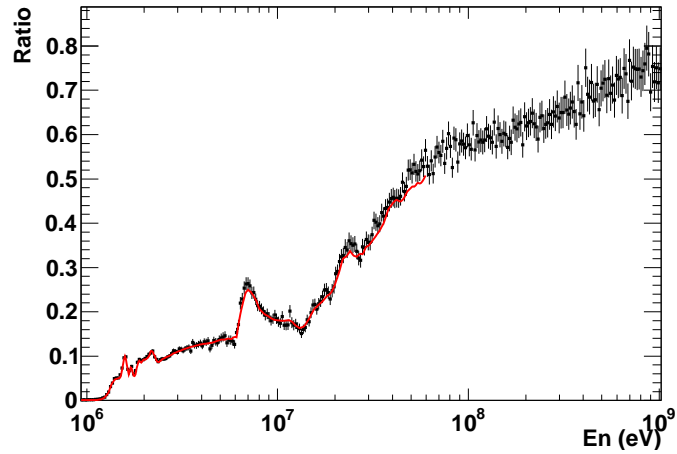
of the different samples, the experimental results, shown in Fig.5.13, were normalized to the integral value of the ENDF/B-VII.1 evaluation between 3 and 5 MeV. This energy interval was chosen because the cross section behaves smoothly and the anisotropy parameter does not present important variations in that region.

With this normalization factor, a good agreement between our results and the evaluation data in the whole energy range covered by it, from fission threshold up to 60 MeV, can be seen.

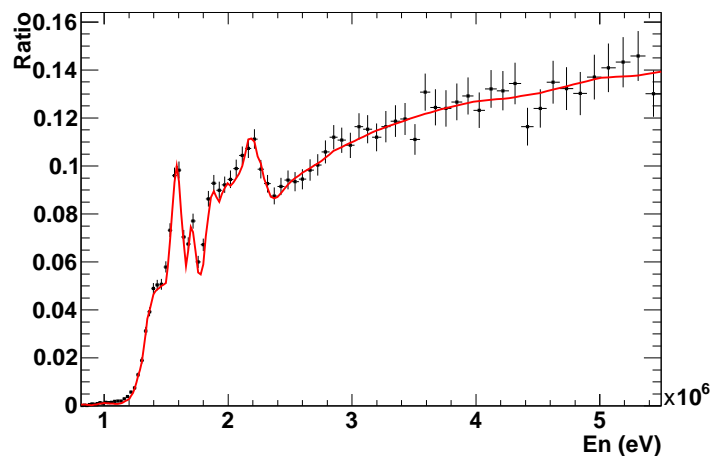
#### 5.2.4. Results on the $^{232}\text{Th}(n,f)$ cross section

Once we had obtained the fission cross section ratio  $\sigma_f(^{232}\text{Th})/\sigma_f(^{235}\text{U})$ , it was possible to calculate the  $^{232}\text{Th}(n,f)$  cross section using the evaluated values for the  $^{235}\text{U}(n,f)$  cross section as a reference.

The  $^{235}\text{U}(n,f)$  evaluation given by ENDF/B-VII.0 [130] is considered as a standard [111] and the last available version, ENDF/B-VII.1 [13], did not modify any of the neutron cross section standards. However, since this evaluation is limited to a neutron energy of 200 MeV, another evaluation had to be used for higher energies. The Japanese Evaluated Nuclear Data Library High Energy File (JENDL/HE-2007) [15] reaches up to 3 GeV neutron energy. Thus, the reference value for the  $^{235}\text{U}(n,f)$  cross section here used



(a)



(b)

Figure 5.13: Present data for the fission cross section ratio  $\sigma_f(^{232}\text{Th})/\sigma_f(^{235}\text{U})$ . Experimental values have been normalized to the integral value of the ENDF/B-VII.1 evaluation between 3 and 5 MeV neutron energy. The neutron energy range covers from fission threshold up to 1 GeV (a). The threshold region is amplified in (b).

is that of the ENDF/B-VII.1 up to 200 MeV, together with that of the JENDL/HE-2007 evaluation from 200 MeV up to 1 GeV.

The anisotropy correction explained in Section 5.2.2 was applied to obtain the result shown in Fig. 5.14.

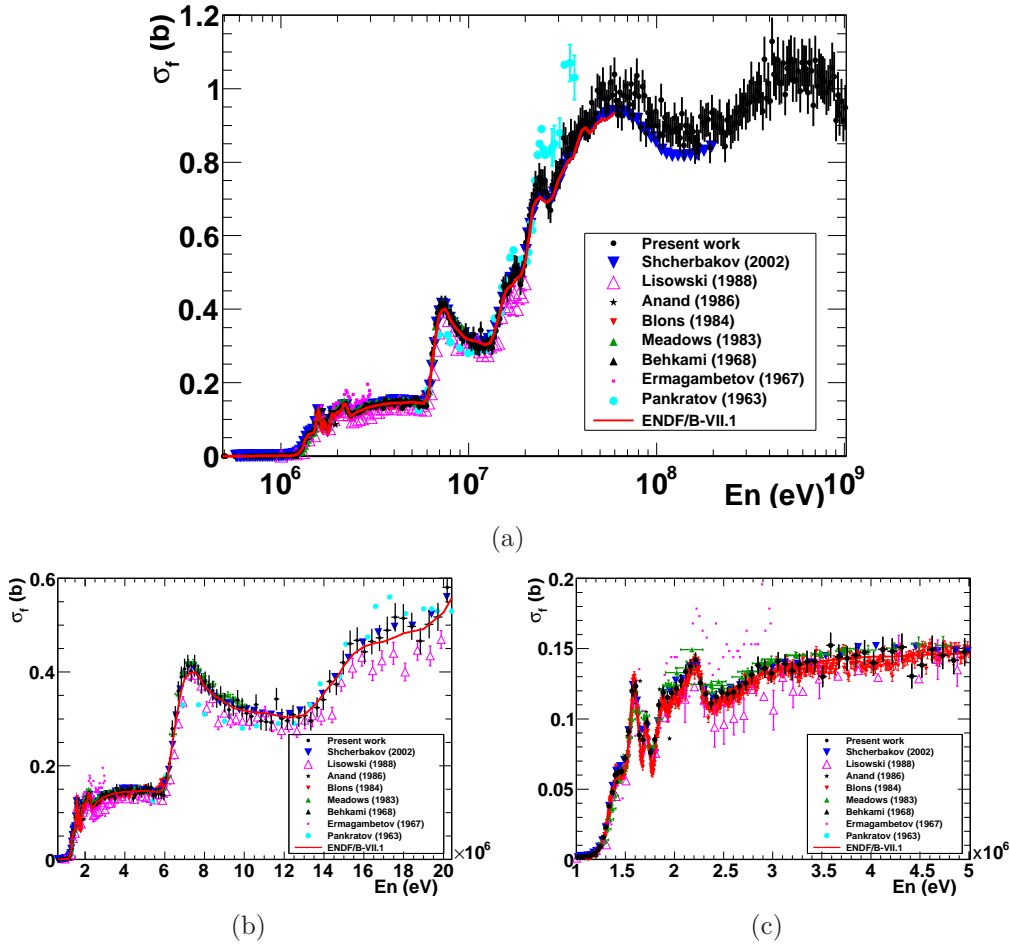


Figure 5.14: Neutron-induced fission cross section of  $^{232}\text{Th}$  obtained in present work compared with previous results from other authors and evaluations: (a) Full energy range results; detailed views in different energy ranges are shown in (b) and (c).

### Comparison with previous data

Fig. 5.14(a) shows the present work results for  $^{232}\text{Th}(n,f)$  in the whole energy range, from fission threshold up to 1 GeV. Previous measurements from other authors [55, 131–137] and from evaluations [13] are also shown. A good agreement is found, in general, with ENDF/B-VII.1 evaluation that reaches up to 60 MeV and it is based on the work presented in [22]. The only measurement reaching up to 200 MeV is the one from Shcherbakov et al. [137], that is compatible with our results within the statistical uncertainty, indicated by the error bars. The old measurement of Pankratov et al. [131] covers up to 40 MeV but clearly overestimates the fission cross

section value above 20 MeV. Data from Lisowski et al. [136] underestimates the cross section in the region from 2.5 MeV up to 20 MeV, as it can be better seen in Fig. 5.14(b), where a narrower energy region is shown. The fission threshold region is shown in more detail in Fig. 5.14(c) where the fine structure of the fission cross section can be seen. Again, there is a good agreement between our results and the previous measurements, except for those of Ermagambetov et al. [132].

### Comparison with evaluations

A comparison between our data and the major evaluated libraries (ENDF/B-VII.1 [13], JENDL-4.0 [14], JEFF-3.1.2 [16], BROND-2.2 [17] and CENDL-3.1 [18]) is shown in the upper panel of Fig. 5.15, where the error bars represent the statistical uncertainty. Ratios between the evaluations and our experimental results are also represented in the lower panels. Note that our data have been normalized taken as reference the data from ENDF/B-VII.1 in the energy range between 3 and 5 MeV.

It can be seen that the biggest discrepancies appear around the first- and the second-chance fission thresholds, making evident that the anisotropic emission effect is relevant in order to get an accurate measurement of the fission cross section:

- The ENDF/B-VII.1 evaluation is the only one reaching up to 60 MeV. It agrees our data up to 20 MeV, except at the first- and second-chance fission thresholds, where discrepancies of  $\sim 9\%$  are found in both cases. In the region above 20 MeV, this evaluation underestimates our results by a 4%.
- The JENDL-4.0 evaluation overestimates systematically our fission cross section around 6%. However, it underestimates the value at the first-chance (6%) while the second-chance is overestimated around 9%.
- The JEFF-3.1.2 evaluation overestimates systematically the fission cross section between 2 and 6 MeV by a 4%. Its behaviour around both first- and second-chance thresholds differs from the other evaluations, and differences up to 18% are found when compared with our data. At energies higher than 20 MeV, the overestimation amounts to 10%.
- BROND-2.2 evaluation agrees our data in all the energy range, except at the onsets of first- and second-chance fission, where it is underestimated by a 10%.

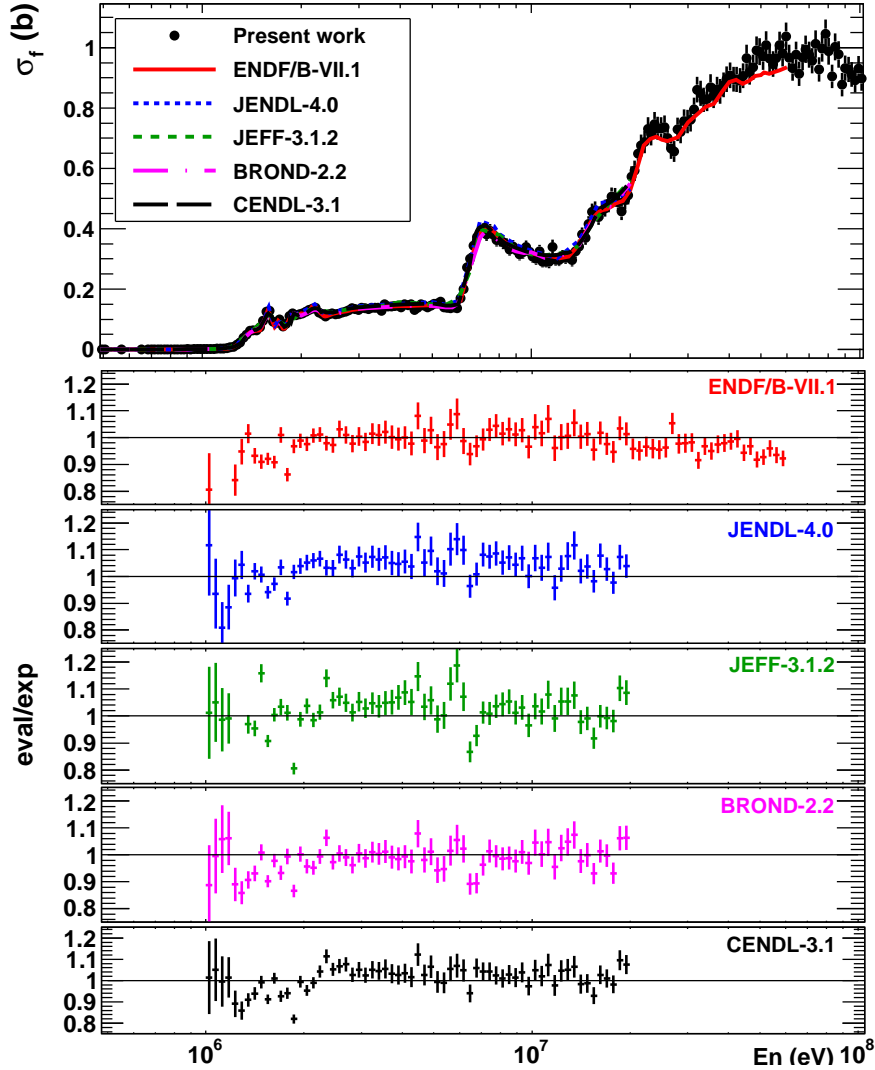


Figure 5.15: Fission cross section of  $^{232}\text{Th}$  given by our results and by evaluations (ENDF/B-VII.1, JENDL-4.0, JEFF-3.1.2, BROND-2.2 and CENDL-3.1) are shown in the upper panel. Ratios between these evaluations and our results are shown in the lower panels.

- CENDL-3.1 evaluation is compatible with our data except at the threshold, where a difference of 10% is observed. The value at the second-chance is lower than ours, but compatible within the statistical error.

The different evaluations are not compatible between them, and only BROND-2.2 and CENDL-3.1 agree our data in most of the evaluated range,

but important discrepancies exist at the multi-chance fission thresholds for all of them.

In any case, the different evaluations do not agree between them within the requested few per cent accuracy needed to the fast reactors development [10]. Moreover, they exhibit large differences around both first- and second-chance fission thresholds. This fact reinforces the idea of the lack of an adequate correction for the anisotropy at these energies where the higher-order Legendre polynomials are required.

### 5.3. Identification of fission modes

Different fission modes exist for actinides where asymmetric mass division is dominant over symmetric fission below  $\sim 30$  MeV, as explained in Chapter 1. Because of the equal linear momentum of both fission fragments, asymmetric mass division leads to different velocities of the fragments and, therefore, the heavy (HFF) and the light fission fragment (LFF) have different arrival times at the neighbouring detectors. The amplitudes of the signals produced in the PPACs are also different, as they depend on the energy deposited in the gas gaps, which are determined by the charge, mass and kinetic energy of the fragment.

In our case, the target backing breaks the symmetry in the amplitude and time distributions because one of the fission fragments deposits part of its kinetic energy in it, resulting in a lower energy that produces a signal of larger amplitude in the detector. On the other hand, due to this slowing down, the fragment also requires more time to reach the detector. An example of this was shown in Fig. 3.16, for neutron energies below 20 MeV. As it can be seen there, fission events accumulate in two regions with different amplitude values, corresponding to the cases  $amp_0 > amp_1$  (when the HFF passes through the backing, producing the amplitude value  $amp_1$ ), and  $amp_1 > amp_0$  (when the LFF produces  $amp_1$ ). The presence of two distinguishable bumps is a clear signature of the asymmetric fission, while a single bump implies symmetric fission.

This effect is also visible in the distribution of the time difference between both fission fragments (shown in Fig. 5.16 for energies below 20 MeV and after removing random coincidences; only data from one of the six samples of  $^{232}\text{Th}$  are represented). If the light fission fragment passes through the backing, the time difference  $t_0 - t_1$  is nearly equal to zero, because the slowing down in the backing is offset by the higher velocity of the LFF.

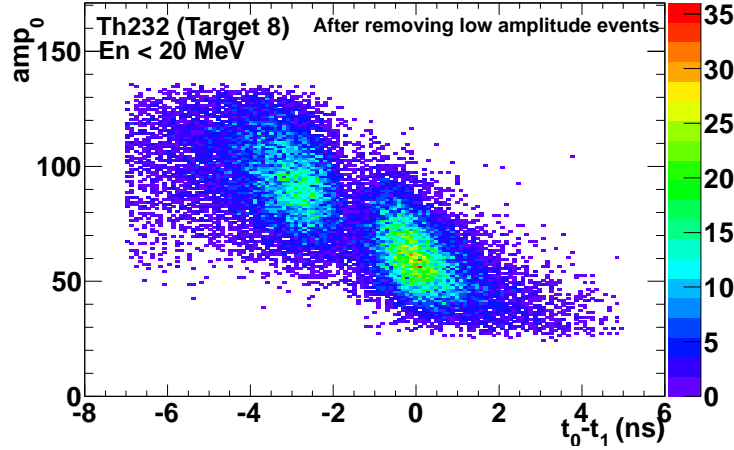


Figure 5.16: Two dimensional plot of the amplitude of the PPAC facing the backing versus the time difference between both PPACs, after removing the random coincidences. The time difference distribution is not centred at zero due to the presence of the backing, which slows down one of the two fission fragments. Data from one of the six samples of  $^{232}\text{Th}$ .

Therefore, in the case of asymmetric fission, the time difference  $t_0 - t_1$  is a good observable for determining whether the heavy or the light fission fragment is hitting the detector behind the backing. Taking advantage of this capability of the PPACs, it should be possible to disentangle the symmetric- and asymmetric-mode contribution to the fission cross sections and to the anisotropies. A detailed study is beyond the scope of this thesis, but some promising results are given here to show the capabilities of the experimental setup, which could be applied to a deeper analysis of the measured data.

When the heavy fission fragment goes through the backing, the slowing down is greater and a larger time difference appears, that depends also on the distance travelled by the fragment until its detection in the PPAC, as it can be seen in Fig. 5.17, where the travelled distance is proportional to  $\cos \theta_{det}$ , being  $\theta_{det}$  the incident angle in the detector. This behaviour is nearly constant if the LFF passes through the backing, as it was shown in Fig. 4.10, where the Geant4 results simulation work were presented.

Different cases covering all the energy range of interest are shown: in the four scatter plots below  $\sim 20$  MeV two *families* can be clearly distinguished, corresponding to whether the heavy or the light fragment passes through the backing; above this energy, the two *families* start to diminish and cannot be separated due to the growing of the symmetric fission, that covers the region

in between.

The time distributions  $t_0 - t_1$  obtained for one target of  $^{232}\text{Th}$  are shown in Fig. 5.18, fitted to the sum of two Gaussians so that the existence of two peaks can be more clearly distinguished when the asymmetric mode is visible, that means, at lower energies. A deeper study of the fits including a third Gaussian to account also for the symmetric mode is needed, besides a choice of narrower energy intervals, for investigating the ratio between fission modes, in particular at the multiple-chance fission thresholds that could give us relevant information on the fission process.

Fig. 5.19 reinforces the above information by showing the evolution of  $t_0 - t_1$  as a function of the neutron energy. Below 20 MeV, two regions corresponding to asymmetric fission can be clearly distinguished. As the energy increases, fission becomes more symmetric and, as expected [65], a one-peak distribution can be seen above  $\sim 50$  MeV.

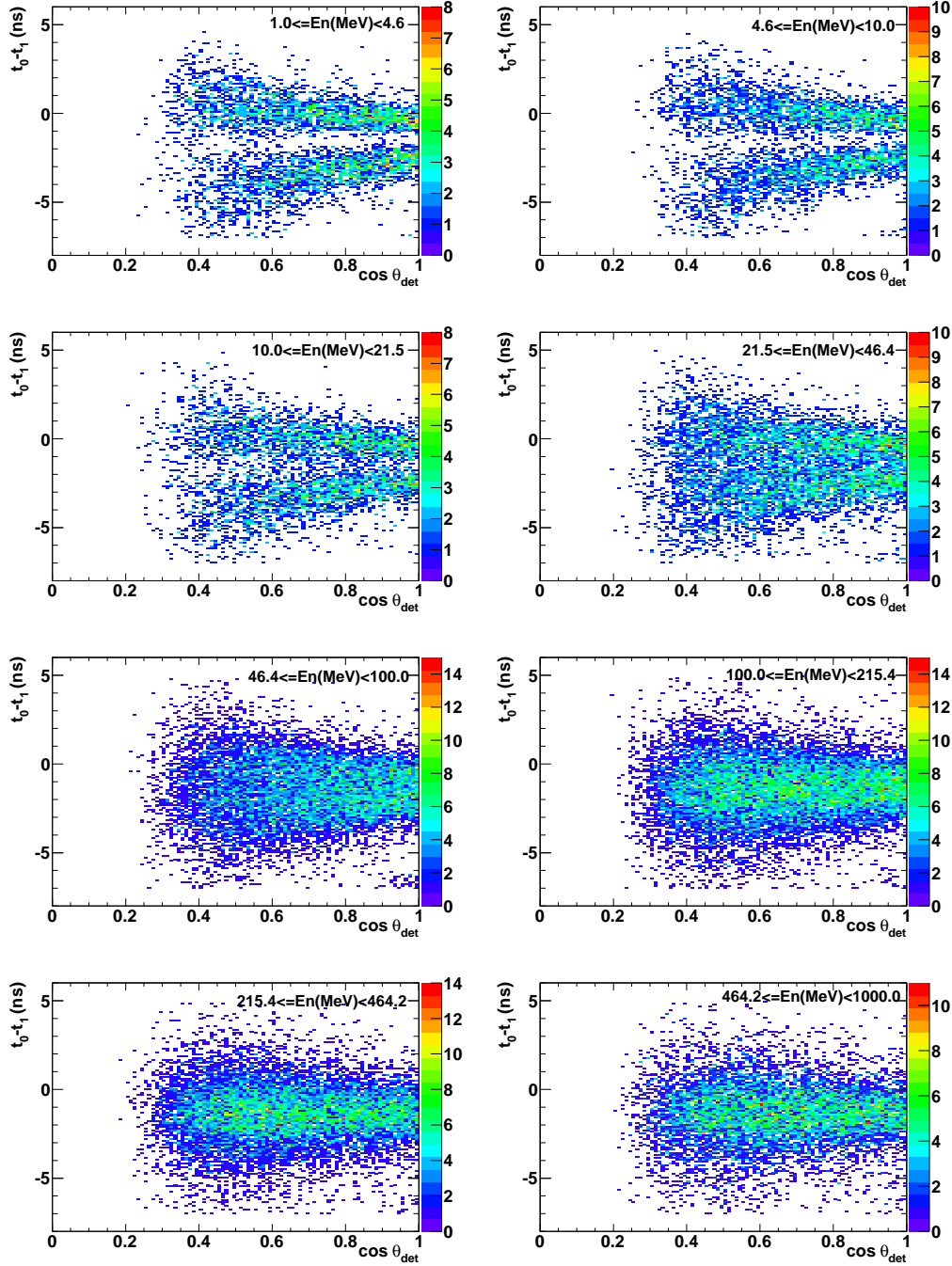


Figure 5.17: Time difference distribution  $t_0 - t_1$  for different energy intervals as a function of the cosine of the angle with respect to the detector. Below  $\sim 50$  MeV, two separated regions corresponding to asymmetric fission can be seen. At higher energies, the symmetric mode dominates the fission process.

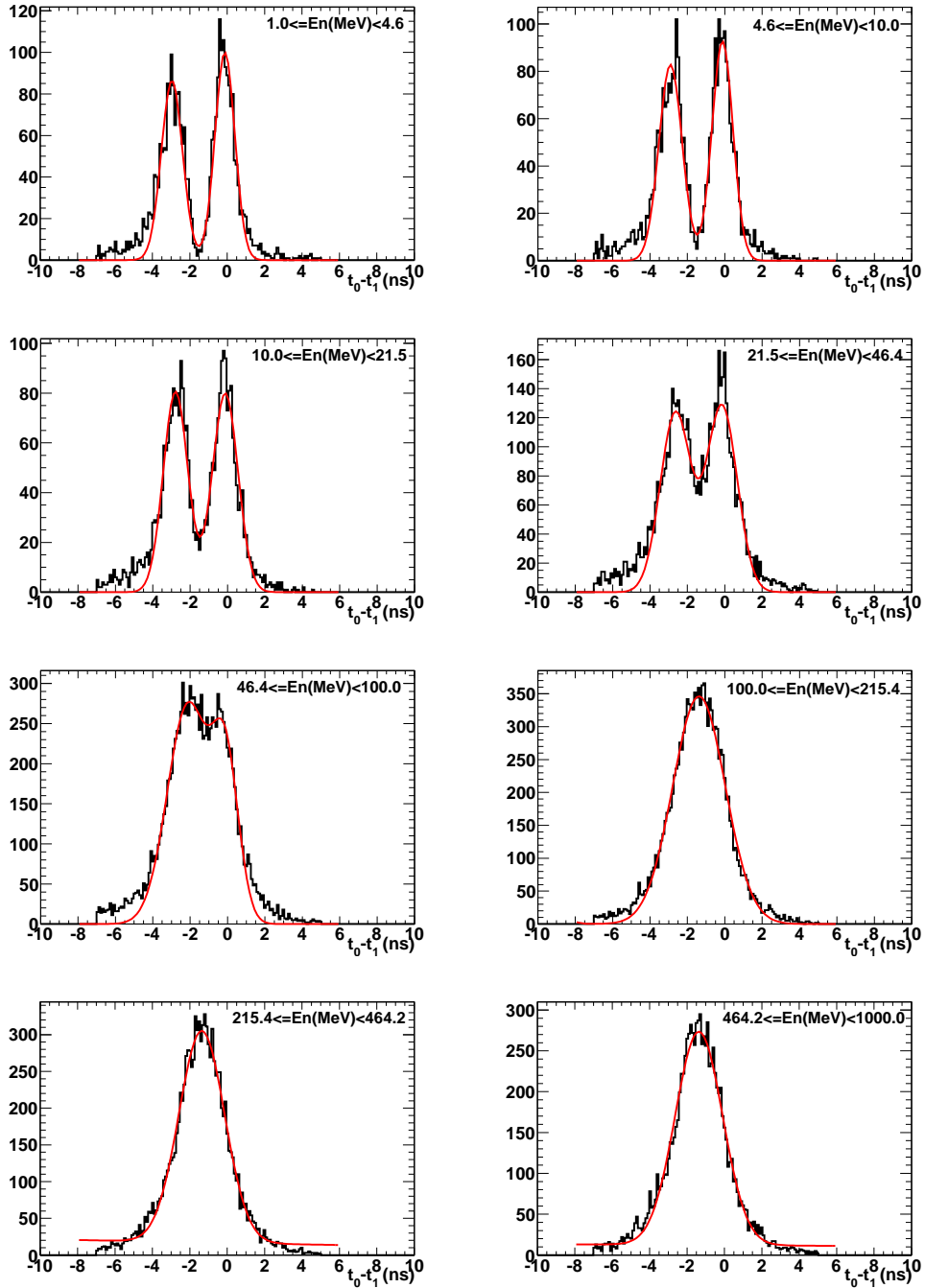


Figure 5.18: Time difference distribution  $t_0 - t_1$  for different energy intervals. Below  $\sim 50$  MeV, two peaks corresponding to asymmetric fission can be seen. At higher energies, fission is dominated by the symmetric mode.

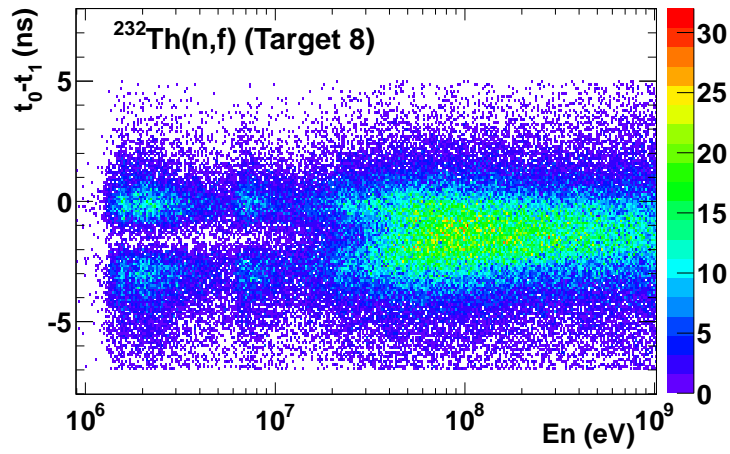


Figure 5.19: Evolution of the time difference between both PPACs with the neutron energy. Below 30 MeV, the asymmetric fission creates a good separation, making it easy to discern whether the heavy or the light fission fragment crossed the backing. Above that energy, the symmetric mode begins to take over and completely dominates the fission process beyond 50 MeV.



# Summary and conclusions

## Summary

This thesis work was done in the frame of the study of the neutron-induced fission of actinides and subactinides at the CERN n\_TOF facility using a fast Parallel Plate Avalanche Counters (PPACs) setup. This experimental setup provide us with an intense neutron beam with a white spectrum from thermal to 1 GeV and with an outstanding high resolution provided by its flight path of 185 m.

In our experiment, fission events were identified by detection of both fission fragments in time coincidence in the two PPAC detectors flanking the corresponding target. This technique allowed us to discriminate the fission events from the background produced by  $\alpha$  disintegration of radioactive samples and by particles produced in spallation reactions. Because PPAC detectors are insensitive to the  $\gamma$  flash, it is possible to reach energies as high as 1 GeV. The stripped cathodes provide the spatial position of the hits in the detectors, so that the emission angle of the fission fragments can be measured. Inside the reaction chamber up to nine targets can be simultaneously measured, using two of them as references ( $^{235}\text{U}$  and  $^{238}\text{U}$  in our case). The reliability of this method was established in earlier measurements of fission cross sections in actinides and subactinides up to 1 GeV neutron energy, with unprecedented resolution over the whole range.

The novel aspect of this experiment is the geometrical arrangement of the targets and detectors, which were tilted  $45^\circ$  with respect to the neutron beam direction. This configuration covered a larger angular acceptance to polar angles, so that the full angular distribution could be measured. In previous experiments, the perpendicular placement of the detector setup limited the acceptance to angles smaller than  $65^\circ$ . One main objective of this thesis is to demonstrate the suitability of such a geometrical configuration for measuring the angular distribution of the fragments emitted in fission.

$^{232}\text{Th}$  was a good study case because, in spite of the high interest of this nucleus as a component of nuclear reactors fuel, its large anisotropies (both in forward- and side-peaked distributions) that change quickly with the neutron energy, have been scarcely measured out of the fission threshold region.

All the experimental techniques used to obtain the final results of this work from the raw data are explained in the present manuscript. The first stage of the analysis involved identifying the fission events and rejecting the background signals. Analysis of the cathode signals to identify the position of the hits and, therefore, the trajectory of the fission fragments has also been explained. Finally, neutron energy was calculated using the time of flight technique and unambiguously associated to each fission event.

Simulation work was done with Geant4 to study the angular acceptance of this new experimental setup, and compare the results with the previously achieved when the detector setup was placed perpendicular to the beam direction. A good agreement between the simulation and experimental data was obtained for the  $^{235}\text{U}(\text{n},\text{f})$  case at low energies.

Finally, a study on the angular distribution of the fission events was presented, which made it possible to obtain the fission fragment angular distributions for the  $^{232}\text{Th}(\text{n},\text{f})$  reaction in the full energy range. The anisotropy parameter, defined as the ratio of the number of fragments emitted in the beam direction and at  $90^\circ$ , was calculated as a function of the neutron energy. In addition to this, the fission cross section of  $^{232}\text{Th}(\text{n},\text{f})$  was also provided, relative to the standard  $^{235}\text{U}(\text{n},\text{f})$  cross section. At this moment, because the target masses have not been measured yet, the cross section has been normalized to the ENDF/B-VII.1 evaluation.

It was shown how the symmetric and asymmetric fission modes can be identified with this experimental setup by using the time differences between both fission fragments. Its evolution with the neutron energy was also shown.

## Conclusions

The main conclusions that should be highlighted from this work are the following:

- This work confirms the excellent capabilities of the PPAC reaction chamber for studying the fission fragment angular distribution using the n\_TOF white neutron beam.
- The angular distribution of the fission fragments and the anisotropy

parameter of the  $^{232}\text{Th}(n,f)$  reaction were measured for the first time in a wide energy range covering from fission threshold up to 1 GeV.

- Around the fission threshold, there is consistency and good agreement between our results and previous data. We have also provided accurate results for the region around second-chance fission threshold, as well as at higher energies, where data were scarce and contradictory.
- An anisotropy value larger than 1 was found for energies above 20 MeV, confirming the only existing measurement done with neutrons up to 100 MeV up to date. Therefore, neutron-induced fission of  $^{232}\text{Th}$  is not isotropic at those energies, despite the high value of the orbital angular momentum of these neutrons.
- The fission cross section of  $^{232}\text{Th}(n,f)$  has been also provided, relative to the standard  $^{235}\text{U}(n,f)$  cross section, extending the available range in the evaluations up to 1 GeV. The value was normalized to the ENDF/B-VII.1 evaluation since no precise measurement on the target masses has been done to date.
- Comparisons between our  $^{232}\text{Th}$  fission cross section and different evaluations have been done. Important discrepancies have been pointed out, mainly at the onsets of multiple-chance fission, reinforcing the idea that precise measurements on the angular distribution are needed to measure correctly the fission cross sections.
- Finally, the way is paved to a new method to determine, using this experimental setup, the contribution of the symmetric and asymmetric fission modes for each neutron energy. A deeper analysis on the different contributions to the fission cross sections and to the angular distributions, mainly at the multiple-chance fission thresholds, could give important information on the fission process.

## Outlook

The success of this experiment to determine the angular distribution of the fragments emitted in the  $^{232}\text{Th}(n,f)$  reaction leads to new measurements using other nuclei that will be done at CERN-n\_TOF using the same experimental setup.

The fission cross section has been determined and properly corrected by the angular distribution of the fragments. However, the final result depends

on a normalization to evaluated data. An independent value of the fission cross section will be determined when target masses are accurately measured by using  $\alpha$  counting.

Since we have focused on calculating the angular distribution and fission cross section, not all the capabilities of this setup have been exploited, and only some of the features of the experimental data have been analysed in detail, but certain other aspects deserve to be studied in depth. One of them is take more advantage of the PPACs ability of distinguishing between symmetric and asymmetric fission modes using the time difference between both detectors. Thanks to the continuous energy beam available at n\_TOF facility, the evolution of both fission modes with the neutron energy and their contribution to the different multiple-chance fission channels can be studied, providing new data of great relevance in basic nuclear physics.

# Resumen en castellano

## Introducción

Este trabajo de tesis se centra en el estudio de la reacción de fisión inducida por neutrones en el  $^{232}\text{Th}$ , más concretamente, en el estudio de la distribución angular de los fragmentos de fisión emitidos y en su importancia para la medida de la sección eficaz de fisión usando detectores que presenten una aceptación limitada.

Con este objetivo, se ha llevado a cabo un experimento en la instalación n\_TOF (Neutron Time Of Flight) del CERN usando un dispositivo compuesto por detectores gaseosos de tipo PPAC (Parallel Plate Avalanche Counter) entre los que se intercalan los blancos con las muestras a estudiar. Dichos detectores tienen una respuesta temporal lo suficientemente rápida como para poder detectar reacciones de fisión de hasta 1 GeV de energía cinética, y ya habían sido usados con éxito para medir la sección eficaz de fisión en diferentes actínidos y subactínidos en n\_TOF, cubriendo un rango energético sin precedentes, desde neutrones térmicos hasta 1 GeV. Sus cátodos segmentados permiten localizar el punto de impacto de los fragmentos en el detector y reconstruir sus trayectorias.

El principio de funcionamiento se basa en la detección, en coincidencia temporal, de los dos fragmentos de fisión en los dos detectores situados a ambos lados del blanco. De esta forma se obtiene una buena separación entre los sucesos que corresponden a fisiones reales, y aquellos debidos a coincidencias aleatorias entre señales de sucesos no correlacionados y desintegraciones  $\alpha$  de isótopos radioactivos.

La novedad del experimento presentado aquí es la disposición geométrica de los detectores y los blancos, que han sido inclinados  $45^\circ$  respecto a la dirección del haz de neutrones con el fin de abarcar una mayor aceptación angular. Así, es posible detectar fragmentos de fisión emitidos a cualquier ángulo entre  $0^\circ$  y  $90^\circ$ , al contrario de lo que sucedía en experimentos ante-

riores, donde la disposición perpendicular de estos elementos respecto al haz limitaba la aceptación a ángulos por debajo de unos  $60^\circ$ .

Este trabajo tiene dos objetivos fundamentales: 1) Demostrar la idoneidad de este dispositivo experimental para medir distribuciones angulares de fragmentos de fisión y 2) medir la distribución angular y la sección eficaz de fisión del  $^{232}\text{Th}$  con neutrones de energías comprendidas entre el umbral de fisión y 1 GeV.

La medida de secciones eficaces de fisión siempre está afectada por la eficiencia limitada de los detectores, que nunca es del 100 %. Este efecto es especialmente importante si se usan detectores de geometría plano-paralela, como pueden ser los detectores PPAC. En tal caso, debemos tener un conocimiento preciso de la distribución angular de los fragmentos emitidos a todas las energías estudiadas con el fin de corregir la eficiencia de los detectores y poder obtener una medida precisa de la sección eficaz de fisión.

La elección del  $^{232}\text{Th}$  para este primer experimento no es casual, sino que obedece a las grandes variaciones del parámetro de anisotropía (definido como el cociente entre el número de fragmentos de fisión emitidos a  $0^\circ$  y a  $90^\circ$ ) que presenta en los umbrales de los diferentes canales de fisión con emisión de neutrones: (n,f), (n,n'f), (n,2n'f), ...

Sin embargo, y a pesar de la importancia del  $^{232}\text{Th}$  para el desarrollo de nuevos ciclos de combustible nuclear, como es el ciclo del torio-uranio, apenas existen datos de su distribución angular más allá del umbral de fisión, y los que hay, presentan grandes incertidumbres que los hacen incompatibles entre ellos, como puede verse en la Fig. 1(a). Con la realización de este experimento, se pretende cubrir esa falta de datos aportando valores para el continuo de energías entre el umbral de fisión y 1 GeV. La sección eficaz de fisión del  $^{232}\text{Th}$  también requiere de un nuevo estudio que arroje luz sobre las diferencias que existen entre las distintas evaluaciones disponibles, que son del orden del 10 % en torno al umbral de fisión, tal y como se muestra en la Fig. 1(b).

## Dispositivo experimental

### La instalación n\_TOF del CERN

El experimento analizado en esta tesis se ha llevado a cabo en n\_TOF (Neutron Time Of Flight), una instalación experimental situada en el CERN y dedicada al estudio de reacciones inducidas por neutrones, principalmente captura radiactiva (n, $\gamma$ ) y fisión (n,f), de gran interés en astrofísica y para el

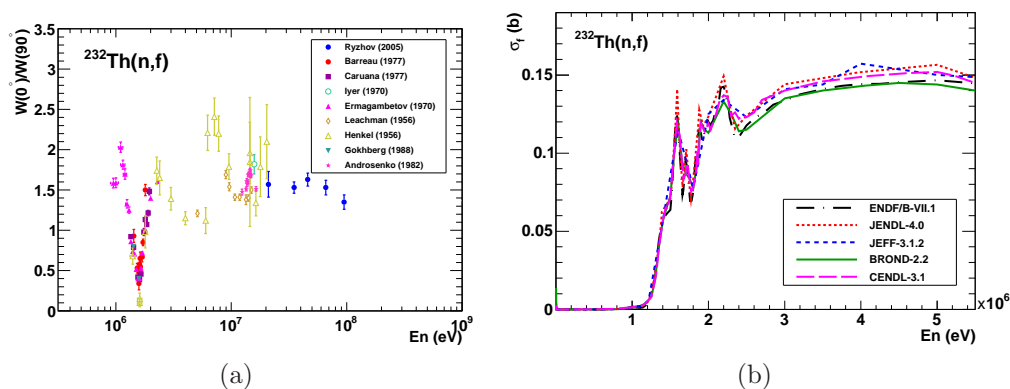


Figura 1: Situación actual de los datos para la reacción  $^{232}\text{Th}(n,f)$ . Los datos experimentales existentes para el parámetro de anisotropía se muestran en (a), mientras que la sección eficaz de fisión en el umbral dada por diferentes evaluaciones se puede ver en (b).

desarrollo de nuevas tecnologías dedicadas a la producción de energía nuclear y a la transmutación de residuos radiactivos.

Los neutrones se producen en un blanco de espalación, en el que incide un haz de protones de 20 GeV/c procedente del acelerador PS (Proton Synchrotron) del CERN. El blanco de espalación está rodeado por un circuito de agua que actúa como moderador de la energía de los neutrones, produciendo un espectro continuo en energía que abarca desde los neutrones térmicos hasta 1 GeV con una resolución en energía de  $3 \times 10^{-4}$  por debajo de varios keV, gracias a los 185 m de distancia de vuelo de los neutrones. Estas características del haz permiten extender el conocimiento de las secciones eficaces de fisión a energías de los neutrones no disponibles en ninguna otra instalación.

## Dispositivo experimental de medidas de fisión

Existen diferentes detectores en n\_TOF usados en medidas de secciones eficaces de fisión, como FIC (Fast Ionization Chamber) o MicroMegs. En nuestro caso nos centraremos en los detectores PPAC (Parallel Plate Avalanche Counter), usados en este experimento.

Un detector PPAC es un detector gaseoso que opera en modo proporcional y cuyos electrodos son placas situadas paralelamente y separadas por una pequeña distancia que ocupa el gas. Su presión puede variar entre 1 y 20 mbar, y un campo reducido del orden de 300 V/(cm·mbar) es suficiente para mantener el régimen proporcional de la cámara.

El diseño utilizado en este caso es el de una PPAC doble, con un ánodo común y dos cátodos segmentados en direcciones perpendiculares, de forma que se puede obtener la posición espacial de los fragmentos en los detectores. Esta posición se calcula a partir de la diferencia de tiempos entre las señales que llegan a ambos extremos de una línea de retardo a la que están conectadas todas las pistas de cada cátodo.

Los detectores usados para este trabajo han sido desarrollados y construidos en el IPN d'Orsay (Francia). Cada ánodo es una lámina de Mylar aluminizado por ambas caras, de  $20 \times 20$  cm<sup>2</sup> y  $1,5$   $\mu$ m de espesor. Está pegado a un marco hecho de resina epoxi y cubierto de una fina capa de cobre, para proteger el detector del ruido electromagnético. Los cátodos, situados a ambos lados y a  $3,2$  mm de distancia del ánodo, también están hechos de Mylar pero con una serie de pistas de aluminio de  $2$  mm de ancho y espaciadas  $100$   $\mu$ m. Cada pista está conectada a la línea de retardo, que es un hilo de cobre enrollado sobre una varilla de plástico de  $20$  cm. Los dos extremos del hilo se conectan a sendos preamplificadores para su lectura.

El gas utilizado es octafluoropropano (C<sub>3</sub>F<sub>8</sub>) a  $4$  mbar de presión, y se hace circular con un flujo de  $50$  l/h.

La cámara de vacío es un cilindro de acero inoxidable de  $1,63$  m de largo, y cuyo eje longitudinal se sitúa a lo largo del haz de neutrones. Dicha cámara puede albergar hasta diez detectores PPAC y nueve blancos intercalados. Con el objetivo de estudiar la distribución angular de los fragmentos, tanto los detectores como los blancos se encuentran rotados  $45^\circ$  con respecto a la dirección del haz.

En este experimento se han usado nueve blancos: seis de <sup>232</sup>Th, uno de <sup>237</sup>Np, uno de <sup>235</sup>U y uno de <sup>238</sup>U, estos dos últimos para ser usados como referencias, ya que sus secciones eficaces de fisión son consideradas como estándar. Cada blanco consiste en un fino depósito del isótopo (de unos  $0,3$  mg/cm<sup>2</sup>) con forma circular y  $80$  mm de diámetro, sobre una lámina de aluminio cuyo espesor es de  $0,75$   $\mu$ m para los blancos de <sup>232</sup>Th, y de  $2,5$   $\mu$ m para los demás.

## Análisis experimental

### Sucesos de fisión

Como cada blanco se encuentra entre dos detectores, los dos fragmentos de fisión son emitidos en direcciones opuestas y detectados casi simultáneamente. Por lo tanto, la identificación de sucesos de fisión se basa en la búsqueda

de señales en coincidencia en los ánodos de dos detectores adyacentes, como se indica en la Fig. 2. Este método permite discriminar, de una manera muy eficiente, los sucesos reales de fisión de señales debidas a desintegraciones  $\alpha$  de isótopos radioactivos y a partículas ligeras producidas por los neutrones en reacciones de espalación sobre los materiales interpuestos en el haz.

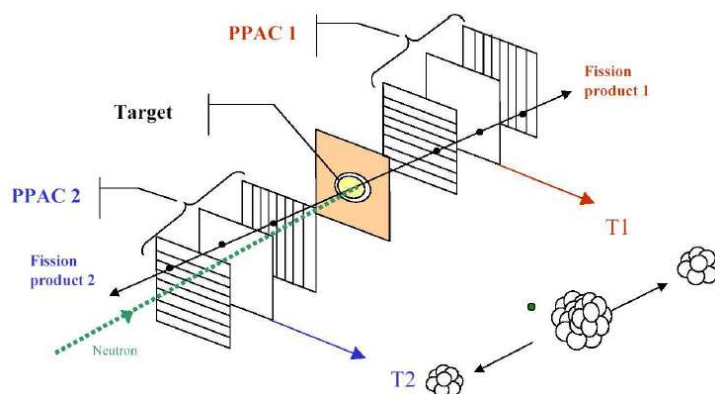


Figura 2: Suceso de fisión detectado con dos detectores PPAC.

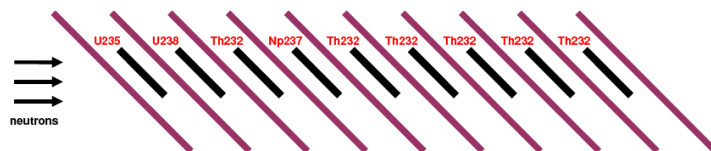


Figura 3: Vista esquemática del dispositivo experimental con diez detectores PPAC y nueve blancos intercalados entre ellos. Todos los elementos se encuentran rotados  $45^\circ$  para lograr una mayor aceptación en el ángulo polar  $\theta$  con respecto a la dirección del haz.

Dado que hay nueve blancos intercalados entre diez detectores, cada detector se utiliza para detectar fragmentos de dos blancos (Fig. 3). Además, cada fragmento de fisión puede atravesar más de un detector. Para determinar de qué blanco ha sido emitido un cierto fragmento deben estudiarse las propiedades temporales de las diferentes señales. Por ejemplo, para aquellos sucesos de fisión que dejen señal en tres detectores (etiquetados como 0, 1 y 2), el estudio de las diferencias de tiempos  $t_0 - t_1$  y  $t_1 - t_2$  permite identificar los sucesos de fisión producidos en el blanco 0 (es decir, el que se encuentra entre los detectores 0 y 1), y distinguirlos de aquellos producidos en el blanco 1 (entre los detectores 1 y 2), tal y como se puede ver en la Fig. 4. La acumulación de sucesos en torno a  $t_1 - t_2 = 0$ , corresponde a fisiones procedentes del

blanco 1 y, por tanto, no correlacionada con la diferencia de tiempos  $t_0 - t_1$ . Las fisiones producidas en el blanco 0 se encuentran en torno a  $t_0 - t_1 = 0$  y no muestran ninguna correlación con  $t_1 - t_2$ , excepto que esta diferencia debe ser negativa y menor de un cierto valor correspondiente al tiempo necesario para atravesar la distancia entre detectores.

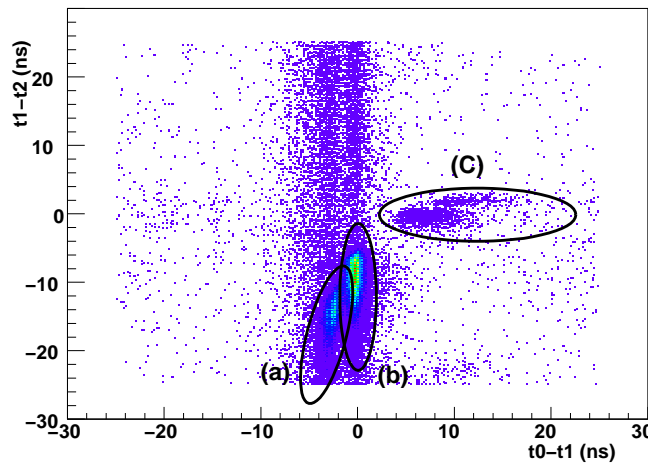


Figura 4: Histograma bidimensional de la distribución de la diferencia de tiempos para sucesos en los que tres detectores dan señales en coincidencia. Las fisiones producidas en el blanco 0 están señaladas como (a) si el fragmento pesado es el que atraviesa el soporte, y como (b) si lo hace el fragmento ligero. Los sucesos (c) corresponden a fisiones en el blanco 1.

### Localización espacial de los sucesos

Tal y como se ha comentado anteriormente, cada detector PPAC tiene dos cátodos segmentados en direcciones perpendiculares cuyas pistas están conectadas a una línea de retardo. La señal se propaga a través de esa línea hacia los dos extremos, donde es leída con un preamplificador. La diferencia de tiempos entre esas dos señales permite obtener la posición en la dirección horizontal o vertical, según la orientación de dicho cátodo.

Cada par de señales obtenidas en un cátodo debe cumplir la llamada “condición diagonal”:

$$t_{ch1} + t_{ch2} - 2t_0 = DLT \quad (11)$$

que establece que la suma de los tiempos de propagación de ambas señales

$t_{ch1}$  y  $t_{ch2}$  a lo largo de la línea de retardo es constante, ya que también lo es la longitud de la línea (DLT). El tiempo dado por la señal producida en el ánodo es  $t_0$  y se usa como referencia común. El nombre de dicha condición viene dado por la forma de la distribución bidimensional obtenida al representar  $t_{ch2} - t_0$  frente a  $t_{ch1} - t_0$ , como se puede ver en la Fig. 5(a).

Representando el primer término de la Ec. (11), como aparece en la Fig. 5(b), se puede ver el valor real de la longitud de cada cátodo (en unidades de tiempo). Estas distribuciones aparecen centradas en 360 ns y tienen una anchura de decenas de ns debido a la resolución temporal asociada a la lectura de los cátodos.

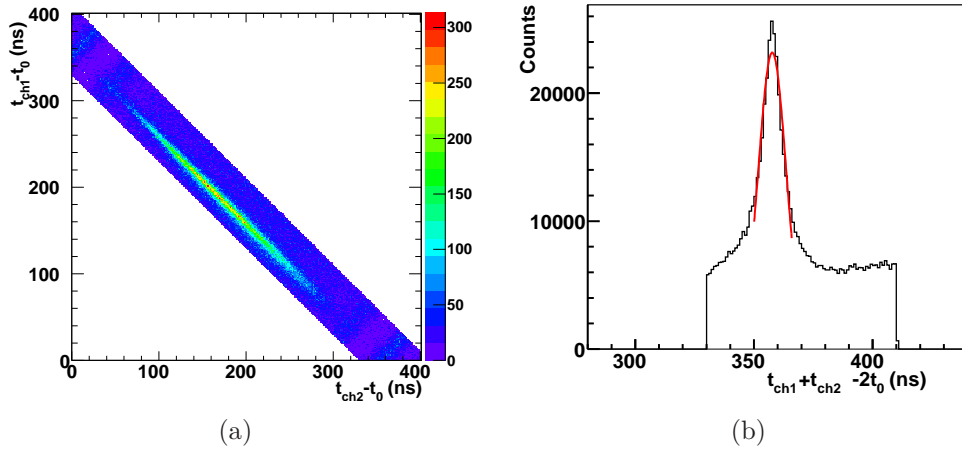


Figura 5: La correlación entre los tiempos de propagación a lo largo de la línea de retardo produce una diagonal (a). La longitud real de la línea de retardo, en unidades de tiempo, se muestra en (b) donde, debido a los preamplificadores, la distribución aparece centrada en 360 ns, en lugar de estarlo en el valor nominal de 300 ns.

Esta condición, junto con la necesidad de que la posición espacial calculada a partir de las señales de los cátodos corresponda con un punto real situado en el interior del detector, permite seleccionar aquellas señales válidas y asociarlas a las señales de los ánodos que definen los sucesos de fisión. De esta forma, para cada fisión se tienen cinco señales en cada detector (una del ánodo, y dos por cada uno de los cátodos), de forma que se puede reconstruir la trayectoria de los fragmentos, asumiendo que se emiten en direcciones opuestas.

### Cálculo del ángulo de emisión

La distribución angular se estudia en función de  $\cos \theta$ , siendo  $\theta$  el ángulo de salida de los fragmentos respecto a la dirección del haz de neutrones. Conociendo los puntos de impacto en cada detector,  $P_0 = (x_0, y_0, z_0)$  y  $P_1 = (x_1, y_1, z_1)$ , la dirección de emisión de los fragmentos está dada por el vector  $\vec{V} = P_1 - P_0 = (x_1 - x_0, y_1 - y_0, z_1 - z_0)$ . Por otra parte, la dirección del haz de neutrones es  $\vec{W} = (1, 0, -1)$ , de forma que el ángulo formado entre los vectores se puede obtener a partir del producto escalar:

$$\cos \theta = \frac{\vec{V} \cdot \vec{W}}{|\vec{V}| \cdot |\vec{W}|} \quad (12)$$

donde  $|\vec{V}|$  y  $|\vec{W}|$  son los módulos de  $\vec{V}$  and  $\vec{W}$ .

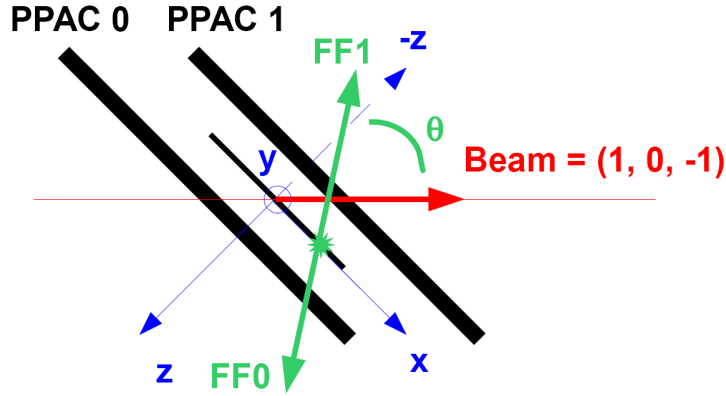


Figura 6: Sistema de referencia utilizado en el cálculo del ángulo de emisión de los fragmentos, FF0 y FF1, medido respecto a la dirección del haz de neutrones.

### Energía de los neutrones

La energía cinética de los neutrones se calcula a partir de su tiempo de vuelo y de la distancia recorrida usando la expresión relativista:

$$E = m_n c^2 \left( \sqrt{\frac{1}{1 - \frac{1}{c^2} \left(\frac{L}{T}\right)^2}} - 1 \right) \quad (13)$$

donde  $m_n$  es la masa del neutrón,  $L$  es la distancia recorrida y  $T$  el tiempo de vuelo. Debido a que los neutrones se producen en una fuente de espalación, la distancia recorrida debe tener en cuenta la llamada “distancia de

moderación”, que es la distancia efectiva recorrida por los neutrones en el proceso de moderación tanto dentro del blanco de espalación como dentro del moderador, y que se puede estimar a partir de simulaciones hechas con el código de transporte de neutrones FLUKA.

Los valores conocidos para la energía de las resonancias de fisión del  $^{235}\text{U}$  a baja energía permiten ajustar la distancia  $L$  incluida en el cálculo de la energía hecho con la Ec. (13).

## Simulación

Para determinar la eficiencia de detección de este dispositivo experimental, así como su aceptación angular, se ha llevado a cabo un trabajo de simulación con Geant4, un paquete informático que simula la interacción de partículas con la materia usando métodos Monte Carlo.

Se ha implementado una versión simplificada del sistema real de detección, considerando únicamente dos detectores y el blanco que se encuentra entre ellos. Dado que sólo estamos interesados en el frenado de los fragmentos de fisión a través de las diferentes capas de material, sólo se han incluido los elementos que componen las partes activas de los detectores y el blanco (formado por el depósito del isótopo a estudiar y una lámina de aluminio), omitiendo los marcos de los electrodos y del blanco.

En cada evento simulado, se lanzan dos fragmentos de fisión en direcciones opuestas desde un punto aleatorio en el interior del blanco. La carga y la masa de los fragmentos se eligen de acuerdo a una distribución de probabilidad generada a partir de las distribuciones de carga y masa dadas por la evaluación ENDF/B-VII.1, mientras que la energía cinética se calcula a partir de la sistemática de Viola. El ángulo de emisión también se determina mediante una distribución de probabilidad que se define usando una serie de polinomios de Legendre en  $\cos\theta$ . Los valores de esos coeficientes determinan la forma de la distribución angular que, para calcular la eficiencia total de detección, se tomará como isotrópica.

Consideramos que un suceso de fisión ha sido detectado, y que además se puede reconstruir su trayectoria, si cumple la condición de que ambos fragmentos depositen una cierta energía en cada una de los dos capas de gas que tiene cada detector. De esta manera, se define la eficiencia de detección como el cociente entre el número de sucesos que cumplan estos requisitos, y el número de sucesos lanzados en la simulación.

El resultado más importante para demostrar la viabilidad de este expe-

rimento es el que se muestra en la Fig. 7. En dicha figura se representa la eficiencia de detección en función del ángulo de emisión  $\cos\theta$  para dos configuraciones geométricas de los detectores: Cuando los detectores y el blanco se sitúan perpendicularmente a la dirección del haz, la aceptación angular está limitada a ángulos menores que  $65^\circ$ . Sin embargo, en la situación actual, con los detectores y el blanco inclinados  $45^\circ$ , la aceptación angular cubre todos los posibles valores de  $\theta$  entre  $0^\circ$  y  $90^\circ$ . A pesar de que la eficiencia presenta una fuerte dependencia con el ángulo, esta última configuración permite estudiar la distribución angular de los fragmentos de fisión.

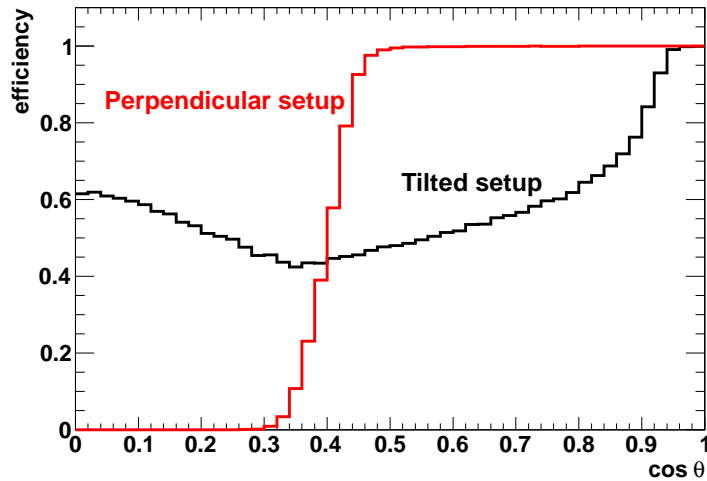


Figura 7: Comparación de las eficiencias de detección para diferentes disposiciones geométricas: perpendicular y rotado  $45^\circ$  respecto a la dirección del haz.

## Resultados de la reacción $^{232}\text{Th}(n,f)$

### Distribución angular de los fragmentos de fisión

En esta última parte se calcula la distribución angular de los fragmentos de fisión del  $^{232}\text{Th}$  así como su parámetro de anisotropía en función de la energía del neutrón incidente.

La distribución angular de los fragmentos se mide respecto al coseno del ángulo que forma la dirección del haz de neutrones con la dirección de salida de los fragmentos, obtenida a partir de sus posiciones en los dos detectores. La anchura de los intervalos de energía se define lo más estrecha posible, pero manteniendo un número de cuentas suficientes en cada intervalo para

poder hacer el análisis de la distribución. Además, dentro de cada intervalo de energía, se han tomado 15 intervalos en  $\cos \theta$ .

Para corregir las distribuciones angulares del  $^{232}\text{Th}$  por el efecto de la eficiencia de detección, éstas se dividen entre la distribución obtenida para el  $^{235}\text{U}$  por debajo de 1 keV ya que, para este caso, la emisión de fragmentos es isótropa. Esas distribuciones ya normalizadas se ajustan a una serie de polinomios de Legendre en  $\cos \theta$ :

$$W(\theta) = A_0 \left[ 1 + \sum_{\substack{L=2 \\ L \text{ par}}}^{L_{\text{máx}}} A_L P_L(\cos \theta) \right] \quad (14)$$

donde  $L$  es el orden del polinomio. En nuestro caso físico, sólo se tienen en cuenta los términos de orden par debido a la simetría en la emisión hacia adelante y hacia atrás.

El valor máximo  $L_{\text{máx}}$  para cada intervalo de energía se obtiene ajustando la distribución con los valores  $L_{\text{máx}}=2, 4, \text{ y } 6$ , y un test  $\chi^2$  determina cuál es el mejor ajuste en cada caso. En la Fig. 8 se muestran dos ejemplos de distribuciones ajustadas a series de Legendre con  $L_{\text{máx}}=2, 4, \text{ y } 6$ . La Fig. 8(a) corresponde a un caso donde la emisión de los fragmentos se produce, principalmente, a  $0^\circ$ , esto es, en la dirección del haz de neutrones; en la Fig. 8(b), la mayor parte de los fragmentos son emitidos a  $45^\circ$ .

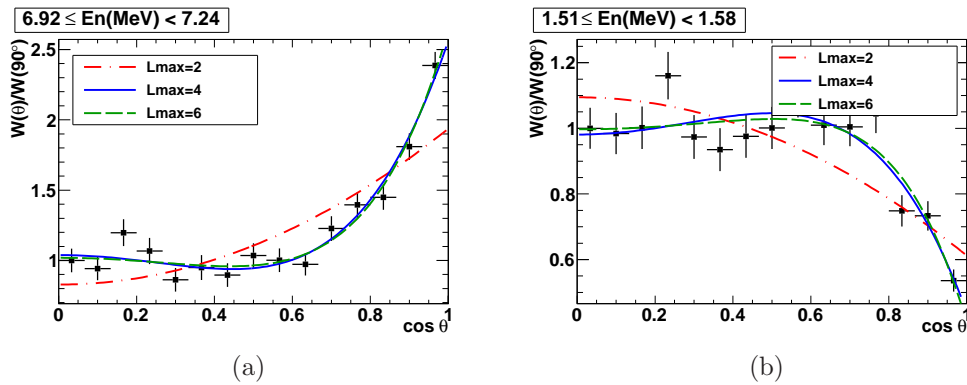


Figura 8: Ejemplos de distribuciones angulares normalizadas de los fragmentos emitidos en la reacción  $^{232}\text{Th}(n,f)$ . La Fig. (a) corresponde a una distribución en la que la mayor parte de los fragmentos se emiten en la dirección del haz, mientras que en la Fig. (b), el máximo de la distribución se encuentra a unos  $45^\circ$ . En ambos casos se muestran los ajustes hechos a series de Legendre de 2°, 4°, y 6° orden.

El parámetro de anisotropía se define como el cociente del número de

fragmentos emitidos a  $0^\circ$  y a  $90^\circ$ , y puede calcularse analíticamente usando los coeficientes del ajuste a la serie de Legendre, mediante la siguiente ecuación:

$$A = \frac{W(0^\circ)}{W(90^\circ)} = \frac{1 + A_2 + A_4 + A_6 + \dots}{1 - \frac{1}{2}A_2 + \frac{3}{8}A_4 - \frac{5}{16}A_6 + \dots} \quad (15)$$

Este parámetro permite ver la evolución de la distribución angular con la energía, tal y como se muestra en la Fig. 9 para el caso del  $^{232}\text{Th}$ . La anisotropía presenta una estructura que está relacionada con la de la sección eficaz, ya que las mayores variaciones ocurren para el umbral de fisión (1-2 MeV), y para el umbral de los canales  $(n,n'f)$  y  $(n,2n'f)$ , en torno a 7 y 15 MeV, respectivamente.

Los datos obtenidos en el presente trabajo muestran un buen acuerdo con los datos existentes en torno al umbral de fisión. A energías mayores apenas existen datos experimentales y, a menudo, son incompatibles entre ellos. Este experimento contribuye a mejorar el conocimiento de la reacción de fisión inducida por neutrones en  $^{232}\text{Th}$  proporcionando resultados experimentales en todo el continuo de energías comprendido entre el umbral de fisión y 1 GeV.

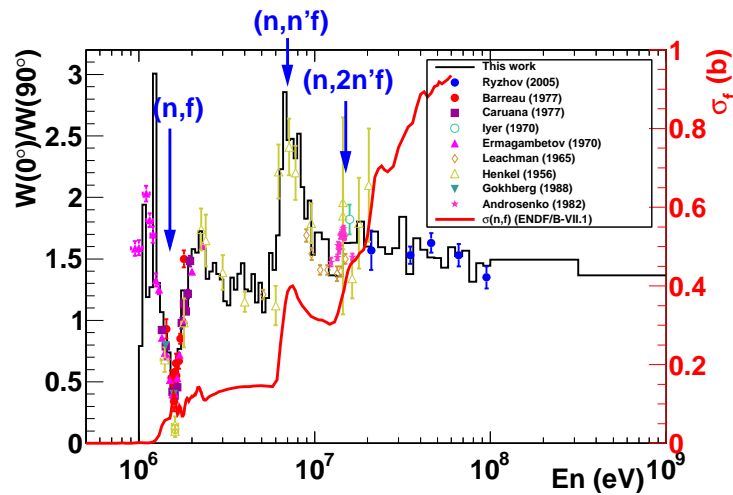


Figura 9: Dependencia del parámetro de anisotropía con la energía del neutrón incidente para la reacción  $^{232}\text{Th}(n,f)$  obtenido en este trabajo, comparado con resultados anteriores obtenidos por otros autores. Se observa cómo la estructura de la anisotropía está relacionada con la de la sección eficaz de fisión, cuyos umbrales de los canales aparecen indicados por las flechas.

## Sección eficaz de fisión

La sección eficaz de fisión del  $^{232}\text{Th}$  puede obtenerse en el mismo experimento usando el  $^{235}\text{U}$  como referencia. Dado que la atenuación del flujo de neutrones es despreciable a lo largo de todo el dispositivo experimental, el cociente de secciones eficaces de dos muestras es independiente del flujo, e igual a:

$$\frac{\sigma_i(E)}{\sigma_j(E)} = \frac{C_i(E)}{C_j(E)} \cdot \frac{N_j}{N_i} \cdot \frac{\epsilon_j(E)}{\epsilon_i(E)} \quad (16)$$

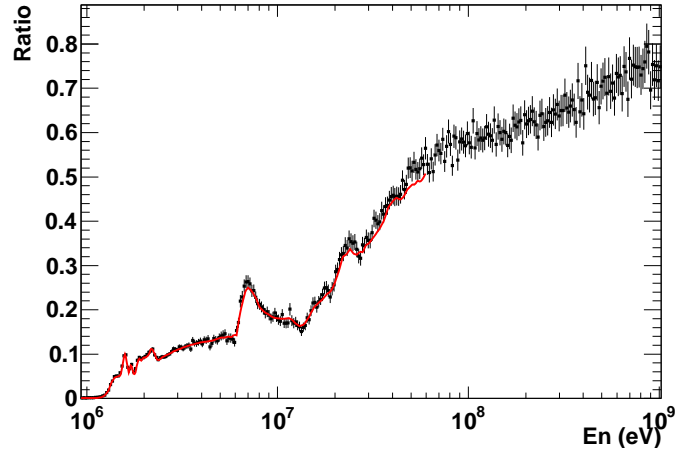
donde el blanco etiquetado como  $j$  es el blanco de referencia ( $^{235}\text{U}$  en este caso) cuya sección eficaz de fisión se supone bien conocida.  $C(E)$  es el número de sucesos de fisión detectados,  $N$  es el número de átomos en el blanco, y  $\epsilon(E)$  es la eficiencia de detección.

Dado que disponemos de seis blancos de  $^{232}\text{Th}$ , las incertidumbres sistemáticas debidas a inhomogeneidades o a diferencias en el espesor de la lámina sobre la que se depositan las muestras se pueden separar de aquellos efectos introducidos por la diferente distribución angular de cada núcleo, que ha de ser igual para los seis blancos.

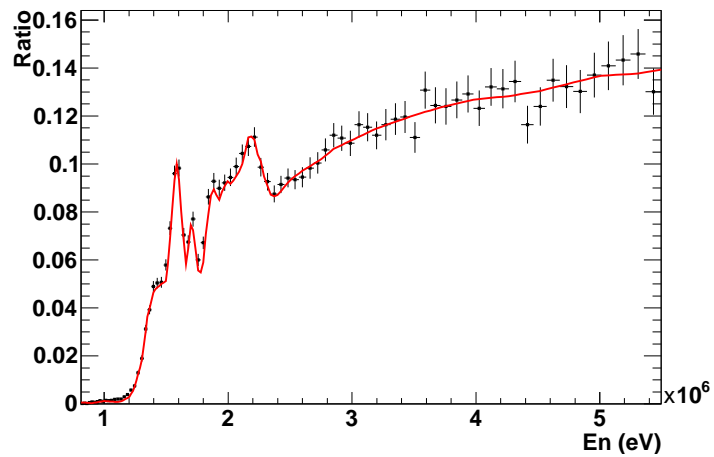
El cociente de secciones eficaces  $^{232}\text{Th}(\text{n,f})/^{235}\text{U}(\text{n,f})$  calculado en este trabajo para energías de los neutrones comprendidas entre el umbral de fisión y 1 GeV se muestra en la Fig. 10. Estos valores están normalizados al valor integral del mismo cociente en el intervalo de 3 a 5 MeV dado por la evaluación ENDF/B-VII.1, ya que no se conoce la masa de los blancos con precisión. La medida de estas masas está pendiente de realizarse con el fin de poder obtener un valor final que no dependa de dicha normalización.

La sección eficaz de fisión del  $^{232}\text{Th}$  puede obtenerse multiplicando el cociente de secciones eficaces  $\sigma_{\text{n,f}}(^{232}\text{Th})/\sigma_{\text{n,f}}(^{235}\text{U})$  por la sección eficaz de fisión del  $^{235}\text{U}$ , cuya evaluación ENDF/B-VII.1 se considera estándar hasta 200 MeV. Por encima de ese valor usamos la evaluación JENDL/HE-2007. El valor final obtenido así para la sección eficaz de fisión del  $^{232}\text{Th}$  se muestra en la Fig. 11.

Se ha aplicado una corrección por el efecto que tiene la diferencia de anisotropías entre el  $^{232}\text{Th}$  y el  $^{235}\text{U}$  en la aceptación angular de los detectores. Dicha corrección alcanza el 6 % tanto en el umbral de fisión como en el umbral de la emisión de un neutrón en la fisión (n,n'f), valores que corresponden a las energías donde el  $^{232}\text{Th}$  presenta las mayores anisotropías. Podemos aplicar dicha corrección gracias a la configuración geométrica utilizada, en la que se puede medir, con precisión, la distribución angular de los fragmentos de fisión.



(a)



(b)

Figura 10: Cociente de las secciones eficaces  $\sigma_f(^{232}\text{Th})/\sigma_f(^{235}\text{U})$  obtenidos en el presente trabajo. Los resultados están normalizados al valor integral de la evaluación ENDF/B-VII.1 en el intervalo de energías comprendido entre 3 y 5 MeV. El rango de energía del neutrón se extiende desde el umbral de fisión hasta 1 GeV (a). La zona del umbral de fisión se muestra en detalle en (b).

Otras configuraciones con una aceptación angular más limitada no permiten medir la distribución angular y, en consecuencia, las medidas de sección eficaz deben ser corregidas utilizando valores ya conocidos de la anisotropía de los núcleos involucrados.

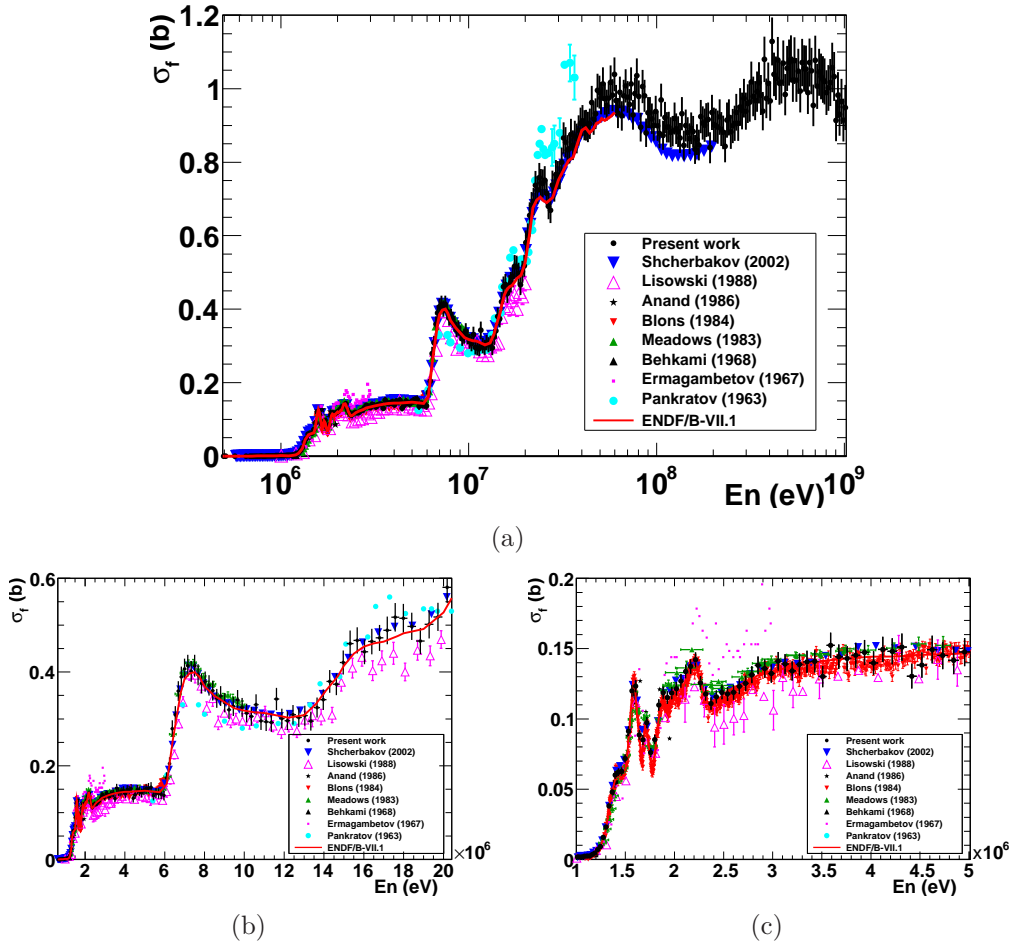


Figura 11: Sección eficaz de fisión inducida por neutrones para el  $^{232}\text{Th}$  obtenida en el presente trabajo (a), donde también se muestran resultados previos obtenidos por otros autores. En (b) y (c) se muestran vistas detalladas de ciertos rangos de energía.

## Conclusiones

En este trabajo se ha probado un dispositivo experimental basado en detectores PPAC girados  $45^\circ$  para medir la distribución angular de los fragmentos emitidos en la fisión inducida por neutrones. El experimento se ha realizado en la instalación n\_TOF del CERN con un haz de neutrones cuyo rango de energía abarca desde neutrones térmicos hasta 1 GeV.

El experimento presentado aquí, en el que se ha estudiado la reacción  $^{232}\text{Th}(n,f)$ , es la primera medida experimental de la distribución angular

de los fragmentos de fisión que cubre un rango tan amplio de energías del neutrón incidente. El buen acuerdo con los datos disponibles demuestra la capacidad del sistema experimental para medir las distribuciones angulares de los fragmentos emitidos. Dado el éxito de este primer experimento, ya está prevista la realización de nuevas medidas de otros núcleos usando el mismo dispositivo de detección en la instalación n.TOF.

La medida de la sección eficaz de fisión, corregida por los efectos de anisotropía, también se ha calculado para el  $^{232}\text{Th}$ . Sin embargo, la obtención de un valor definitivo que no dependa de la normalización a una evaluación está supeditado a la medida precisa de las masas de los blancos utilizados, que está prevista próximamente.

# Appendix A

## Legendre polynomials

In the present work, the Fission Fragment Angular Distribution  $W(\theta)$  is described by means of a series of Legendre polynomials  $P_n(\cos \theta)$ . In this Appendix, the Legendre polynomials and some of their properties are presented. The aim is to provide a quick reference on these polynomials and to justify their convenience in the present case, but any attempt to demonstrate their mathematical properties or the theorems mentioned here is beyond the scope of this work. More complete and rigorous derivations of the properties presented here can be found in numerous textbooks on mathematics [138–140] and from the point of view of the applications in physics [141–143]. A quick summary of the Legendre polynomials properties, without demonstrations, is included in Ref. [144].

### A.1. Introduction to the Legendre polynomials

Legendre polynomials appear in many problems of physics having spherical symmetry, for instance, in the separation of variables of the Schrödinger wave equation for central force fields, as discussed in Chapter 1:

$$-\frac{\hbar^2}{2\mu} \nabla^2 \Psi + V(r, s)\Psi_i = E\psi \quad (\text{A.1})$$

where the angular dependence comes entirely from the Laplacian operator, so that the following eigenvalues equation must be satisfied:

$$\left[ \frac{1}{\sin \theta} \frac{\partial}{\partial \theta} \left( \sin \theta \frac{\partial}{\partial \theta} \right) + \frac{1}{\sin^2 \theta} \frac{\partial^2}{\partial \phi^2} \right] Y = -\lambda Y \quad (\text{A.2})$$

As it has been explained in Chapter 1, the normalized solutions for this angular equation are the spherical harmonics  $Y(\theta, \phi)$ , that have the form:

$$Y_{l,m}(\theta, \phi) = (-1)^m \left[ \frac{(2l+1)(l-m)!}{4\pi(l+m)!} \right]^{1/2} e^{im\phi} P_l^m(\cos\theta) \quad (\text{A.3})$$

where  $l$  and  $m$  are integers, with  $l \geq 0$  and  $|m| < l$ . The functions  $P_l^m(\cos\theta)$  are the associated Legendre polynomials of order  $m$ , that include the dependence on the polar angle  $\theta$ . In the particular case where there is no dependence on the azimuthal angle  $\phi$ ,  $m = 0$  and the polynomials  $P_l^m(\cos\theta)$  are reduced to the  $P_l(\cos\theta)$ , which are named Legendre polynomials, and are solutions of the Legendre equation:

$$\frac{d}{d(\cos\theta)} \left[ (1 - \cos^2\theta) \frac{dy(\cos\theta)}{d(\cos\theta)} \right] + \lambda y(\cos\theta) = 0 \quad (\text{A.4})$$

If  $\lambda = n(n+1)$ , being  $n$  a non-negative integer, the solutions to Eq. (A.4) are the Legendre polynomials  $P_n(\cos\theta)$ , that can be obtained by using the Rodrigues' formula:

$$P_n(\cos\theta) = \frac{1}{2^n n!} \frac{d^n}{d(\cos\theta)^n} [(\cos^2\theta - 1)^n] \quad (\text{A.5})$$

where  $n$  is the degree of the polynomial. Some of the Legendre polynomials are shown in Table A.1 and are represented in Fig. A.1.

## A.2. Properties of the Legendre polynomials

Although it can be demonstrated rigorously [141], a first glance on the Legendre polynomials in Table A.1 show us that they verify the following parity property:

$$P_n(-\cos\theta) = (-1)^n P_n(\cos\theta) \quad (\text{A.6})$$

This means that the polynomials have a parity even or odd (with respect to  $\cos\theta$ ) depending whether the degree  $n$  of the polynomial is even or odd. The symmetric or antisymmetric character can be clearly seen in Fig. A.1, where the even and odd order polynomials have been represented in different plots. This is an important property in quantum mechanics where, for central forces,  $n$  is a quantum number relating parity and angular momentum.

$n$	Legendre polynomials
0	$P_0(\cos \theta) = 1$
1	$P_1(\cos \theta) = \cos \theta$
2	$P_2(\cos \theta) = \frac{1}{2}(3 \cos^2 \theta - 1)$
3	$P_3(\cos \theta) = \frac{1}{2}(5 \cos^3 \theta - 3 \cos \theta)$
4	$P_4(\cos \theta) = \frac{1}{8}(35 \cos^4 \theta - 30 \cos^2 \theta + 3)$
5	$P_5(\cos \theta) = \frac{1}{8}(63 \cos^5 \theta - 70 \cos^3 \theta + 15 \cos \theta)$
6	$P_6(\cos \theta) = \frac{1}{16}(231 \cos^6 \theta - 315 \cos^4 \theta + 105 \cos^2 \theta - 5)$
7	$P_7(\cos \theta) = \frac{1}{16}(429 \cos^7 \theta - 693 \cos^5 \theta + 315 \cos^3 \theta - 35 \cos \theta)$

Table A.1: First Legendre polynomials.

Another important property that is worth mentioning here is the orthogonality of the Legendre polynomials. They verify the relationship:

$$\int_{-1}^{+1} P_n(\cos \theta) P_m(\cos \theta) = \begin{cases} \frac{2}{2n+1} & \text{if } m = n \\ 0 & \text{if } m \neq n \end{cases} \quad (\text{A.7})$$

so that  $P_0(\cos \theta), P_1(\cos \theta), P_2(\cos \theta), \dots, P_n(\cos \theta), \dots$  is a sequence of orthogonal polynomials in the interval  $[-1, +1]$ .

In addition, it can be demonstrated that the Legendre polynomials form a complete set (see, for example, Refs. [138, 141]). Therefore, any arbitrary function  $f(\cos \theta)$  on  $[-1, +1]$  can be expanded in Legendre series<sup>1</sup>:

$$f(\cos \theta) = \sum_{n=0}^{\infty} c_n P_n(\cos \theta) \quad (\text{A.8})$$

This is the most useful property for the purposes of the present work. Thanks to this theorem, it is possible to describe any angular distribution

<sup>1</sup>Strictely, this is possible for any function  $f(\cos \theta)$  whose integral

$$\int_{-1}^{+1} |f(\cos \theta)|^2 d(\cos \theta)$$

exists. Rigorous justifications of this theorem can be found in Refs. [138, 141].

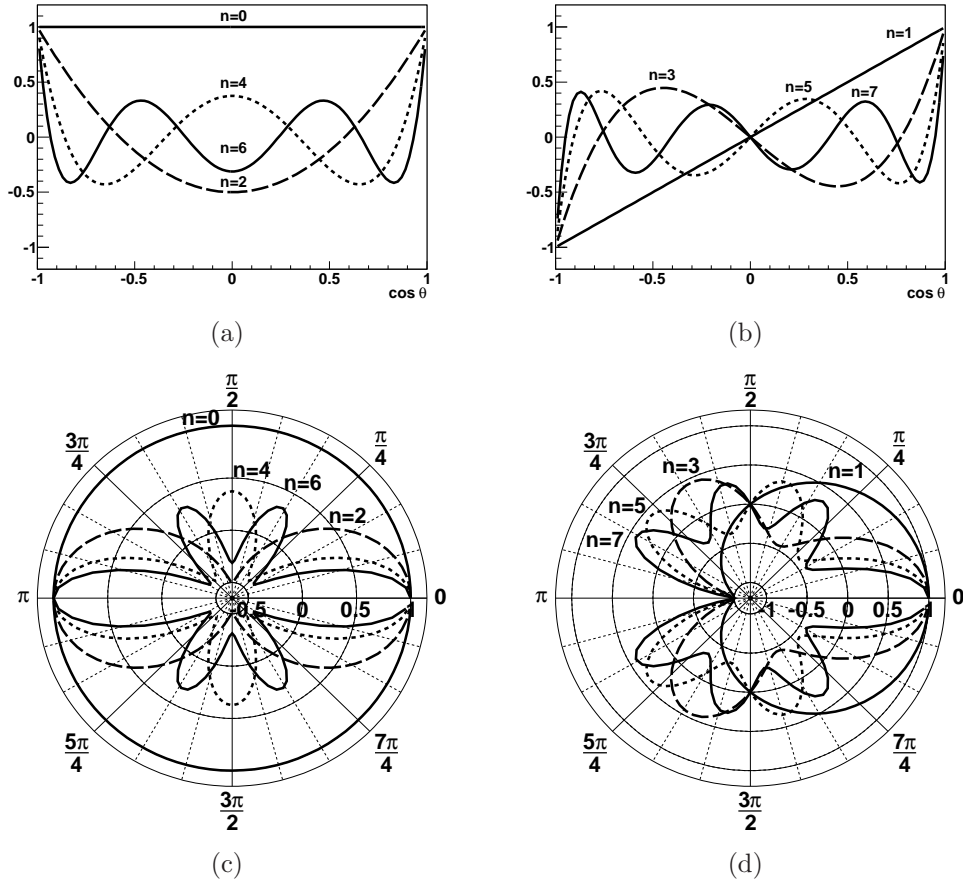


Figure A.1: Even (a) and odd (b) order Legendre polynomials. Polar representations are given in (c) and (d).

$W(\theta)$  of the emitted fission fragments by using a sum of Legendre polynomials in  $\cos \theta$ .

The emission of fission fragments is symmetric with respect to  $\theta = 90^\circ$ , since there is no difference between the backward and the forward emitted fragments. The parity property expressed by Eq. (A.6) indicates that only even order polynomials have this behaviour, as it can be also seen in the polar representations in Figs. A.1(c) and (d). It is easy to verify that any function made of a sum of only even Legendre polynomials is also even. Therefore, any angular distribution of fission fragments  $W(\theta)$  can be expressed as a sum of only even order Legendre polynomials.

# Appendix B

## Linear momentum transfer

The emission angles of the fission fragments given in the laboratory frame  $\theta_{lab}$  and in the center-of-masses (CM) frame  $\theta_{cm}$  are related through a Lorentz transformation, where the center-of-masses frame has a velocity  $v_{cm}$  with respect to the laboratory, that we assume parallel to the z-axis. In such a case, if  $E$  and  $\vec{p}$  are the relativistic energy and the momentum of the fragment in the laboratory frame, and  $E'$  and  $\vec{p}'$  are given in the CM frame, the relationships between both coordinate systems are given by Eqs. (B.1) and (B.2):

$$p'_x = p_x \quad (\text{B.1a}) \quad p_x = p'_x \quad (\text{B.2a})$$

$$p'_y = p_y \quad (\text{B.1b}) \quad p_y = p'_y \quad (\text{B.2b})$$

$$p'_z = \frac{p_z - \frac{v_{cm} \cdot E}{c^2}}{\sqrt{1 - \beta^2}} \quad (\text{B.1c}) \quad p_z = \frac{p'_z + \frac{v_{cm} \cdot E'}{c^2}}{\sqrt{1 - \beta^2}} \quad (\text{B.2c})$$

$$E' = \frac{E - v_{cm} \cdot p_z}{\sqrt{1 - \beta^2}} \quad (\text{B.1d}) \quad E = \frac{E' + v_{cm} \cdot p'_z}{\sqrt{1 - \beta^2}} \quad (\text{B.2d})$$

where  $\beta = v_{cm}/c$  and  $\gamma = 1/\sqrt{1 - \beta^2}$ .

The angles  $\theta_{lab}$  and  $\theta_{cm}$  are the ones formed by the emission direction (in laboratory and CM frames, respectively) and the z direction, as indicated in Fig. B.1, so that:

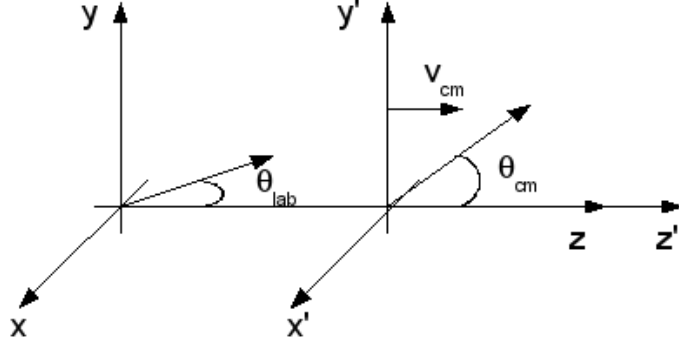


Figure B.1: Center-of-mass and laboratory frames.

$$\tan \theta_{lab} = \frac{p_y}{p_z} \qquad \tan \theta_{cm} = \frac{p'_y}{p'_z}$$

Therefore, we can use the Lorentz transformations, Eqs. (B.1) and (B.2), to write  $\tan \theta_{lab}$  as a function of the magnitudes in the center-of-mass frame:

$$\tan \theta_{lab} = \frac{p_y}{p_z} = \frac{p'_y}{\frac{p'_z + \frac{v_{cm} \cdot E'}{c^2}}{\sqrt{1-\beta^2}}}$$

Using that  $p'_y = p' \cdot \sin \theta_{cm}$ , we finally obtain:

$$\tan \theta_{lab} = \frac{p' \cdot \sin \theta_{cm}}{\gamma (p' \cdot \cos \theta_{cm} + \frac{v_{cm} \cdot E'}{c^2})} = \frac{\sin \theta_{cm}}{\gamma (\cos \theta_{cm} + \beta/\beta'_1)} \quad (\text{B.3})$$

where  $\beta'_1$  is the velocity of the fission fragment in the center-of-mass frame.

In the non-relativistic limit, when the linear momentum transferred by the neutron to the nucleus is small,  $\beta \rightarrow 0$ , both angles are equal:  $\tan \theta_{lab} = \tan \theta_{cm}$  and, therefore,  $\theta_{lab} = \theta_{cm}$ .

# Appendix C

## Numerical results

Table C.1: Numerical values of the coefficients of the fit to the angular distribution of  $^{232}\text{Th}(n,f)$  for each neutron energy interval and the anisotropy parameter calculated from them.

$En$ (MeV)	$A_0$	$A_2$	$A_4$	$A_6$	$A = \frac{W(0^\circ)}{W(90^\circ)}$
1.00 – 1.05	$0.57 \pm 0.12$	$-0.15 \pm 0.42$	0	0	$0.79 \pm 0.54$
1.05 – 1.10	$1.67 \pm 0.23$	$0.48 \pm 0.32$	0	0	$1.94 \pm 0.84$
1.10 – 1.15	$0.54 \pm 0.07$	$0.50 \pm 0.30$	$0.38 \pm 0.39$	$-0.59 \pm 0.49$	$1.19 \pm 0.79$
1.15 – 1.20	$1.71 \pm 0.16$	$0.38 \pm 0.20$	$-0.47 \pm 0.26$	$-0.08 \pm 0.34$	$1.27 \pm 0.90$
1.20 – 1.26	$1.08 \pm 0.07$	$0.47 \pm 0.15$	$0.44 \pm 0.19$	$0.46 \pm 0.24$	$3.01 \pm 0.75$
1.26 – 1.32	$1.05 \pm 0.04$	$0.18 \pm 0.09$	0	0	$1.30 \pm 0.16$
1.32 – 1.38	$0.89 \pm 0.02$	$0.04 \pm 0.06$	0	0	$1.07 \pm 0.09$
1.38 – 1.45	$1.10 \pm 0.02$	$-0.04 \pm 0.04$	0	0	$0.94 \pm 0.06$
1.45 – 1.51	$1.13 \pm 0.02$	$-0.08 \pm 0.04$	$-0.17 \pm 0.06$	$-0.02 \pm 0.07$	$0.74 \pm 0.11$
1.51 – 1.58	$0.94 \pm 0.02$	$-0.27 \pm 0.03$	$-0.26 \pm 0.04$	0	$0.45 \pm 0.05$
1.58 – 1.66	$1.05 \pm 0.02$	$-0.17 \pm 0.03$	$-0.26 \pm 0.04$	0	$0.58 \pm 0.06$
1.66 – 1.74	$1.10 \pm 0.02$	$-0.08 \pm 0.04$	$-0.18 \pm 0.05$	0	$0.77 \pm 0.07$
1.74 – 1.82	$1.05 \pm 0.02$	$0.15 \pm 0.04$	0	0	$1.24 \pm 0.07$
1.82 – 1.91	$1.00 \pm 0.02$	$0.08 \pm 0.04$	$0.13 \pm 0.05$	$-0.06 \pm 0.06$	$1.11 \pm 0.10$
1.91 – 2.00	$0.95 \pm 0.02$	$0.23 \pm 0.04$	$0.24 \pm 0.05$	0	$1.50 \pm 0.07$
2.00 – 2.09	$1.01 \pm 0.02$	$0.29 \pm 0.04$	$0.17 \pm 0.05$	0	$1.58 \pm 0.08$
2.09 – 2.19	$1.02 \pm 0.02$	$0.25 \pm 0.04$	$0.26 \pm 0.05$	0	$1.55 \pm 0.07$
2.19 – 2.29	$1.08 \pm 0.02$	$0.35 \pm 0.04$	$0.19 \pm 0.05$	0	$1.73 \pm 0.08$
2.29 – 2.40	$1.07 \pm 0.02$	$0.33 \pm 0.04$	0	0	$1.58 \pm 0.08$
2.40 – 2.51	$1.10 \pm 0.02$	$0.20 \pm 0.04$	0	0	$1.34 \pm 0.07$
2.51 – 2.63	$0.98 \pm 0.02$	$0.17 \pm 0.04$	$0.23 \pm 0.06$	0	$1.40 \pm 0.08$

Continued on next page

Table C.1: (continued)

$En$ (MeV)	$A_0$	$A_2$	$A_4$	$A_6$	$A = \frac{W(0^\circ)}{W(90^\circ)}$
2.63 – 2.75	$1.15 \pm 0.02$	$0.22 \pm 0.04$	$0.06 \pm 0.06$	$0.04 \pm 0.07$	$1.47 \pm 0.14$
2.75 – 2.88	$1.04 \pm 0.02$	$0.22 \pm 0.04$	0	0	$1.38 \pm 0.08$
2.88 – 3.02	$1.02 \pm 0.02$	$0.19 \pm 0.04$	$0.04 \pm 0.06$	0	$1.33 \pm 0.08$
3.02 – 3.16	$1.04 \pm 0.02$	$0.22 \pm 0.05$	$0.16 \pm 0.06$	$-0.21 \pm 0.07$	$1.16 \pm 0.13$
3.16 – 3.31	$1.12 \pm 0.02$	$0.20 \pm 0.05$	$0.15 \pm 0.06$	$-0.20 \pm 0.08$	$1.12 \pm 0.14$
3.31 – 3.47	$1.16 \pm 0.03$	$0.21 \pm 0.05$	0	0	$1.35 \pm 0.09$
3.47 – 3.63	$1.05 \pm 0.03$	$0.21 \pm 0.05$	$0.20 \pm 0.07$	$-0.15 \pm 0.09$	$1.25 \pm 0.15$
3.63 – 3.80	$1.08 \pm 0.03$	$0.20 \pm 0.05$	$0.10 \pm 0.07$	0	$1.38 \pm 0.10$
3.80 – 3.98	$1.05 \pm 0.03$	$0.23 \pm 0.05$	$0.16 \pm 0.07$	0	$1.47 \pm 0.10$
3.98 – 4.17	$0.96 \pm 0.02$	$0.11 \pm 0.05$	$0.12 \pm 0.07$	0	$1.25 \pm 0.09$
4.17 – 4.37	$0.90 \pm 0.02$	$0.08 \pm 0.05$	$0.19 \pm 0.07$	0	$1.24 \pm 0.09$
4.37 – 4.57	$1.15 \pm 0.03$	$0.16 \pm 0.06$	$0.21 \pm 0.08$	0	$1.38 \pm 0.11$
4.57 – 4.79	$0.95 \pm 0.03$	$0.10 \pm 0.06$	$0.05 \pm 0.08$	$-0.03 \pm 0.10$	$1.15 \pm 0.17$
4.79 – 5.01	$1.13 \pm 0.03$	$0.19 \pm 0.06$	0	0	$1.31 \pm 0.11$
5.01 – 5.25	$0.96 \pm 0.03$	$0.04 \pm 0.06$	0	0	$1.06 \pm 0.09$
5.25 – 5.50	$1.11 \pm 0.03$	$0.11 \pm 0.06$	0	0	$1.18 \pm 0.10$
5.50 – 5.75	$1.05 \pm 0.03$	$0.22 \pm 0.07$	$0.36 \pm 0.09$	0	$1.55 \pm 0.12$
5.75 – 6.03	$1.11 \pm 0.03$	$0.24 \pm 0.07$	0	0	$1.41 \pm 0.13$
6.03 – 6.31	$1.12 \pm 0.03$	$0.30 \pm 0.06$	$0.38 \pm 0.08$	0	$1.69 \pm 0.11$
6.31 – 6.61	$1.51 \pm 0.03$	$0.55 \pm 0.05$	$0.35 \pm 0.07$	0	$2.23 \pm 0.13$
6.61 – 6.92	$1.21 \pm 0.02$	$0.63 \pm 0.05$	$0.45 \pm 0.06$	$0.19 \pm 0.07$	$2.86 \pm 0.23$
6.92 – 7.24	$1.21 \pm 0.02$	$0.64 \pm 0.04$	$0.48 \pm 0.06$	0	$2.47 \pm 0.12$
7.24 – 7.59	$1.33 \pm 0.03$	$0.65 \pm 0.05$	$0.38 \pm 0.06$	0	$2.48 \pm 0.13$
7.59 – 7.94	$1.25 \pm 0.03$	$0.53 \pm 0.05$	$0.36 \pm 0.06$	$0.07 \pm 0.08$	$2.32 \pm 0.20$
7.94 – 8.32	$1.08 \pm 0.02$	$0.54 \pm 0.05$	$0.39 \pm 0.06$	$0.16 \pm 0.08$	$2.52 \pm 0.21$
8.32 – 8.71	$1.05 \pm 0.02$	$0.50 \pm 0.05$	$0.32 \pm 0.07$	0	$2.08 \pm 0.12$
8.71 – 9.12	$1.07 \pm 0.02$	$0.39 \pm 0.05$	$0.26 \pm 0.07$	0	$1.83 \pm 0.11$
9.12 – 9.55	$1.20 \pm 0.03$	$0.38 \pm 0.05$	$0.25 \pm 0.07$	$0.10 \pm 0.09$	$1.97 \pm 0.20$
9.55 – 10.00	$1.01 \pm 0.02$	$0.26 \pm 0.05$	$0.16 \pm 0.07$	0	$1.53 \pm 0.10$
10.00 – 10.96	$1.08 \pm 0.02$	$0.35 \pm 0.04$	$0.19 \pm 0.05$	0	$1.71 \pm 0.08$
10.96 – 12.02	$1.06 \pm 0.02$	$0.25 \pm 0.04$	$0.21 \pm 0.05$	$0.08 \pm 0.07$	$1.66 \pm 0.14$
12.02 – 13.18	$1.05 \pm 0.02$	$0.16 \pm 0.04$	$0.19 \pm 0.05$	0	$1.37 \pm 0.08$
13.18 – 14.45	$1.04 \pm 0.02$	$0.21 \pm 0.04$	$0.26 \pm 0.05$	$-0.09 \pm 0.07$	$1.36 \pm 0.12$
14.45 – 15.85	$1.08 \pm 0.02$	$0.30 \pm 0.04$	$0.24 \pm 0.05$	0	$1.63 \pm 0.07$
15.85 – 17.38	$1.09 \pm 0.02$	$0.29 \pm 0.04$	$0.28 \pm 0.05$	0	$1.63 \pm 0.07$
17.38 – 19.05	$0.99 \pm 0.02$	$0.37 \pm 0.03$	$0.30 \pm 0.05$	0	$1.80 \pm 0.07$
19.05 – 20.89	$1.03 \pm 0.02$	$0.29 \pm 0.03$	$0.36 \pm 0.04$	$-0.05 \pm 0.06$	$1.60 \pm 0.10$

Continued on next page

Table C.1: (continued)

$En$ (MeV)	$A_0$	$A_2$	$A_4$	$A_6$	$A = \frac{W(0^\circ)}{W(90^\circ)}$
20.89 – 22.91	$1.15 \pm 0.02$	$0.33 \pm 0.03$	$0.30 \pm 0.04$	$0.00 \pm 0.05$	$1.72 \pm 0.10$
22.91 – 25.12	$1.08 \pm 0.01$	$0.27 \pm 0.03$	$0.33 \pm 0.04$	$-0.02 \pm 0.05$	$1.59 \pm 0.09$
25.12 – 27.54	$1.03 \pm 0.01$	$0.25 \pm 0.03$	$0.25 \pm 0.04$	$-0.00 \pm 0.05$	$1.54 \pm 0.09$
27.54 – 30.20	$1.07 \pm 0.01$	$0.29 \pm 0.03$	$0.18 \pm 0.04$	0	$1.59 \pm 0.06$
30.20 – 33.11	$1.05 \pm 0.01$	$0.31 \pm 0.03$	$0.35 \pm 0.03$	$0.09 \pm 0.04$	$1.84 \pm 0.09$
33.11 – 36.31	$1.10 \pm 0.01$	$0.21 \pm 0.03$	$0.24 \pm 0.03$	$-0.06 \pm 0.04$	$1.38 \pm 0.07$
36.31 – 39.81	$1.17 \pm 0.01$	$0.22 \pm 0.02$	$0.30 \pm 0.03$	$0.10 \pm 0.04$	$1.67 \pm 0.08$
39.81 – 43.65	$1.13 \pm 0.01$	$0.26 \pm 0.02$	$0.25 \pm 0.03$	0	$1.57 \pm 0.05$
43.65 – 47.86	$1.02 \pm 0.01$	$0.22 \pm 0.02$	$0.29 \pm 0.03$	0	$1.51 \pm 0.05$
47.86 – 52.48	$0.99 \pm 0.01$	$0.19 \pm 0.02$	$0.29 \pm 0.03$	$0.03 \pm 0.04$	$1.51 \pm 0.07$
52.48 – 57.54	$0.95 \pm 0.01$	$0.18 \pm 0.02$	$0.27 \pm 0.03$	0	$1.43 \pm 0.04$
57.54 – 63.10	$1.06 \pm 0.01$	$0.26 \pm 0.02$	$0.30 \pm 0.03$	0	$1.60 \pm 0.05$
63.10 – 69.18	$0.96 \pm 0.01$	$0.21 \pm 0.02$	$0.35 \pm 0.03$	0	$1.52 \pm 0.04$
69.18 – 75.86	$1.02 \pm 0.01$	$0.24 \pm 0.02$	$0.34 \pm 0.03$	0	$1.57 \pm 0.04$
75.86 – 83.18	$0.93 \pm 0.01$	$0.14 \pm 0.02$	$0.33 \pm 0.03$	$-0.06 \pm 0.04$	$1.31 \pm 0.06$
83.18 – 91.20	$0.95 \pm 0.01$	$0.18 \pm 0.02$	$0.34 \pm 0.03$	0	$1.47 \pm 0.04$
91.20 – 100.00	$0.94 \pm 0.01$	$0.16 \pm 0.02$	$0.37 \pm 0.03$	0	$1.44 \pm 0.04$
100.00 – 316.23	$0.96 \pm 0.00$	$0.21 \pm 0.01$	$0.42 \pm 0.01$	$-0.04 \pm 0.01$	$1.49 \pm 0.02$
316.23 – 1000.00	$0.94 \pm 0.00$	$0.11 \pm 0.01$	$0.37 \pm 0.01$	0	$1.37 \pm 0.02$

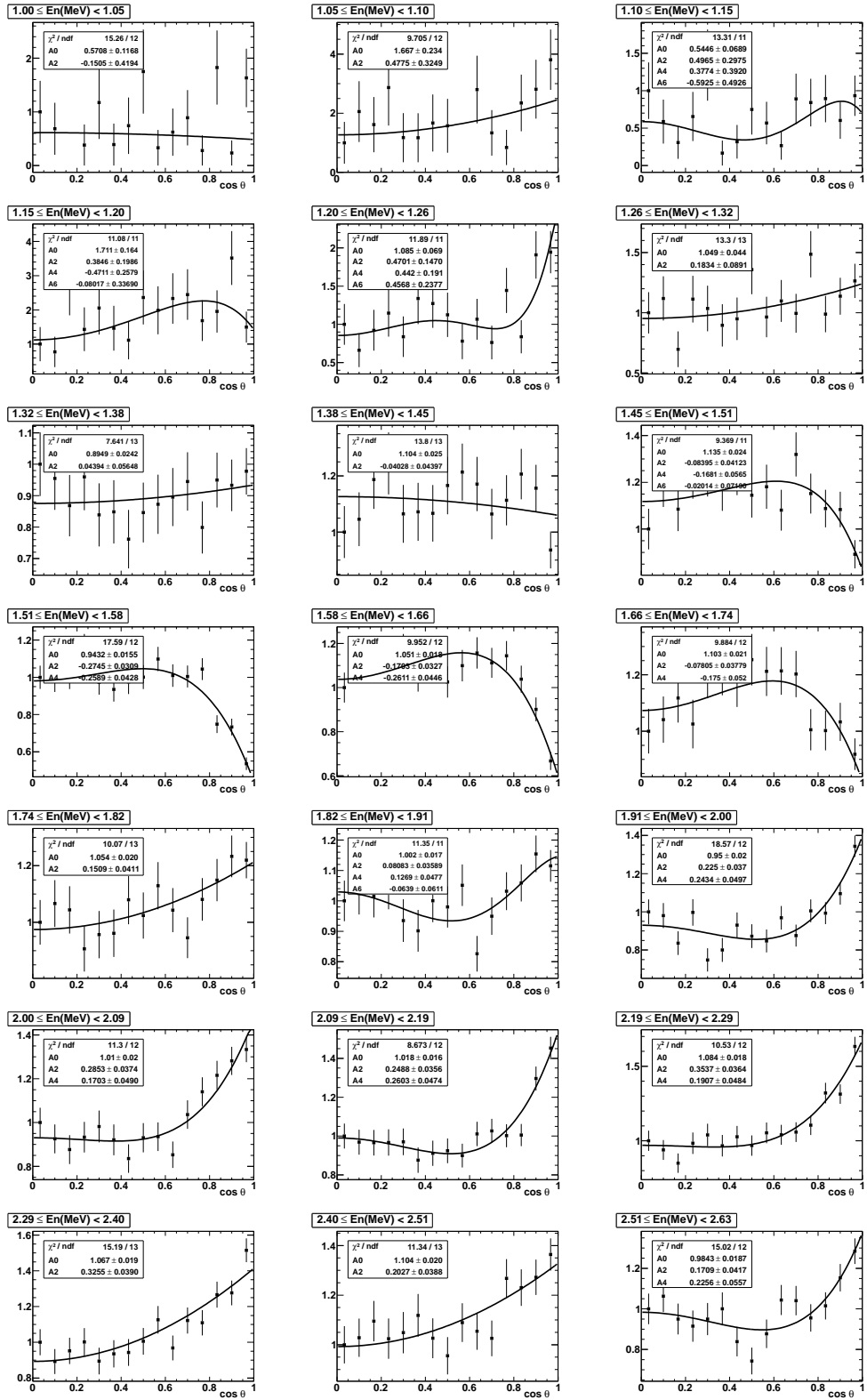


Figure C.1: Fits to the experimental angular distributions of  $^{232}\text{Th}(n,f)$ .

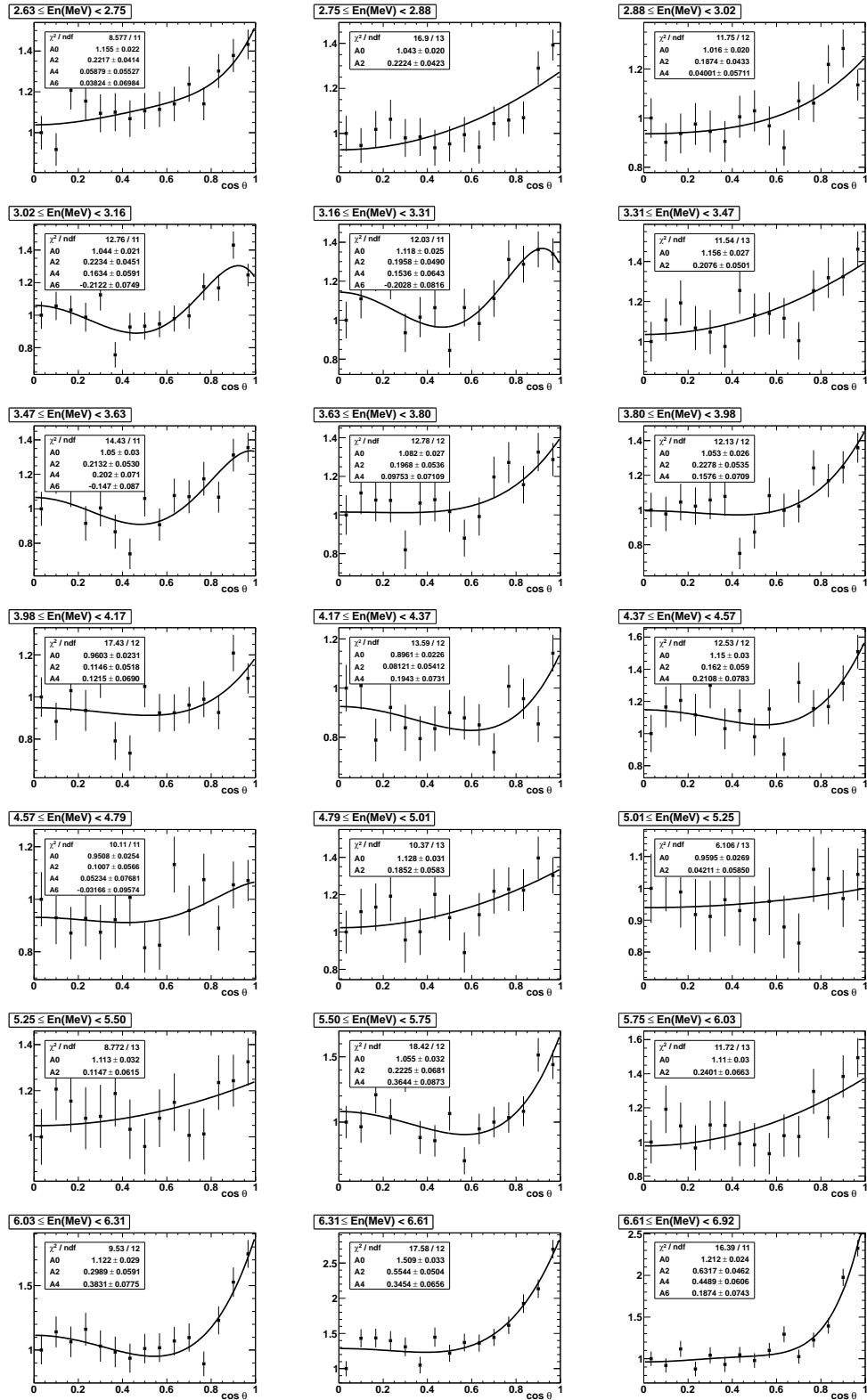


Figure C.2: The same as Fig. C.1.

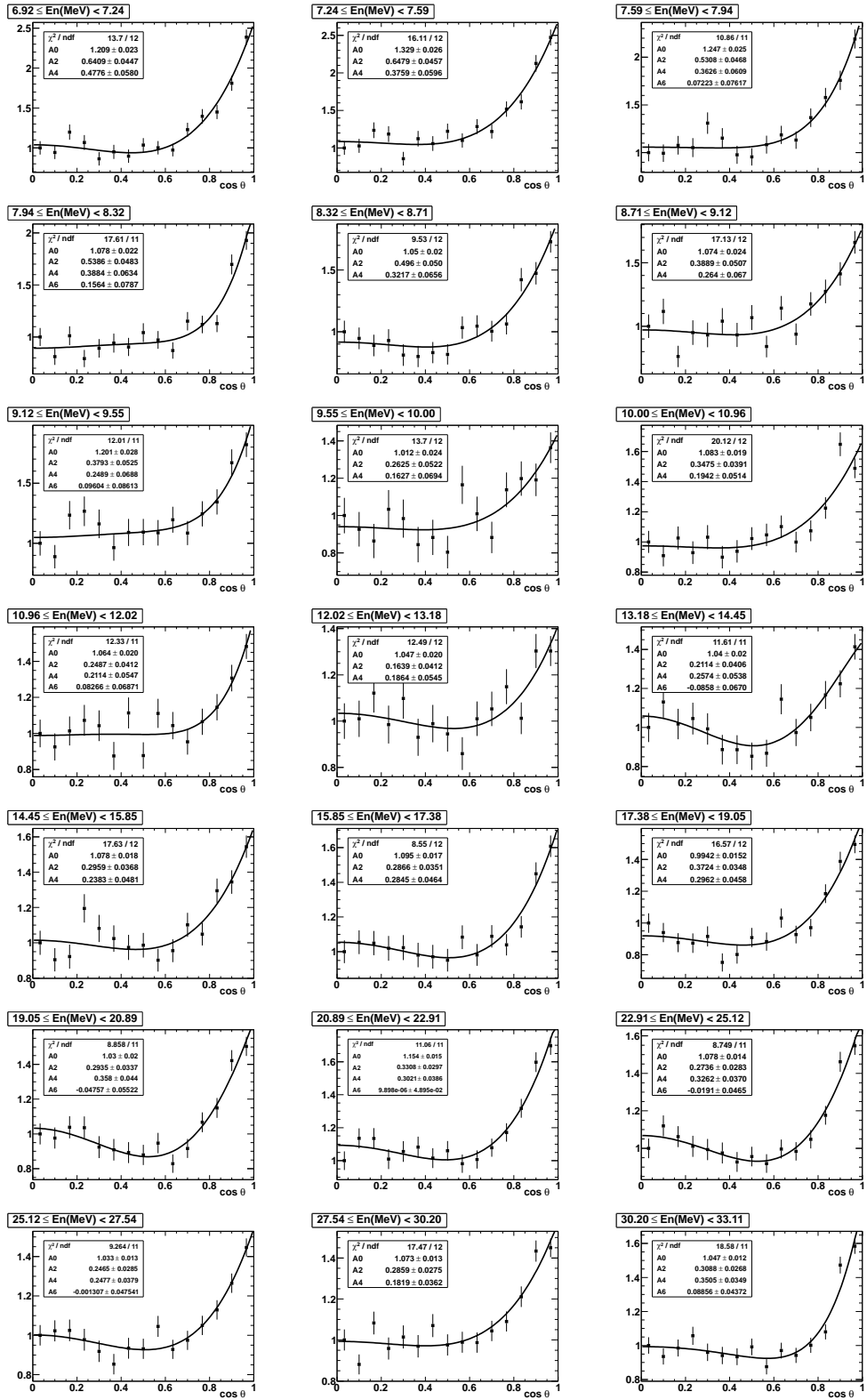


Figure C.3: The same as Fig. C.1.

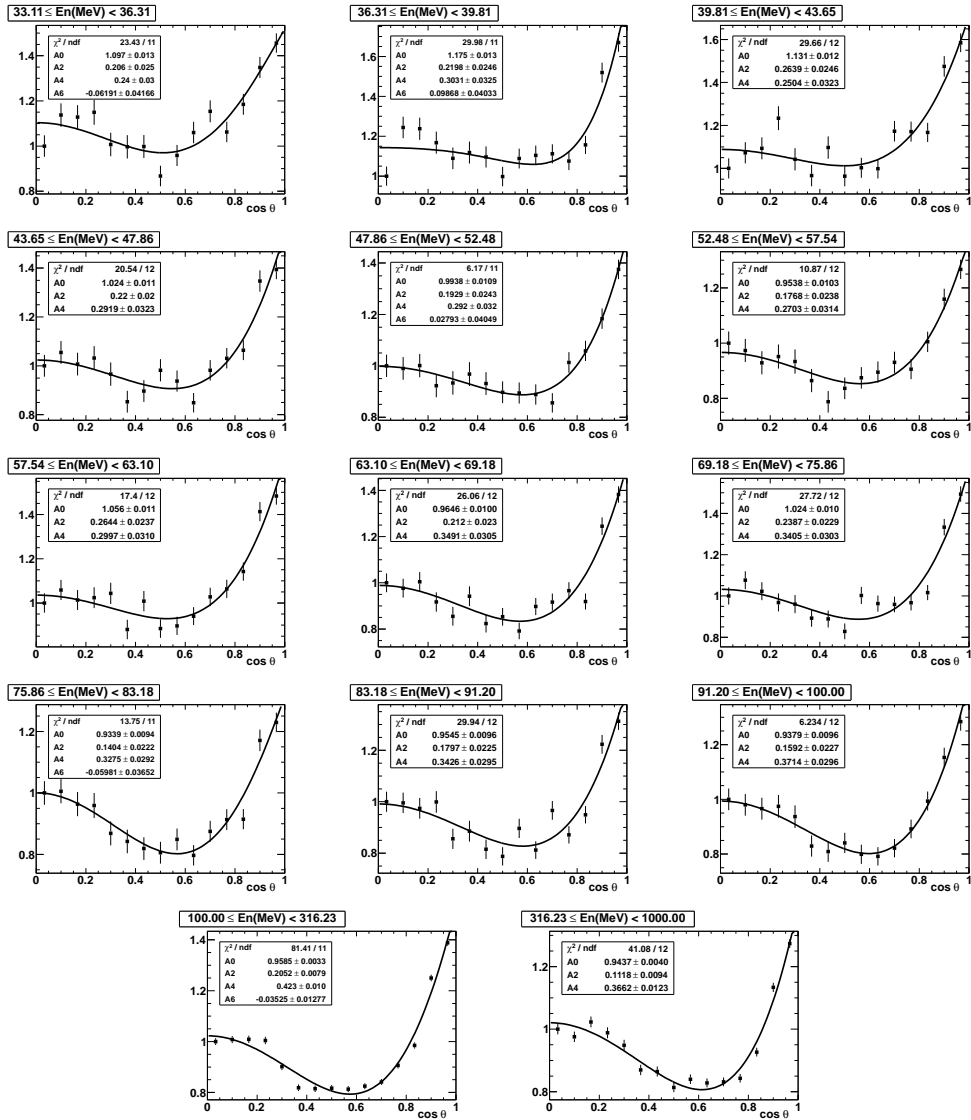


Figure C.4: The same as Fig. C.1.



# Bibliography

- [1] L. Tassan-Got, C. Stéphan, and C. O. Bacri et al. (The n\_TOF Collaboration). *Angular distributions in the neutron-induced fission of actinides. CERN/INTC 2006-016/INTC-P-209*, 2006.
- [2] L. Tassan-Got, L. Audouin, and M. Mac Cormick et al. (The n\_TOF Collaboration). *Angular distributions in the neutron-induced fission of actinides. CERN/INTC 2010-038/INTC-P-209-ADD-1*, 2010.
- [3] C. Paradela et al. *Phys. Rev. C*, 82:034601, 2010.
- [4] D. Tarrío et al. *Phys. Rev. C*, 83:044620, 2011.
- [5] S. Cohen and W. Swiatecki. *Ann. Phys.*, 22:406, 1963.
- [6] U. Abbondanno et al. (The n\_TOF Collaboration). *Measurements of Fission Cross Sections for the Isotopes relevant to the Thorium Fuel Cycle. CERN/INTC 2001-025*, 2001.
- [7] Generation IV International Forum. <http://www.gen-4.org>.
- [8] World Nuclear Association. <http://www.world-nuclear.org/>.
- [9] M. Lung and O. Gremm. *Nucl. Eng. Des.*, 180:133, 1998.
- [10] Thorium fuel cycle. Potential benefits and challenges. *IAEA-TECDOC*, 1450, 2005.
- [11] C. D. Bowman. *Annu. Rev. Nucl. Part. Sci.*, 48:505, 1998.
- [12] EXFOR (Experimental Nuclear Reaction Data). National Nuclear Data Center (NNDC) (Brookhaven), 2009. <http://www-nds.iaea.org/exfor/exfor.htm>.

- [13] M. B. Chadwick, M. Herman, P. Obložinský, et al. ENDF/B-VII.1: Nuclear data for science and technology: Cross sections, covariances, fission product yields and decay data. *Nuclear Data Sheets*, 112:2887, 2011.
- [14] K. Shibata, O. Iwamoto, T. Nakagawa, et al. JENDL-4.0: A New Library for Nuclear Science and Engineering. *J. Nucl. Sci. Techn.*, 48:1, 2011.
- [15] T. Fukahori et al. JENDL High Energy File 2007 (JENDL/HE-2007), 2007. To be submitted to *J. Nucl. Sci. Tech.* Available at: <http://www.ndc.jaea.go.jp>.
- [16] A. Santamarina, D. Bernard, P. Blaise, et al. The JEFF-3.1.1 Nuclear Data Library. *OECD/NEA Data Bank. JEFF Report 22*, 2009. (The last version 3.1.2 has been released in 2012 and the corresponding report has not been published yet. There are no differences between both versions for the case of Th-232).
- [17] V. N. Manokhin et al. BROND-2.2. Russian Evaluated Neutron Reaction Data Library. *Report IAEA-NDS-90 Rev. 8*, 1994.
- [18] Z. G. Ge, Z. X. Zhao, H. H. Xia, et al. The Updated Version of Chinese Evaluated Nuclear Data Library (CENDL-3.1). *J. Korean Phys. Soc.*, 59:1052, 2011.
- [19] NEA Nuclear Data High Priority Request List. The updated list is available online: <http://www.oecd-nea.org/dbdata/hpr1/index.html>.
- [20] V. G. Pronyaev. Summary report of the consultant's meeting on assessment of nuclear data needs for thorium and other advanced cycles. *IAEA Report INDC (NDS), 408*, 1999.
- [21] A. Trkov and D. W. Muir. *J. Nucl. Sci. and Techn.*, Supp. 2:1454, 2002.
- [22] M. Sin, R. Capote, A. Ventura, et al. *Phys. Rev. C*, 74:014608, 2006.
- [23] S. Bjørnholm and J. E. Lynn. *Rev. Mod. Phys.*, 52:725, 1980.
- [24] C. Rubbia, S. Andriamonje, D. Bouvet-Bensimon, et al. *Proposal for a Neutron Time of Flight Facility. CERN/LHC/98-02(EET) and CERN/LHC/98-02(EET)-Add. 1*, 1998.

- 
- [25] The n\_TOF Collaboration. *European Collaboration for High-Resolution Measurements of Neutron Cross Sections between 1 eV and 250 MeV. CERN/SPSC 99-8 SPSC/P310*, 1999.
- [26] The n\_TOF Collaboration. *Technical Report. CERN-INTC-2000-018*, 2000.
- [27] N. Colonna, F. Belloni, E. Berthoumieux, et al. *Energy Environ. Sci.*, 3:1910, 2010.
- [28] A. A. Goverdovski. In *Proceedings of the Workshop on Nuclear Reaction Data and Nuclear Reactors: Physics, Design and Safety, Trieste, Italy*, 2002.
- [29] O. Hahn and F. Strassmann. *Naturwissenschaften*, 26:755, 1938.
- [30] L. Meitner and O. R. Frisch. *Nature*, 143:239, 1939.
- [31] N. Bohr and J. A. Wheeler. *Phys. Rev.*, 56:426, 1939.
- [32] G. Herrmann. *Nucl. Phys. A*, 502:141, 1989.
- [33] R. Vandenbosch and J. R. Huizenga. *Nuclear Fission*. Academic Press, 1973.
- [34] C. Wagemans. *The Nuclear Fission Process*. CRC Press, 1991.
- [35] S. G. Prussin. *Nuclear Physics for Applications. A Model Approach*. Wiley-VCH Verlag & Co., 2007.
- [36] R. F. Casten. *Nuclear Structure from a Simple Perspective*. Oxford University Press, 2000.
- [37] B. L. Cohen. *Concepts of Nuclear Physics*. McGraw-Hill Book Company, 1971.
- [38] D. Vauthrein and D. M. Brink. Hartree-Fock calculations with Skyrme's Interaction. I. Spherical Nuclei. *Phys. Rev. C*, 5:626, 1982.
- [39] J. R. Stone and P.-G. Reinhard. *Phys. Rev. C*, 58:587, 2007.
- [40] S. Hilaire, A. J. Koning, and S. Goriely. *EPJ Web of Conferences*, 8:02004, 2010.
- [41] M. Bender, P.-H. Heenen, and P.-G. Reinhard. *Rev. Mod. Phys.*, 75:121, 2003.

- [42] N. Chamel, S. Goriely, and J. M. Pearson. *Nucl. Phys. A*, 812:72, 2008.
- [43] S. Goriely, N. Chamel, and J. M. Pearson. *Phys. Rev. Lett.*, 102:152503, 2009.
- [44] A.J. Koning, S. Hilaire, and M.C. Duijvestijn. TALYS-1.0. In *International Conference on Nuclear Data for Science and Technology - ND2007, April 22-27, 2007, Nice, France*, page 211, 2008.
- [45] M. Herman, R. Capote, B. V. Carlson, et al. *Nucl. Data Sheets*, 108:2655, 2007.
- [46] S. Goriely, S. Hilaire, A. J. Koning, et al. *Phys. Rev. C*, 79:024612, 2009.
- [47] S. Goriely, S. Hilaire, A. J. Koning, and R. Capote. *Phys. Rev. C*, 83:034601, 2011.
- [48] S. G. Nilsson, C. F. Tsang, A. Sobiczewski, et al. *Nucl. Phys. A*, 131:1, 1969.
- [49] W. D. Myers and W. J. Swiatecki. *Nucl. Phys.*, 81:1, 1966.
- [50] V. M. Strutinsky. *Nucl. Phys. A*, 95:420, 1967.
- [51] V. M. Strutinsky. *Nucl. Phys. A*, 122:1, 1968.
- [52] P. Möller and J. R. Nix. In *Proceedings of the Third IAEA Symposium on the Physics and Chemistry of fission, Rochester, New York, 1973*, page 103, 1974. INDC(NDS)-245.
- [53] J. Blons, C. Mazur, and D. Paya. *Phys. Rev. Lett.*, 35:1749, 1975.
- [54] J. Blons, C. Mazur, D. Paya, M. Ribrag, and H. Weigmann. *Phys. Rev. Lett.*, 41:1282, 1978.
- [55] J. Blons, C. Mazur, D. Paya, M. Ribrag, and H. Weigmann. *Nucl. Phys. A*, 414:1, 1984.
- [56] M. Kowal and J. Skalski. *Phys. Rev. C*, 85:061302, 2012.
- [57] M. Mirea, L. Tassan-Got, C. Stephan, et al. *Phys. Rev. C*, 76:064608, 2007.
- [58] P. Möller, A. J. Sierk, T. Ichikawa, et al. *Phys. Rev. C*, 79:064304, 2009.

- [59] P. Möller, D. G. Madland, A. J. Sierk, and A. Iwamoto. *Nature*, 409:785, 2001.
- [60] B. D. Wilkins, E. P. Steinberg, and R. R. Chasman. *Phys. Rev. C*, 14:1832, 1976.
- [61] U. Brosa, S. Grossmann, and A. Müller. *Phys. Rep.*, 197:167, 1990.
- [62] M. C. Duijvestijn, A. J. Koning, and F.-J. Hamsch. *Phys. Rev. C*, 64:014607, 2001.
- [63] V. M. Maslov, Yu. V. Porodzinskij, N. A. Tetereva, A. B. Kagalenko, N. V. Kornilov, M. Baba, and A. Hasegawa. Neutron Data Evaluation of  $^{232}\text{Th}$ . *IAEA Report INDC (BLR), 016*, 2003.
- [64] I. V. Ryzhov et al. *Nucl. Phys. A*, 760:19, 2005.
- [65] V. M. Maslov. *Phys. Lett. B*, 649:376, 2007.
- [66] F.-J. Hamsch, G. Vladuca, A. Tudora, S. Oberstedt, and I. Ruskov. *Ann. Nucl. En.*, 32:1297, 2005.
- [67] L. E. Glendenin, J. E. Gindler, D. J. Henderson, and J. W. Meadows. *Phys. Rev. C*, 24:2600, 1981.
- [68] L. E. Glendenin, J. E. Gindler, I. Ahmad, D. J. Henderson, and J. W. Meadows. *Phys. Rev. C*, 22:152, 1980.
- [69] V. E. Viola, K. Kwiatkowski, and M. Walker. *Phys. Rev. C*, 31:1550, 1985.
- [70] E. J. Winhold, P. T. Demos, and I. Halpern. Minutes of the Meeting at Chicago, October 24-27, 1951. *Phys. Rev.*, 85:728, 1952.
- [71] E. J. Winhold, P. T. Demos, and I. Halpern. *Phys. Rev.*, 87:1139, 1952.
- [72] J. E. Brolley and W. C. Dickinson. *Phys. Rev.*, 94:640, 1954.
- [73] J. E. Brolley, W. C. Dickinson, and R. L. Henkel. *Phys. Rev.*, 99:159, 1955.
- [74] R. L. Henkel and J. E. Brolley Jr. *Phys. Rev.*, 103:1292, 1956.
- [75] L. Wilets and D. M. Chase. *Phys. Rev.*, 103:1296, 1956.
- [76] R. W. Lamphere. *Nucl. Phys.*, 38:561, 1962.

- [77] U. Abbondanno et al. (The n\_TOF Collaboration). *Status Report. CERN/INTC 2001-021*, 2002.
- [78] U. Abbondanno et al. (The n\_TOF Collaboration). *CERN n\_TOF Facility: Performance Report. CERN-SL-2002-053 ECT*, 2002.
- [79] PS-Vistars is available online: <http://op-webtools.web.cern.ch/op-webtools/Vistar/vistars.php?usr=CPS>.
- [80] The n\_TOF Collaboration. *n\_TOF New target commissioning and beam characterization. CERN/INTC 2008-035/INTC-P-249*, 2008.
- [81] C. Paradela. *Instalación y calibración de un monitor de neutrones para n\_TOF*. (Master Thesis). Universidade de Santiago de Compostela, 2003.
- [82] C. Borcea, P. Cenini, M. Dahlfors, et al. *Results from the Commissioning of the n\_TOF Spallation Neutron Source at CERN. CERN-SL-2002-051*, 2002.
- [83] C. Borcea et al. *Nucl. Instr. and Meth. A*, 513:524–537, 2003.
- [84] D. Cano-Ott C. Guerrero, V. Becares and the n\_TOF Collaboration. *J. Korean Phys. Soc.*, 59:1624, 2011. In Proceedings of the International Conference on Nuclear Data for Science and Technology 2010.
- [85] J. Pancin et al. (The n\_TOF Collaboration). *Nucl. Instr. and Meth. A*, 524:102, 2004.
- [86] I. Savvidis, C. Lampoudis, T. Papaevangelou, C. Eleftheriadis, and the n\_TOF Collaboration. *Rad. Meas.*, 42:1492, 2007.
- [87] S. Andriamonje, M. Calviani, Y. Kadi, and the n\_TOF Collaboration. *J. Korean Phys. Soc.*, 59:1601, 2011. In Proceedings of the International Conference on Nuclear Data for Science and Technology 2010.
- [88] U. Abbondanno et al. (The n\_TOF Collaboration). *Nucl. Instr. and Meth. A*, 538:692–702, 2005.
- [89] CERN Advanced STORAge manager (CASTOR). Information available at: <http://castor.web.cern.ch/>.
- [90] M. Calviani, P. Cennini, D. Karadimos, V. Ketlerov, V. Konovalove, W. Furman, A. Goverdowski, V. Vlachoudis, L. Zanini, and the n\_TOF Collaboration. *Nucl. Instr. and Meth. A*, 594:220, 2008.

- [91] M. Calviani. *Measurement of fission cross-section of actinides at n\_TOF for advanced nuclear reactors*. PhD thesis, Università degli Studi di Padova, 2009.
- [92] M. Calviani, J. Praena, and the n\_TOF Collaboration. *Phys. Rev. C*, 80:044604, 2009.
- [93] M. Calviani, E. Berthomieux, and S. Andriamonje et al. (The n\_TOF Collaboration). *Measurement of the fission cross-section of  $^{240}\text{Pu}$  and  $^{242}\text{Pu}$  at CERN's n\_TOF Facility*. CERN/INTC 2010-042, 2010.
- [94] G. F. Knoll. *Radiation Detection and Measurement*. John Wiley & Sons, 2000.
- [95] W. R. Leo. *Techniques for Nuclear and Particle Physics Experiments*. Springer-Verlag, 1994.
- [96] D. N. Poenaru and W. Greiner. *Experimental Techniques in Nuclear Physics*. Walter de Gruyter, 1997.
- [97] J. Pancin, B. Fernández, S. Damoy, et al. Micromegas at low pressure for beam tracking. *J. Instrum.*, 7:C03017, 2012. In Proceedings of the 2nd International Conference on Micro Pattern Gaseous Detectors, Kobe, Japan, 2011.
- [98] J. W. Keuffel. *Rev. Sci. Instr.*, 20:202, 1949.
- [99] R. W. Pidd and L. Madansky. *Phys. Rev.*, 75:1175, 1949.
- [100] A. Breskin and N. Zwang. *Nucl. Instr. and Meth.*, 144:609, 1977.
- [101] J. Christiansen, G. Hempel, H. Ingwersen, et al. *Nucl. Phys. A*, 239:253, 1975.
- [102] G. Hempel, F. Hopkins, and G. Schatz. *Nucl. Instr. and Meth.*, 131:445, 1975.
- [103] J. C. Sanabria, B. L. Berman, C. Cetina, et al. *Nucl. Instr. and Meth. A*, 441:525, 2000.
- [104] A. A. Kotov, W. Neubert, L. N. Andronenko, B. L. Gorshkov, G. G. Kovshevny, L. A. Vaishnene, and M. I. Yazikov. *Nucl. Instr. and Meth.*, 178:55, 1980.
- [105] A. A. Kotov, L. A. Vaishnene, V. G. Vovchenko, , et al. *Phys. Rev. C*, 74:034605, 2006.

- [106] M. Nakhostin, M. Baba, T. Itoga, T. Oishi, Y. Unno, S. Kamada, and T. Okuji. *Rad. Prot. Dos.*, 129:426, 2008.
- [107] A. Breskin and N. Zwang. *Nucl. Instr. and Meth.*, 146:461, 1977.
- [108] D. v. Harrach and H. J. Specht. *Nucl. Instr. and Meth.*, 164:477, 1979.
- [109] C. Stephan, L. Ferrant, B. Berthier, S. David, L. Tassan-Got, C. O. Bacri, F. Rejmund, and C. Moreau (n\_TOF Collaboration). *J. Nucl. Sci. and Techn.*, Supp. 2:276, 2002.
- [110] L. Ferrant. *Mesures de sections efficaces de fission induit par neutrons sur des actinides du cycle du thorium à n\_TOF*. PhD thesis, Université Paris XI Orsay, 2005.
- [111] A. D. Carlson, V.G. Pronyaev, D.L. Smith, et al. *Nuclear Data Sheets*, 110:3215, 2009. See also <http://www-nds.iaea.org/standards/>.
- [112] C. Paradela. *Measurement of the U-234(n,f) cross section with PPAC detectors at the n\_TOF facility*. PhD thesis, Universidade de Santiago de Compostela, 2005.
- [113] F. Saint Laurent, M. Conjeaud, R. Dayras, et al. *Phys. Lett.*, 110B:372, 1982.
- [114] M. Fatyga, K. Kwiatkowski, H. J. Karwowski, et al. *Phys. Rev. C*, 32:1496, 1985.
- [115] G. Lorusso et al. *Nucl. Instr. and Meth. A*, 532:622–630, 2004.
- [116] C. Guerrero, A. Tsinganis et al. (The n\_TOF Collaboration). Performance of the neutron time-of-flight n\_TOF facility at CERN. *To be submitted to Nucl. Instr. and Meth. A*, 2012.
- [117] A. Ferrari, P. R. Sala, A. Fasso, et al. FLUKA: a multi-particle transport code. *CERN-2005-10, INFN/TC-05/11, SLAC-R-773*, 2005.
- [118] G. Battistoni, S. Muraro, P.R. Sala, et al. The FLUKA code: Description and benchmarking. *AIP Conference Proceeding*, 896:31, 2007. In Proceedings of the Hadronic Shower Simulation Workshop 2006, Fermilab, 2006.
- [119] S. Agostinelli, J. Allison, K. Amako, et al. *Nucl. Instr. and Meth. A*, 506:250, 2003. Geant4 official webpage: <http://geant4.web.cern.ch/geant4/>.

- [120] S. B. Ermagambetov and G. N. Smirenkin. *Sov. J. Nucl. Phys.*, 11:646, 1970.
- [121] G. Barreau. *C. E. N. Bordeaux-Gradignan Reports*, 7706, 1977.
- [122] J. Caruana, J. W. Boldeman, and R. L. Walsh. *Nucl. Phys. A*, 285:205, 1977.
- [123] B. M. Gokhberg, L. D. Kozlov, S. K. Lisin, et al. *Sov. J. Nucl. Phys.*, 47:201, 1988.
- [124] R. B. Leachman and L. B. Blumberg. *Phys. Rev.*, 137:814, 1965.
- [125] R. H. Iyer, R. Sampathkumar, and N. K. Chaudhuri. *Prog. Rep.: BARC Trombay Report Series*, 872:107, 1976.
- [126] Kh. D. Androsenko, G. G. Korolev, and D. L. Shpak. *Vop. At. Nauki i Tekhn., Ser. Yadernye Konstanty*, 2/46:9, 1982.
- [127] E. Barutcugil, S. Juhasz, M. Varnagy, et al. *Nucl. Phys. A*, 173:571, 1971.
- [128] V. Emma, S. Lo Nigro, and C. Milone. *Nucl. Phys. A*, 199:186, 1973.
- [129] D. Tarrío et al. (the n\_TOF Collaboration). On the systematic errors of the Th<sup>232</sup>(n,f) cross section measured with PPACs at CERN-n\_TOF. In *Proceedings of the Final Scientific EFNUDAT Workshop, August 30 - September 2, 2010, CERN, Geneva, Switzerland*, page 39, 2010.
- [130] M. B. Chadwick, P. Obložinský, M. Herman, et al. ENDF/B-VII.0: Next generation evaluated nuclear data library for nuclear science and technology. *Nuclear Data Sheets*, 107:2931, 2006.
- [131] V. M. Pankratov. *Sov. J. At. Energy*, 14:167, 1963.
- [132] S. B. Ermagambetov, V. F. Kuznetsov, and G. N. Smirenkin. *Sov. J. Nucl. Phys.*, 5:181, 1967.
- [133] A. N. Behkami, J. R. Huizenga, and J. H. Roberts. *Nucl. Phys. A*, 118:65, 1968.
- [134] J. W. Meadows. *Argonne National Laboratory Reports*, 83, 1983.
- [135] R. P. Anand, K. N. Iyengar, and N. N. Ajitanand. *Prog. Rep.: BARC Trombay Report Series*, 1297:1, 1986.

- [136] P. W. Lisowski, J. L. Ullman, S. J. Balestrini, A. D. Carlson, O. A. Wasson, and N. W. Hill. In *Proceedings of the Conf. on Nucl. Data For Sci. and Technol., Mito, Japan*, page 97, 1988.
- [137] O. Shcherbakov, A. Donets, A. Evdokimov, et al. *J. Nucl. Sci. and Techn.*, Supp. 2:230, 2002.
- [138] Y. Ayant and M. Borg. *Funciones Especiales*. Alhambra, 1974.
- [139] G. F. Simmons and J. S. Robertson. *Ecuaciones diferenciales*. McGraw Hill, 1999.
- [140] A. C. King, J. Billingham, and S. R. Otto. *Differential Equations. Linear, Nonlinear, Ordinary, Partial*. Cambridge University Press, 2003.
- [141] G. Arfken. *Mathematical Methods for Physicists*. Academic Press, 1985.
- [142] T. L. Chow. *Mathematical Methods for Physicists. A concise Introduction*. Cambridge University Press, 2000.
- [143] A. P. Levanyuk and A. Cano. *Métodos Matemáticos de la Física. Método de Fourier*. Ediciones de la Universidad Autónoma de Madrid, 2006.
- [144] M. R. Spiegel, J. Liu, and L. Abellanas. *Fórmulas y Tablas de Matemática Aplicada*. McGraw Hill, 2000.